



Escola Tècnica Superior d'Enginyeries
Industrial i Aeronàutica de Terrassa

UNIVERSITAT POLITÈCNICA DE CATALUNYA

STUDY OF AN AIR-BREATHING ENGINE FOR HYPERSONIC FLIGHT

TECHNICAL REPORT

Author: Marta Marimon Mateu

Tutor: Josep Oriol Lizandra Dalmases

September 2013

[This page is intentionally left blank]

Abstract

A computationally efficient, quasi-one-dimensional, supersonic combustion model has been developed to simulate high-speed engine flowfields such as in a scramjet. The model can be used in design and optimization studies, where a wide range of engine inlet conditions may be encountered.

The model solves a series of ordinary differential equations that come from the equations of fluid motion coupled with combustion. The effects of area change, wall skin friction, mass injection, fuel mixing, and heat transfer are included. The equations are derived assuming an open thermodynamic system with equilibrium or with finite-rate chemistry. Results will show the differences on combustor performance between considering equilibrium or not. The inclusion of chemical kinetics allows for a prediction of fuel ignition, a finite rate process that inherently cannot be predicted using equilibrium methods. Therefore, incorporating the timescales of fuel mixing and ignition is crucial for an accurate prediction of combustor performance in most scramjet operating conditions.

Furthermore, the effects of dissociation, fuel mixing and friction are discussed. Eventually, a simple analysis of the air inlet and the nozzle is developed in order to have an overall vision of the scramjet and its feasibility.

Table of contents

Abstract.....	3
Table of contents.....	4
Index of figures.....	6
Index of tables.....	8
Nomenclature.....	9
1. Aim.....	12
2. Scope.....	13
3. Introduction.....	14
3.1. Definition of a scramjet engine.....	14
3.2. Scramjet engine historical timeline.....	15
3.3. Applications for a scramjet engine.....	19
3.4. Current scramjet engine technology challenges.....	23
4. Parts of a scramjet engine.....	27
4.1. Air inlet.....	27
4.2. Isolator.....	30
4.3. Combustor.....	31
4.4. Nozzle.....	32
5. Combustion model.....	35
5.1. Fluid motion equations.....	35
5.1.1. Mass conservation.....	36
5.1.2. Momentum conservation.....	37
5.1.3. Energy conservation.....	38
5.2. Equation of state.....	40
5.3. Combustion.....	40
5.3.1. Combustion without dissociation.....	41
5.3.2. Combustion with equilibrium dissociation.....	42
5.3.3. Combustion with non-equilibrium dissociation.....	46
5.4. Complete equation set.....	49
5.5. Semi-perfect gas flow properties.....	49
5.6. Supersonic mixing model.....	50
5.7. Reaction mechanism.....	52
6. Combustion code.....	54

7. Code verification	56
7.1. Isentropic evolution	56
7.2. Heat addition	57
7.3. Combustion without dissociation	58
7.4. Combustion with equilibrium dissociation	59
7.5. Combustion with non-equilibrium dissociation	62
8. Results	63
8.1. Chemical equilibrium without dissociation	63
8.1.1. HyShot II Flight Tests	63
8.1.2. Reflected shock tunnel experiment.....	64
8.1.3. Influence of mixing model.....	65
8.2. Effects of dissociation.....	69
8.2.1. Anderson & Gooderum experiment	69
8.2.2. Influence of combustor inlet conditions.....	73
8.2.3. Influence of combustor chamber design	75
8.3. Effects of friction.....	77
8.4. Application.....	78
9. Conclusions and recommendations	84
10. Bibliography	86
Annexes	89
A. Scramjet evolution	90
B. Governing equations detailed development	92
C. Air inlet performance.....	97
D. Nozzle performance.....	100

Index of figures

Figure 1. Schematic diagram of a ramjet engine	14
Figure 2. Schematic diagram of a scramjet engine	15
Figure 3. NASA Hypersonic Research Engine	16
Figure 4. NASA airframe-integrated engine configuration	16
Figure 5. NASA Hyper-X research vehicle	17
Figure 6. Hyper-X flight trajectory	18
Figure 7. HyShot payload	18
Figure 8. HyShot flight profile	19
Figure 9. Specific Impulse versus Mach number for various engine types	20
Figure 10. Propulsion system options as a function of Mach number	20
Figure 11. Propulsion-airframe integrated scramjet with station numbering	27
Figure 12. Types of supersonic air inlets	29
Figure 13. Schematic of flow structure in an isolator	30
Figure 14. Specific impulse for equilibrium nozzle flow (combustor pressure fixed at 1 atm)	34
Figure 15. Specific impulse for frozen nozzle flow (combustor pressure fixed at 1 atm)	34
Figure 16. Control volume for developing the governing equations of the combustion model	36
Figure 17. Chemical equilibrium in function of T , for $\phi = 1$ and $p = 1 atm$	59
Figure 18. Zoom in of Figure 17	59
Figure 19. Chemical equilibrium in function of ϕ , for $T = 3000K$ and $p = 1 atm$	60
Figure 20. Zoom in of Figure 19	60
Figure 21. Chemical equilibrium in function of p , for $\phi = 1$ and $T = 3000K$	61
Figure 22. Temperature rise in combustion of H_2 with air, as a function of equivalence ratio, and initial and final temperature, for pressure of 1 atm and no flow	61
Figure 23. Schematic diagram of the experimental HyShot II combustion duct [22]. Units are in meters	64
Figure 24. Pressure distribution in the HyShot II combustor (P_0 is the pressure at combustor entrance)	64
Figure 25. Schematic diagram of the experimental T4 reflected shock tunnel [23]. Units are in meters	65
Figure 26. Pressure distribution for T4 experiment (P_0 is the pressure at combustor entrance)	65
Figure 27. Influence of mixing model on flowfield performance (the experiment of Section 8.1.2 is used, $c_f = 0.002$, $T_w = 500K$)	66

Figure 28. Influence of mixing length on flowfield performance (the experiment of Section 8.1.2 is used, $c_f = 0.002$, $T_w = 500K$).	67
Figure 29. Schematic diagram of Anderson & Gooderum's experimental combustor [17]. Units are in meters.	69
Figure 30. Flowfield performance for Anderson & Gooderum's experiment ($c_f = 0.002$, $T_w = 500K$). All variables except thrust are dimensionalised by its initial values. Legend: blue = no dissociation, red = equilibrium dissociation, green = non-equilibrium dissociation.....	70
Figure 31. Species mass fractions for Anderson & Gooderum's experiment ($c_f = 0.002$, $T_w = 500K$). N_2 is not shown since it is not dissociated and it acts as an inert gas. Legend: blue = no dissociation, red = equilibrium dissociation, green = non-equilibrium dissociation.....	71
Figure 32. Flowfield performance in an area constant duct for different initial conditions ($c_f = 0$, adiabatic walls). Legend: black = case 1, blue = case 2, green = case 3, red = case 4; continuous line = equilibrium & dashed line = non-equilibrium.	74
Figure 33. Necessary length to achieve equilibrium in function of combustor inlet Mach.....	75
Figure 34. Flowfield performance in a diverging duct for different area ratios ($c_f = 0$, adiabatic walls). Legend: black = Case 1, blue = Case 2, green = Case 3, red = Case 4, pink = Case 5; dashed = Case 6.....	76
Figure 35. Net thrust generated by the combustion chamber in function of the area ratio	76
Figure 36. Performance of cold flow along a constant area duct.....	78
Figure 37. Schematic illustration of a scramjet engine	79
Figure 38. Properties distribution in the combustor of Figure 37	80
Figure 39. Combustor & nozzle properties distribution. The combustor ends at $x = 5.8 m$ and is performed with finite-rate chemistry. The nozzle has been simulated with three types of flow. Legend: blue = frozen flow, green = finite-rate chemistry, red = equilibrium flow.....	82
Figure 40. Oblique shock wave.....	97
Figure 41. Scramjet inlet with three shock waves.....	98
Figure 42. Total pressure ratio in function of flight Mach number and kinetic energy efficiency.....	99
Figure 43. Internal nozzle	100

Index of tables

Table 1. Attributes of space launch systems	22
Table 2. Abridged Jachimowski mechanism reactions	52
Table 3. Abridged Jachimowski mechanism parameters. Units are <i>cal</i> , <i>mol</i> , <i>cm</i> ³ , <i>s</i> , <i>K</i>	53
Table 4. Flow properties at combustor entrance to get graphs of Figure 32	74
Table 5. Area ratios of the combustor to get graphs of Figure 34	75
Table 6. Exit nozzle flow properties for equilibrium flow, finite-rate chemistry and frozen flow	82
Table 7. Worldwide scramjet evolution 1955-1990	90
Table 8. Worldwide scramjet evolution 1990-today	91

Nomenclature

Roman symbols

a	sound velocity, m/s
A	geometric area, m ²
A_r	pre-exponential factor, cm mol s
a_{1-7}	curvefit constants
c_f	wall skin friction coefficient
c_{fj}	fuel jet (or mixing) friction coefficient
C_H	Stanton number
c_p	specific heat capacity at constant pressure, J/kgK
C_v	nozzle velocity coefficient
d_f	injector hydraulic diameter, m
e	specific energy, J/kg
E_r	activation energy for reaction, J/mol
f	fuel - air ratio
F	thrust, N
F_{mix}	fuel jet (or mixing) friction force, N
F_{wall}	wall skin friction force, N
g	gravitational intensity, m/s ²
G	Gibbs free energy, J/kg
h	specific enthalpy, J/kg
Δh_f^0	standard enthalpy of formation, J/kg
I_{sp}	specific impulse, s
k_b	backward rate constant, cm mol s
k_f	forward rate constant, cm mol s
K_c	equilibrium constant based on concentrations
K_p	equilibrium constant based on pressures
L	combustor length, m
L_{mix}	mixing length, m
m	mass, kg
\bar{m}	mass flow parameter
\dot{m}	mass flow rate, kg/s
\dot{m}_f	fuel mass flow rate not mixed with air, kg/s
\dot{m}_{fm}	fuel mass flow rate mixed with air (available for reaction), kg/s
\dot{m}_{of}	fuel mass flow rate through the injectors, kg/s
M	Mach number

MW	molecular weight, kg/mol
n	mol, mol
N_i	total number of species
$N_{i,r}$	total number of species in the r th reaction
N_r	total number of reactions
p	pressure, Pa
P_{fj}	fuel jet hydraulic perimeter, m
Pr	Prandtl number
P_w	wall perimeter, m
\dot{q}	heat transfer rate per unit area, J/m ² s
\dot{q}_r	rate-of-progress variable, mol/m ³ s
r	recovery factor
R	universal gas constant, J/molK
R_f	Reynolds analogy factor
R_g	gas constant, J/kgK
s	specific entropy, J/kgK
T	temperature, K
u	velocity, m/s
x	axial coordinate, m
Y	mass fraction

Greek symbols

β_r	temperature exponent
γ	ratio of specific heats
$\gamma_{i,r}$	third-body efficiency of the i th species in the r th reaction
ε	ratio of fuel injection velocity to flowfield velocity
η_c	combustion efficiency
η_d	air inlet kinetic energy efficiency
η_m	mixing efficiency
π_d	air inlet total pressure ratio
ρ	density, kg/m ³
$\nu_{i,r}$	stoichiometric coefficient of the i th species in the r th reaction
ϕ	equivalence ratio
$\chi_{i,r}$	chemical symbol of the i th species in the r th reaction
$\dot{\omega}$	molar production rate, mol/m ³ s

Subscripts

<i>a</i>	air
<i>aw</i>	adiabatic wall
<i>f</i>	fuel
<i>i</i>	<i>i</i> th specie
<i>r</i>	<i>r</i> th reaction
<i>ref</i>	reference conditions
<i>st</i>	stoichiometric conditions
<i>t</i>	total or stagnation conditions
<i>w</i>	wall

1. Aim

The aim of this study is to develop a parametric analysis of an airbreathing engine capable to propel a vehicle through a hypersonic flight, making especial emphasis on the combustion due to its high repercussion on the efficiency.

2. Scope

- Research of information relating to scramjet concept, its historical evolution and highlights.
- Research of information concerning to supersonic combustion and its modelling.
- Development of a quasi-one-dimensional combustor model.
- Implementation of the combustor model with MATLAB.
- Verification of the code implemented in MATLAB.
- Analyses of results and some critical parameters influences.
- Study of air inlet and nozzle in order to have an overall vision of scramjet.

3. Introduction

The purpose of this project is to develop a study of an airbreathing engine for a hypersonic flight. On the basis of current technology, the engine able to achieve this is called SCRAMJET. This chapter will provide a basic introduction to scramjet technology by presenting the definition, a historical timeline, possible applications, and the current status of scramjet engines.

3.1. Definition of a scramjet engine

In order to provide a definition of a scramjet engine, the definition of a ramjet engine is first necessary, as a scramjet engine is a direct descendant of a ramjet engine.

Ramjet engines have no moving parts unlike turbojets or turbofans. It is an open duct constituted of an inlet, a combustion chamber and a nozzle. The compression of the intake air is achieved through the inlet by the forward speed of the air vehicle which is supersonic. So, the freestream air at the combustor entrance has increased its temperature and pressure, and has reduced its speed to subsonic. Then, the freestream air is ignited with the addition of fuel and combustion takes place. Lastly, a nozzle accelerates the exhaust gases to supersonic speeds, resulting in thrust. Figure 1 shows a schematic diagram of a ramjet engine.

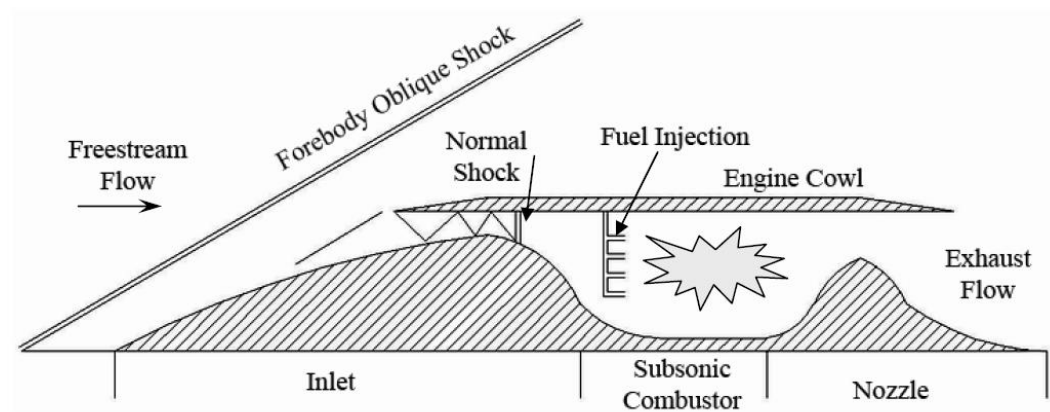


Figure 1. Schematic diagram of a ramjet engine

Due to the deceleration of the freestream air through the inlet, the temperature and the pressure of the flow at the entrance of the combustor is considerably higher than in the freestream. At flight speeds of around Mach 6

these increases of temperature and pressure make inefficient both the deceleration of the freestream air into subsonic speeds and the combustion. Thus, if the flow is no longer slowed to subsonic speeds, but rather only slowed to acceptable supersonic speeds, the combustion will be supersonic and the ramjet will be then termed Supersonic Combustion Ramjet, resulting in the acronym SCRAMJET. Figure 2 shows a schematic diagram of a scramjet engine. Notice that the configuration of a scramjet engine is very similar to that of a ramjet engine. The only difference is the integration of an isolator in some scramjets that operate between Mach 4 and 8. The reason is explained in Section 4.2.

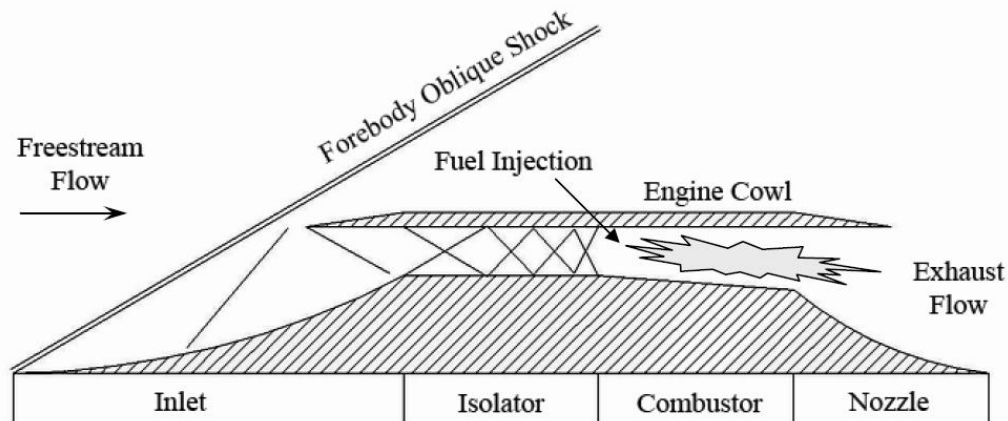


Figure 2. Schematic diagram of a scramjet engine

3.2. Scramjet engine historical timeline

The intention of this section is to provide a brief introduction to the historical timeline of the scramjet and a knowledge base for the current projects.

As mentioned previously, the scramjet is a direct descendant of the ramjet. Therefore, in an attempt to provide a brief historical timeline of the modern-day scramjet, it must first begin with the invention of the ramjet. As soon as five years after the legendary Wright brothers flight in 17 December 1903 the first concept of ramjet engine was patented in France. But it was not until the 1930s that testing started. Although tests demonstrated an increase in thrust, the ramjet engine began to receive attention during the second-half of the 1940s and reached a relative peak during the 1950s with a number of operational systems being deployed.

Development on the scramjet, on the other hand, did not begin until the 1960s. The leading figure in the development of hydrogen fuelled scramjet engines in those early years was unquestionably Ferri. His work inspired both United States and European research on scramjet engines, and many major programs started. The first one was the NASA Hypersonic Research Engine (HRE) program. The HRE program, which started in 1964, was crafted to develop and demonstrate flight-weight, variable-geometry, hydrogen-fuelled and hydrogen-cooled scramjet technology, by installing a scramjet engine on the X-15 A-2 rocket research airplane. Unfortunately, this program was not able to be flight tested because of the high cost, and the program ended in 1974, but with a total of some 52 tests completed. It should also be noted that the engine built for the HRE program was an axisymmetric combustor (see Figure 3).

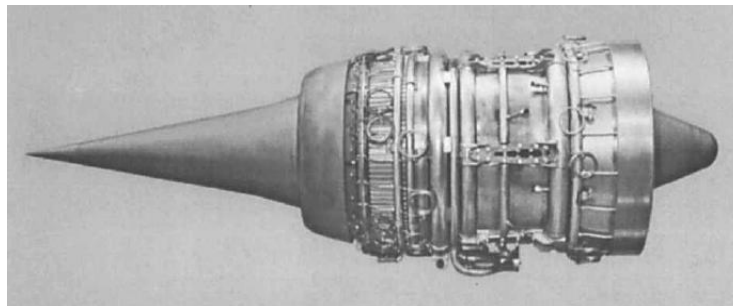


Figure 3. NASA Hypersonic Research Engine

This axisymmetric configuration proved to be popular in those early years because it made the study easier. However, it was not suitable for an operational engine, so NASA began to focus on a rectangular airframe-integrated engine (see Figure 4), in which much of the aircraft serves as part of the propulsion system. This engine configuration has gone through several generations of technology development because it is the only concept that has the additional power to make it practical for propulsion.

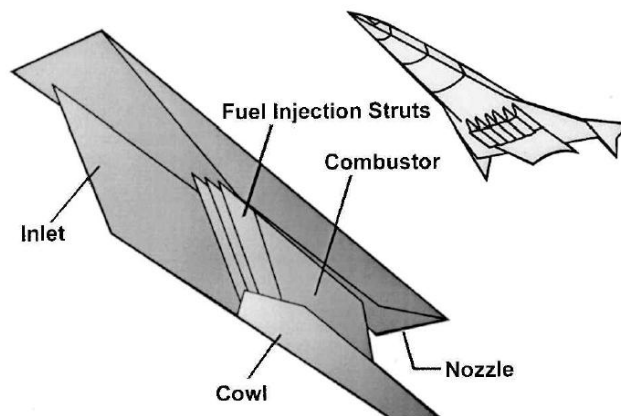


Figure 4. NASA airframe-integrated engine configuration

After these early attempts on the scramjet technology, many other projects in several countries continued developing. In United States, it can be stand out two extensive projects before the first flight test occurred. One was the Supersonic Combustion Ramjet Missile (SCRAM) program carried out in 1962-1977. The SCRAM program, which was oriented toward compact ship-launched missiles using storable reactive fuels, successfully demonstrated the technology necessary to proceed into flight testing. The other one was the National Aerospace Plane (NASP) program with the aim of developing a Single-Stage-to-Orbit (SSTO) hypersonic combined-cycle airbreathing engine to propel a research vehicle, the X-30. Since NASP program started in 1989 a large number of experimental engines were tested, but the X-30 experimental SSTO vehicle was not built because there was not funding, and NASP program ended in 1994.

A major new initiative by NASA to explore the overall performance of airframe-integrated dual-mode scramjet-powered vehicle is now underway. This initiative is called Hyper-X and it aims to flight demonstrate the first integrated airframe-scramjet engine hypersonic vehicle and flight validate key propulsion and related technologies. The vehicle designed to carry out this program is called X-43 and it is attached to a Pegasus Solid Propellant Booster which is air-launched from a B-52 aircraft. Figure 5 shows a picture of the X-43 and Figure 6 shows its flight trajectory. The first successful flight test of X-43 took place on March 2004 reaching a speed of Mach 7. And on November 2004, X-43 made a second flight test and got Mach 10.

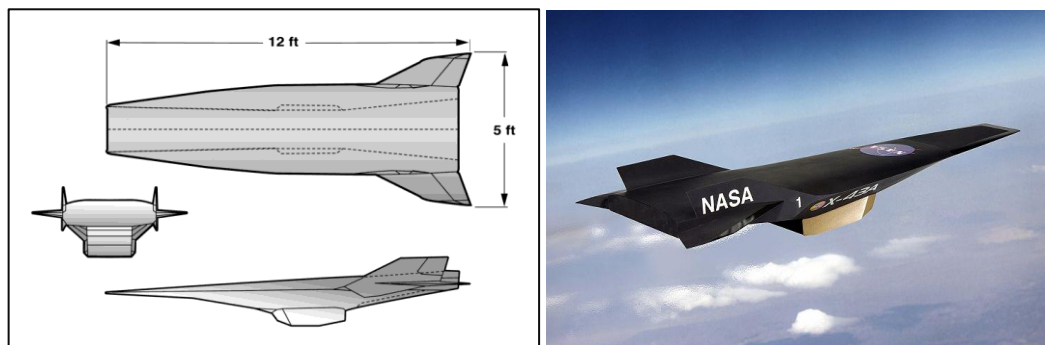


Figure 5. NASA Hyper-X research vehicle

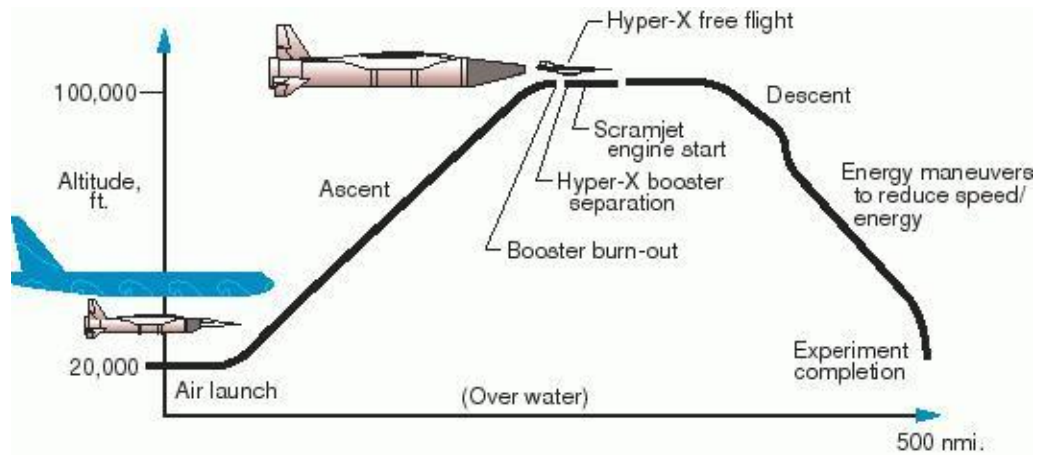


Figure 6. Hyper-X flight trajectory

Though X-43 set a speed record, it was not the first flight test of a scramjet. That title is occupied by the University of Queensland in Australia for the HyShot program. HyShot program has been developed with the object of obtaining the correlation between flight and ground test supersonic combustion data, and on July 2002 made the first flight test of a scramjet engine. The scramjet was launched by an un-guided sounding rocket on a highly parabolic trajectory and the combustion experiment was conducted during the re-entry. The HyShot payload and flight profile are illustrated in Figure 7 and Figure 8 respectively. After this flight, three more flights have been launched.



Figure 7. HyShot payload

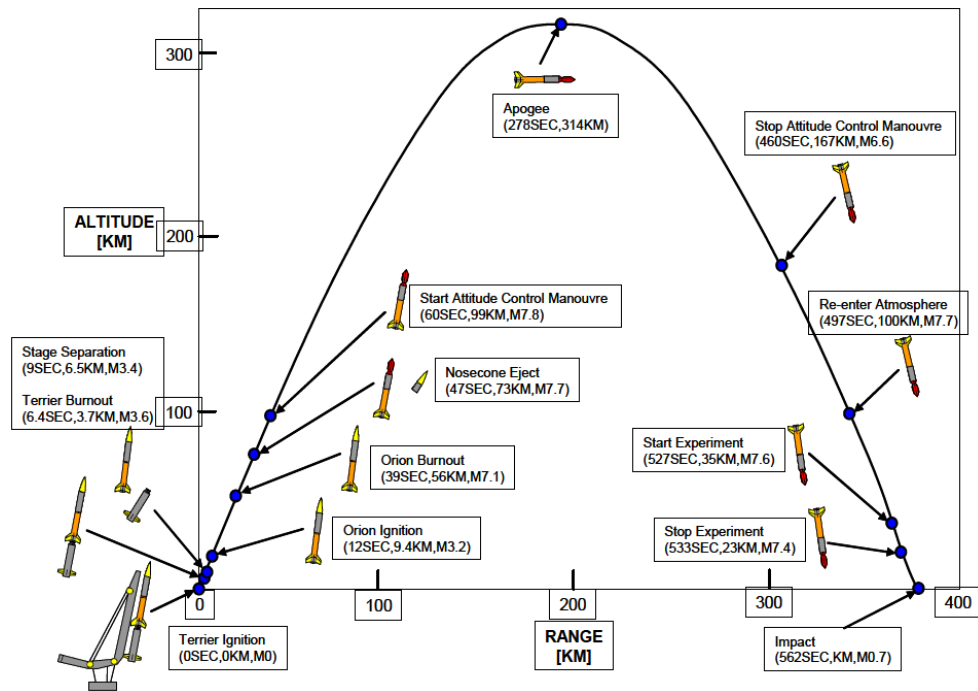


Figure 8. HyShot flight profile

In other countries such as Russia, France or Germany other programs have been developed. In Table 7 and Table 8 of Annex A there is a detailed evolution since the beginnings of scramjet technology until nowadays.

3.3. Applications for a scramjet engine

There is a range of possible applications for scramjet engines, including missile propulsion, hypersonic cruiser propulsion, and part of a staged space access propulsion system. Before going into details, the need for a scramjet engine hydrogen-fuelled to propel a vehicle at Mach 5 or higher will be justified.

Figure 9 displays the approximate performance range in terms of engine specific impulse and Mach number for various types of propulsion systems. It can be seen that at Mach numbers higher than approximately 6-7, the only available propulsion systems are rockets and scramjets. Compared to rockets, scramjets have much higher specific impulse levels (because they do not have to carry on board the oxidizer as they are airbreathing engines and collect oxygen from the atmosphere); therefore, it is clear why it is advantageous to develop the scramjet, if for this reason only. There are other reasons that highlight the advantages of the scramjet development as well. Airbreathing engines produce higher engine efficiency, have longer powered range, possess the ability for thrust modulation to ensure efficient operation, have higher versatility, and are completely reusable.

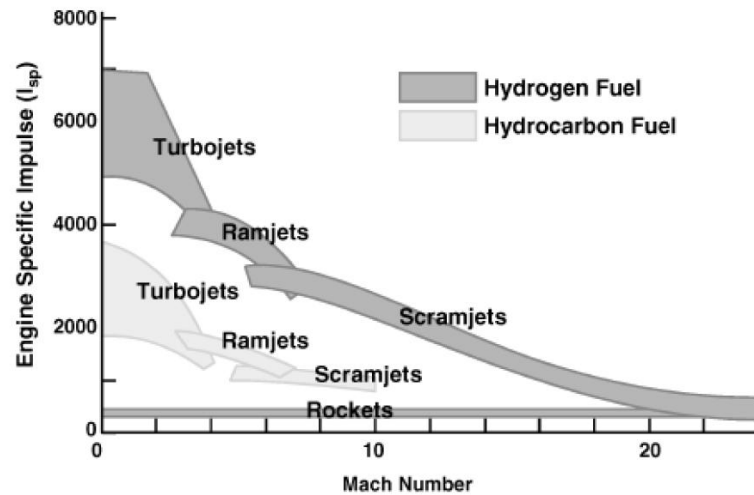


Figure 9. Specific Impulse versus Mach number for various engine types

Figure 10 displays a qualitative chart of propulsion options based on the flight Mach number. The curve represents the approximate altitude required to operate at a given flight Mach number as well as the needed propulsion system. Also shown in this chart is a relative boundary between the two fuel options for scramjets: hydrocarbons and hydrogen. The general consensus is that hydrogen fuel should be used for airbreathing flight faster than approximately Mach 8 (see Section 4.3 for more details). Though hydrogen can perform at higher speeds above the hydrocarbon upper limit, with the current capabilities the hydrogen-fuelled scramjet will only offer acceptable performance to about Mach 15.

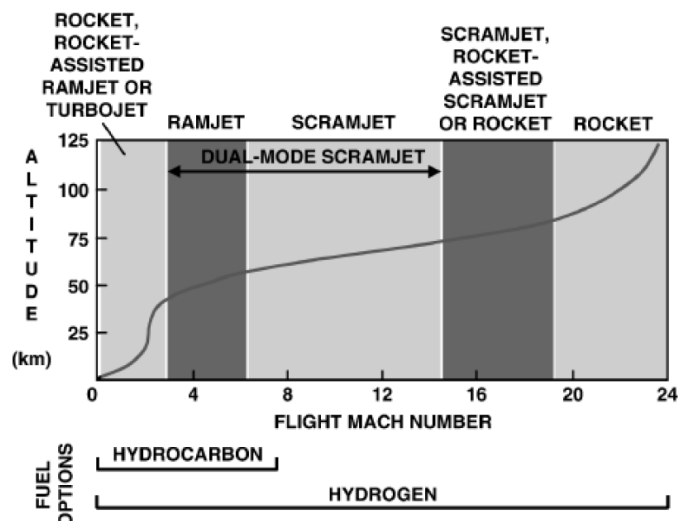


Figure 10. Propulsion system options as a function of Mach number

Next, there is a detailed explanation of some applications for scramjet engines.

- **Space launch applications**

Space launch is one of the potential applications of scramjet engines that have raised the most attention for the past two decades. Airbreathing vehicles, capable of hypersonic speeds, can transform access to space, just like turbojets transformed the airline business. The benefits of using a scramjet for a Single-Stage-to-Orbit (SSTO) vehicle are improved safety, mission flexibility, vehicle design robustness, and reduced operating costs. A SSTO vehicle takes off and lands horizontally like an ordinary aircraft but has the capability to bring payload to lower earth orbits without releasing pieces of its own structure, for example fuel tanks or burn-out rockets.

Safety benefits result from characteristics such as enhanced abort capability and moderate power density. Horizontal takeoff and powered landing allows the ability to abort over most of the flight, both ascent and decent. High lift/drag (L/D) allows longer-range glide for large landing footprint. Power density, or the quantity of propellant pumped for a given thrust level, is 1/10 that of a vertical takeoff rocket due to lower thrust loading (T/W), lower vehicle weight and higher specific impulse. Power density is a large factor in catastrophic failures. Recent analysis indicates that safety increases by several orders of magnitude are possible using airbreathing systems. Mission flexibility results from horizontal takeoff and landing, the large landing (unpowered) footprint and high L/D. Utilization of aerodynamic forces rather than thrust allows efficient orbital plane changes during ascent, and expanded launch window. Robustness and reliability can be built into airbreathing systems because of large margins and reduced weight growth sensitivity, and the low thrust required for smaller, horizontal takeoff systems. Cost models indicate that about one-order magnitude reduction in operating cost is possible. Attributes for selected airbreathing assisted launch systems categorized by staging Mach number and reusable or expandable second stage are listed in Table 1. What it might be observed is that increasing staging Mach number plus adding a reusable second stage, increases the payload fraction and reliability, and reduces both loss of the vehicle and operating cost. The most significant benefit is in safety, quantified by the attribute "Loss of Vehicle/Payload".

Attributes	Baseline ELV	Baseline Space Shuttle	Mach 7 Stage	Mach 10 Stage	Mach 15 Stage	SSTO
	Expendable	Partially Reusable	Expendable 2nd Stage	Reusable	Reusable	Reusable
Payload Fraction	3%	1%	1-2%	3%	4%	5%
Loss of Vehicle/Payload	1: 50	1: 100	1: 4,000	1: 60,000	1: 110,000	1: 160,000
Cost per Lb to LEO	\$2,500	\$10,000	\$1,700	\$2,000	\$1,400	\$1,000

Table 1. Attributes of space launch systems

Despite all of these benefits, remaining uncertainties related to this technology make impossible to conclude on the real feasibility of such SSTO launcher. A combined propulsion could improve the feasibility of a SSTO if the airbreathing mode is used on a very large flight Mach number range (from about 2 to 12), but this implies to develop a very complex propulsion system. Moreover, up to now, no known airbreathing engine is capable of operating at orbital speeds within the atmosphere (hydrogen-fuelled scramjets seem to have a top speed of about Mach 15) or have sufficient acceleration level in the whole airbreathing mode for orbit insertion.

- **Military applications**

The vehicle that could most quickly benefit from current scramjet research is the cruise missile, as it is explained in the following points:

- The space application draws maximum benefit from airbreathing propulsion when using it up to Mach 10-12, in order to optimize the staging of the different propulsion modes. On the contrary, the military interest of high speeds can be reached significantly below this domain. Mach 8 should not be very far from the upper limit for missile applications.
- In its whole flight envelope, the space launcher has to provide a very large acceleration, which is one of the key parameters to provide sufficient payload performances into orbit. A cruising military system has naturally less needs in terms of acceleration capability at high speed.
- Test facilities, developed in some programs, were designed to test components of the propulsion system of a launcher at much reduced scale and in a limited flight Mach number conditions range, but they nearly enable to test a missile engine at full scale. This situation contributes to reduce the uncertainties remaining after ground tests to get to flight tests.

- Finally, it is clear that if a flight demonstration was made using a vehicle whose size would have been chosen minimal for together preserving the demonstration interest of the operation, and limiting the cost, this minimal size would probably be not very far from the size of a missile. Consequently, the success of the flight demonstration would validate the methodology used to develop the experimental vehicle, so that this methodology would also be applicable for any kind of vehicle of similar size and level of integration.

Then, different possible military applications can be proposed:

- Tactical missile when penetration is the key factor or when pure speed is necessary against time targets
- High speed reconnaissance drone with improved mission safety and response time capability
- Global range rapid intervention system based on previously mentioned missiles and drones
- Global range military aircraft or UCAV
- Short response time space launching system

- **Civil applications**

On the other hand, for civil applications, a hypersonic cruiser aircraft that is an alternative to traditional turbojet or turbofan transportation could also be a not-too-distant possibility. The urge to always fly faster and higher might contribute to develop a scramjet vehicle for a commercial hypersonic flight. However, due to all the problems present in the scramjet technology and the remaining uncertainties, today this possibility stays very far from being a reality.

3.4. Current scramjet engine technology challenges

This section will expose some of the most important pros and cons of the scramjet technology as well as some technical challenges.

One of the greatest advantages is the simplicity of design. A scramjet has no moving parts and the main part of its body is constituted by continuous surfaces. This admits relatively low manufacturing costs for the engine itself. Another significant difference between airbreathing engines and rockets, both of them able to fly at hypersonic speeds, is the fuel for combustion that they have to carry on board. While a rocket must carry the oxidizer on board, a scramjet collect it from the atmosphere; thus, this last would be lighter and hopefully

capable of carrying more payload, since in a rocket the 75 percent of the total start weight is the oxidizer. So, that would be a great advantage too.

On the other hand, a scramjet engine has a major inconvenience. It cannot produce thrust if it is not first accelerated to a high velocity around Mach 5-6. This requires one or two additional propulsion systems to propel the vehicle to the needed scramjet start velocity. Therefore, various structures are needed for the suspension of these engines as well as all necessary control systems. All secondary equipment necessary to bring the vehicle to velocities suitable for the scramjet operation makes the whole vehicle heavy, in contrast to what has been mentioned previously. Then, the loss in the dry mass and, consequently, the gain in the payload mass are not so significant. In order to minimize the weight and complexity of having multiple propulsion systems, a dual-mode ramjet/scramjet is often proposed.

The current challenges in the development of the scramjet engine can be gathered in three main areas: air inlet, combustion, and structures and materials.

- **Air inlet**

The overall performance of a scramjet is largely dictated by the aerodynamic performance, geometric size, and weight of the hypersonic inlets. Commonly, hypersonic inlets have a wide Mach number range, but the shock-on-lip condition can be met only at the design Mach number, since shock angles vary with the upstream Mach numbers. Thus, at Mach numbers higher than the design one, the ramp shocks move inside the inlet and evolve into a strong incident shock, causing strong slip layers, remarkable total pressure loss, boundary-layer separation, and possible engine unstart. At Mach numbers lower than the design one, the ramp shocks move away from the cowl lip, causing loss of the precompressed airflow and the so-called spillage drag. To avoid these performance penalties at offdesign conditions, the control of the ramp shock system is needed. Hence, variable geometric approaches for ramp shock control are widely considered and studied.

- **Combustion**

Although the concept of scramjet engines appears simple, supersonic combustion remains a complex field of study. Supersonic combustion is very difficult to maintain and continues to be a formidable task.

The ignition delay time of a fuel-air mixture continues to be the limiting factor for all scramjet engines designs. Decreasing the delay time allows for shorter combustors and/or higher flight velocities. Initially, the ignition delay time

of a fuel is fixed for a given set of conditions and the type of fuel. Increasing the temperature of the fuel and/or air stream reduces this time. Pressure plays a somewhat more complex role. Increasing the pressure, usually, but not always, improves the combustion conditions. Increasing pressure usually reduces the ignition delay time, but there exists a critical value of pressure, above which, the delay time increases dramatically, followed by a slow decrease. So, it is not always advantageous to increase the pressure. The equivalence ratio does not strongly affect the ignition delay time, except for equivalence ratios below 0.3, where the delay time increases sharply. Hydrogen has very low ignition delay time compared with hydrocarbon. Therefore, all these effects need to be considered in designs.

Perhaps the largest problem associated with combustion is the mixing between freestream air and fuel. If fuel cannot be properly injected and mixed into the air stream it will not ignite, regardless of pressure, temperature or equivalence ratio. Due to compressibility effects, fuel injection presents challenging obstacles. The air stream is at such a high pressure and velocity, that fuel injected into the stream has a tendency to be pushed against the wall and rendered ineffective. In addition to the problem of mixing, ignition and flame holding at these high velocities is extremely difficult. To overcome these challenges, several solutions have been proposed like plasma torches, ramps and wedges, or recessed cavities.

Another challenge to increase the performance is the need of a variable geometry combustion chamber. A fixed geometry combustor associated to a variable capture area air inlet does not benefit from the enhanced efficiency of the air inlet. A fully variable geometry – air inlet + combustion chamber – can increase the performance by comparison with the previous concept, but cannot take all the benefit of the complexity related to a fully variable geometry system because of the fixed minimum section of the inlet (equivalent to the fixed section of the combustion chamber entrance). So other concepts have been studied, which consist in modifying at the same time the minimum section of the air inlet and the geometry of the combustion chamber. Moreover, for such concepts, having at disposal a variable minimum section for the air inlet avoids the need of large variation of the air inlet capture area (i.e. increase when the Mach number increases) and permits high efficiency in a wide Mach number range.

- **Structures and materials**

Unlike a rocket that passes nearly vertically through the atmosphere on its way to orbit, a scramjet would take a more levelled trajectory. Because of the thrust-to-weight ratio of a scramjet being low compared to modern rockets, the

scramjet needs more time to accelerate. Such a depressed trajectory implies that the vehicle stays a long time in the atmosphere at hypersonic speeds, causing atmospheric friction to become a problem. This is not only for space launch applications but also in missile or commercial transport applications. Heat addition produced by the combustion at these high velocities and temperatures is another significant factor to take into account. Therefore, the materials chosen for the structure must have good properties and be adequate in front of these phenomena. Furthermore, cooling of the engine's structure by fuel or radiation is essential.

4. Parts of a scramjet engine

In this chapter are described the different parts of a scramjet engine: air inlet, isolator, combustor and nozzle. With the actual technology, as it is mentioned in Chapter 3, the scramjet engine must be integrated with the fuselage of the aircraft, specially the air inlet and the nozzle. Part of the forebody aircraft fuselage makes the function of air inlet compressing the freestream air, and similarly, the aftbody acts as a nozzle expanding the gases from the combustion.

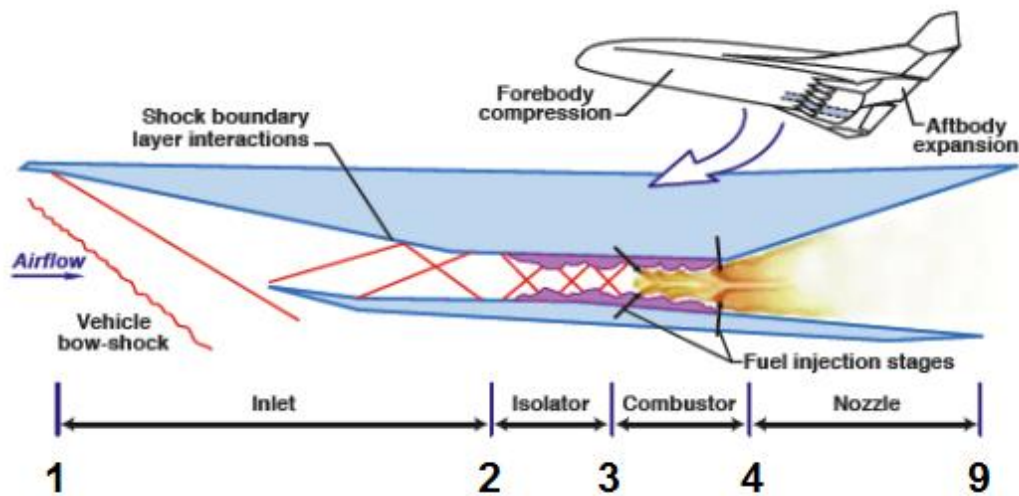


Figure 11. Propulsion-airframe integrated scramjet with station numbering

The flowpath through a scramjet engine follows a Brayton thermodynamic cycle. The air is compressed, after that combustion takes place to increase the flow temperature and pressure, and finally, the products from the combustion are expanded. Next, the different parts of a scramjet in charge of these processes are described.

4.1. Air inlet

The air inlet can be considered as a diffuser in which takes place the compression of the freestream air gathered. This compression is achieved by successive shock waves.

For an oblique shock wave (see Figure 40 of Annex C), the flow is always deflected towards the shock wave, and the flow properties vary as

$$\begin{array}{lll}
M_{2n} < 1 & M_2 < M_1 \\
T_{t2} = T_{t1} & p_{t2} < p_{t1} & \rho_{t2} < \rho_{t1} \\
T_2 > T_1 & p_2 > p_1 & \rho_2 > \rho_1
\end{array}$$

Here the subscript 1 and 2 corresponds respectively just before and just after the shock wave.

Therefore, at the exit of the air inlet, the supersonic freestream air has reduced its velocity and has raised its static temperature and pressure. Furthermore, the total temperature through the air inlet is constant and the total pressure changes

$$\frac{T_{t2}}{T_{t0}} = 1 \quad \frac{p_{t2}}{p_{t0}} < 1$$

The subscript 0 represents freestream conditions before forebody compression.

The ratio between the total pressure at the station 0 and 2 (π_d) characterizes the inlet's pressure performance and consists of two contributions

$$\pi_d = \pi_{d_{max}} \eta_r \quad (4.1)$$

$\pi_{d_{max}}$ represents the part due to viscosity effects, while η_r is called recovery factor and characterizes the contribution of compressibility effects. Both factors imply total pressure losses within the inlet.

The performance of the air inlet compression can be separated into two key parameters: capability, or how much compression is performed, and efficiency, or what level of flow losses does the inlet generate during the compression process. A common parameter used to quantify the efficiency of the forebody/inlet compression is the kinetic energy efficiency η_d . The definition of η_d is the ratio of the kinetic energy the compressed flow would achieve if it were expanded isentropically to freestream pressure, relative to the kinetic energy of the freestream

$$\eta_d = \frac{\frac{1}{2} u_2'^2}{\frac{1}{2} u_0^2} = \frac{u_2'^2}{u_0^2} \quad (4.2)$$

Both parameters, total pressure ratio and kinetic energy efficiency, can be related through the expression

$$\pi_d = \left[1 + (1 - \eta_d) \frac{\gamma - 1}{2} M_0^2 \right]^{\frac{-\gamma}{\gamma - 1}} \quad (4.3)$$

See Annex C for more details on this expression, as well as on the equations governing shock waves.

Hypersonic inlets used in scramjets fall into three-different categories, based on the type of compression that is utilized. These three types are: external compression, mixed compression and internal compression. A schematic of these types is shown in Figure 12. In the external compression all the compression is performed by flow turning in one direction by shock waves that are external to the engine. These inlet configurations have large cowl drag, as the flow entering the combustor is at a large angle relative to the freestream flow; however, external compression inlets are self-starting and spill flow when operated below the design Mach number (this is a desirable feature for inlets that must operate over a large Mach number range). In a mixed compression inlet the compression is performed by shocks both external and internal to the engine, and the angle of the external cowl relative to the freestream can be made very small to minimize external drag. These inlets are typically longer than external compression configurations, but also spill flow when operated below the design Mach number. Depending on the amount of internal compression, however, mixed compression inlets may need variable geometry in order to start. In internal compression inlet the compression is performed by shock waves that are internal to the engine. This type of inlet can be shorter than a mixed compression inlet, but it does not allow easy integration with the vehicle. It maintains full capture at Mach numbers lower than the design point, but its most significant limitation is that extensive variable geometry is always required for it to start.

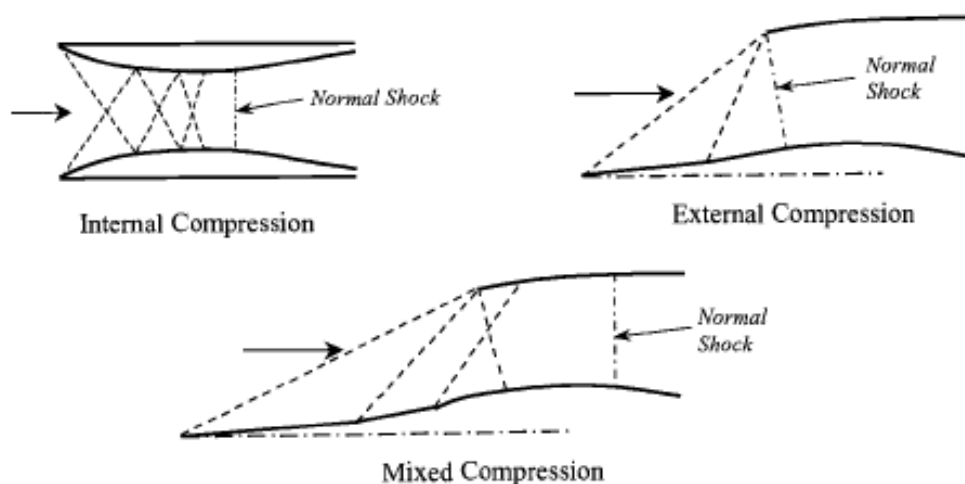


Figure 12. Types of supersonic air inlets

4.2. Isolator

At flight speeds below Mach 8, combustion in a scramjet engine can generate a large local pressure rise and separation of the boundary layer on the surfaces of the combustion duct. This separation, which can feed upstream of fuel injection, acts to further diffuse the core flow in the duct, and will affect the operation of the inlet, possibly causing an unstart of the engine. The method used to alleviate this problem is the installation of a short duct between the inlet and the combustor known as an isolator. In some engines (those which operate in the lower hypersonic regime between Mach 4 and 8) the combination of the diffusion in the isolator and heat release in the combustion decelerate the core flow to subsonic conditions, in what is called dual-mode combustion. At speeds above Mach 8 the increased kinetic energy of the airflow through the engine means that the combustion generated pressure rise is not strong enough to cause boundary layer separation. Flow remains attached and supersonic throughout, and this is termed pure scramjet. In this case an isolator is not necessary.

The structure of the supersonic flow in confined ducts under the influence of a strong adverse pressure gradient is of interest in the design of scramjet isolators. As shown in Figure 13, a pressure gradient is imposed on the incoming supersonic flow, and with the presence of a boundary layer, a series of crossing oblique shocks are generated. This phenomenon, known as pseudo shock or shock-train, is characterized by a region of separated flow next to the wall, together with a supersonic core that experiences a pressure gradient due to the area restriction of the separation and forms the series of oblique shocks mentioned before. Finally, the flow reattaches at some point and mixes out to conditions that match the imposed back-pressure. Being able to predict the length scale of this flow structure is the key component of isolator design for dual-mode scramjets.

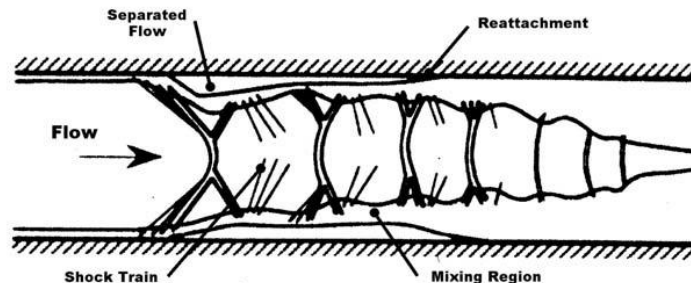


Figure 13. Schematic of flow structure in an isolator

4.3. Combustor

The combustor chamber is a duct where the combustion between freestream air and fuel takes place. This combustion is supersonic, so there are some aspects that require more attention on the contrary of the conventional combustion. Next, these aspects will be commented.

At very high velocities, a properly fuel injection and mixing could be a problem, as well as flame holding. That is why over the past decades a lot of different configurations have been studied and developed. Some techniques used today for fuel injection in scramjet engines are: wall, ramp, strut, pylon and pulsed injectors. And for keeping the combustion, there is a technique quite used called cavity flame holders.

Another significant aspect to take into account is the dissociation. At the entrance of the combustor the flow static temperature and pressure are very high, and with the heat release due to chemical reactions, the temperature and pressure could reach extremely high values which involve dissociation of combustion products.

Because of the heat addition, the velocity or Mach number decreases while the static temperature and pressure increases. The total temperature is raised and the total pressure is reduced. The total pressure loss is proportional to the square of Mach number; hence, it is better to have a small combustor inlet Mach number, on the contrary for the dissociation phenomenon. In Section 4.4 there is a discussion about the optimum Mach number at the entrance of the combustor.

Finally, the fuel used in scramjet engines is hydrogen or hydrocarbons. Hydrogen is most used because it has more advantages in front of hydrocarbons. The reason for using liquid hydrogen for scramjet fuel rests with its high specific impulse and its potential for cooling parts of the vehicle. The heat value (which represents the amount of energy released when a fuel is combusted) for hydrogen is two and a half times that of hydrocarbons. Hydrogen is also extremely flammable and it has a wide flammability range (it can burn when it occupies between 4 - 74% of the air volume). Another advantage over hydrocarbons is that hydrogen is a clean fuel as it doesn't produce any harmful pollutants like carbon monoxide (CO) or carbon dioxide (CO₂) during the combustion process. The only product from its combustion is water, which can be safely exhausted into the atmosphere.

Although it may appear that hydrogen is the ideal fuel for scramjet propulsion it does present some drawbacks. Liquid hydrogen is not a dense fuel, having a density of only 0.09 kg/m^3 . For example, JP-8 on the other hand has a density of 800 kg/m^3 in similar conditions, very much higher. Having a low density does save weight; however, a large volume is needed in order to store enough chemical energy for practical use.

Even with the above limitations hydrogen has been the clear choice for many scramjet researchers due to its versatility and performance, and it is also clear that hydrogen will be the preferred fuel for future projects and developments using scramjet technology.

4.4. Nozzle

The nozzle is a divergent duct that accelerates the supersonic flow and at the same time expands it reducing its static temperature and pressure. The expansion process converts the potential energy of the combusting flow to kinetic energy and then it results in thrust. An ideal expansion nozzle would expand the engine plume isentropically to the freestream pressure assuming chemical equilibrium. Nevertheless, loss mechanisms are present in real expansion processes and are due to under-expansion, failure to recombine dissociated species, flow angularity and viscous losses.

The weight of a fully-expanded nozzle would be prohibitive at most hypersonic flight conditions; hence under-expansion losses are usually traded against vehicle structural weight. Dissociation losses result from chemical freezing in the rapid expansion process in the nozzle, essentially locking up energy that cannot be converted to thrust. Flow angularity losses are product of varying flow conditions in the nozzle, and viscous losses are associated with friction on the nozzle surfaces.

The flow enters the nozzle in a highly reactive state. As it expands to lower pressure and temperature, chemical reactions will occur toward the completion of combustion, with consequent additional heat release. If the expansion is slow enough chemical equilibrium is approached, but in most cases, due to the high velocities reached in a scramjet, the flow composition freezes and becomes fixed. Two limiting cases can be treated fairly easily: equilibrium flow, where equilibrium is maintained through all nozzle length, and frozen flow, where the flow doesn't change its composition from the combustor exit. The true situation lies between these two cases.

The choice of combustor inlet Mach number is a key aspect for the performance of the scramjet and it is related to the nozzle expansion. If the static temperature at the combustor entrance is too high, dissociation will be present and then chemical energy is not available as thermal energy for conversion to kinetic energy in the nozzle. So, the question to be dealt with quantitatively is then what static temperature, or what combustor inlet Mach number, is best for any given flight Mach number. The existence of such an optimum M_3 , which depends on finite chemical reaction rates, can be seen by comparison of the specific impulse for two limiting cases: one which chemical equilibrium is assumed throughout the flow, and another in which the flow is assumed to be in equilibrium up to the combustor exit but frozen at that composition during the nozzle expansion.

As it can be seen in Figure 14, for equilibrium nozzle flow there is no optimum M_3 , the specific impulse increases continuously as M_3 decreases. This is not surprising, because for equilibrium flow the chemical energy invested in dissociation is recovered as thermal energy and then kinetic energy as recombination occurs in the nozzle, and the lower the combustor Mach number the lower the entropy increase in the combustor. Therefore, independently on the flight Mach number interests a low combustor inlet Mach number.

In contrast, for frozen nozzle flow (Figure 15), there is a clear optimum M_3 for flight Mach numbers above about 10. It is defined by the envelope, drawn as a dashed line. The optimum value of M_3 depends on the extent to which recombination occurs in the nozzle, as well as on the degree of dissociation at the combustor exit. For a very high flight Mach number, if the flow is decelerated to a very low M_3 , the total pressure loss will be small but then losses of dissociation will be too high, and in the opposite case, if the flow is slowed to a relative high M_3 , dissociation losses will be small but the total pressure loss will be very elevated. So, balancing each term it can be found an optimum combustor inlet Mach number.

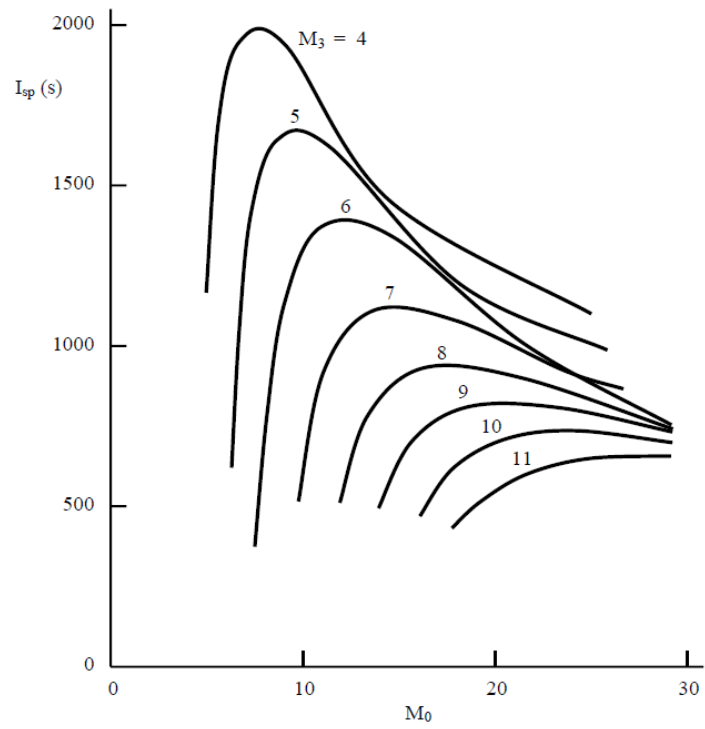


Figure 14. Specific impulse for equilibrium nozzle flow (combustor pressure fixed at 1 atm)

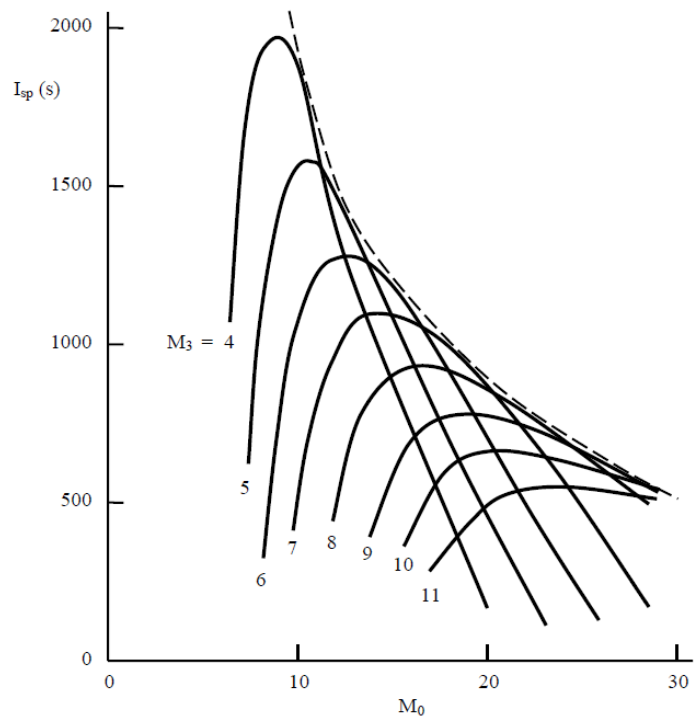


Figure 15. Specific impulse for frozen nozzle flow (combustor pressure fixed at 1 atm)

5. Combustion model

Due to the relevance impact the combustion has on the overall efficiency of a scramjet, this chapter presents a model to simulate the phenomenon that takes place in a scramjet combustor. The combustor involves thermodynamics and dynamics of fluid flow coupled to combustion, which can be considered a multi-stage heat releasing mechanism. In order to avoid the expensive computationally processes by solving Navier-Stokes equations in conjunction with a turbulent model, a quasi-one-dimensional solver is proposed in this section.

The quasi-one-dimensional model uses a unique formulation of fluid motion equations and chemical kinetics. It also includes wall skin friction, wall heat transfer, duct area changes and fuel-air mixing. This last effect must be taken into account for its relevance in the total pressure loss which is about as the same magnitude as losses due to wall skin friction.

The governing equations that will be presented next are based on the general following assumptions:

- Quasi-one-dimensional flow (therefore, all flow variables are functions of the axial distance x along the combustor).
- Steady-state flow (so temporal terms are neglected).
- Continuous flow (so changes in stream properties are continuous)
- The flow behaves as a semi-perfect gas (internal energy, enthalpy and specific heat are only T-dependant).

5.1. Fluid motion equations

To develop the combustion model, firstly it is necessary to derive the equations governing the motion of a fluid. They are the conservation of mass, momentum and energy. See Annex B for a more detailed development of the equations.

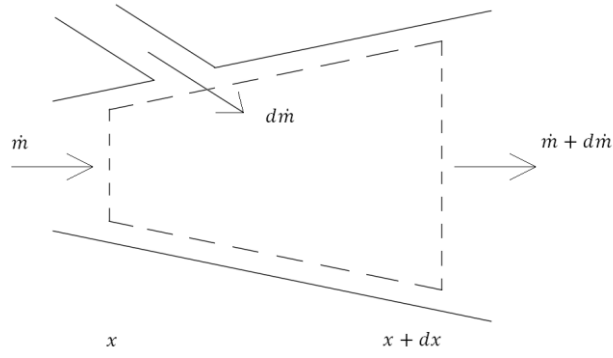


Figure 16. Control volume for developing the governing equations of the combustion model

5.1.1. Mass conservation

From the integral expression

$$\dot{m} = \rho u A \quad (5.1)$$

Is obtained

$$\frac{1}{\dot{m}} \frac{d\dot{m}}{dx} = \frac{1}{\rho} \frac{d\rho}{dx} + \frac{1}{u} \frac{du}{dx} + \frac{1}{A} \frac{dA}{dx} \quad (5.2)$$

Where \dot{m} is the mass flow rate of the gases (reactive and products in gaseous phase). Therefore, as fuel injected is mixed with air, \dot{m} increases while \dot{m}_f decreases to keep constant the total mass flow rate

$$\dot{m}_{tot} = \dot{m}_a + \dot{m}_{of} = \dot{m}_a + \dot{m}_{fm} + \dot{m}_f = \dot{m} + \dot{m}_f = ct \quad (5.3)$$

Notice the difference between \dot{m}_{fm} and \dot{m}_f , the sum of them gives \dot{m}_{of} . The fuel mass flow rate that passes through the injectors is \dot{m}_{of} and it can be separated into two fractions: one which is already mixed with the freestream air (\dot{m}_{fm}) and the other one which stills to be mixed (\dot{m}_f). Analogously, it is possible to define the ratios of both variables, $\frac{d\dot{m}_{fm}}{dx}$ and $\frac{d\dot{m}_f}{dx}$, which according to its definition they meet the following relation

$$\frac{d\dot{m}_f}{dx} = - \frac{d\dot{m}_{fm}}{dx} \quad (5.4)$$

Since $\dot{m} = \dot{m}_a + \dot{m}_{fm}$, the ratio of fuel that is being mixed is equal to the ratio which increases \dot{m} ; thus it can be stated the relation

$$\frac{d\dot{m}_f}{dx} = - \frac{d\dot{m}}{dx} \quad (5.5)$$

5.1.2. Momentum conservation

The net force acting on the control volume is equal to the increase of momentum flux of the streams flowing through the control volume. Considering only forces in the direction of flow and neglecting body forces, the conservation of momentum yields

$$(pA)|_x - (pA)|_{x+\Delta x} + \int_x^{x+\Delta x} p dA - \int_x^{x+\Delta x} F_{wall} dx - \int_x^{x+\Delta x} F_{mix} dx = (\dot{m}u + \dot{m}_f u_f)|_{x+\Delta x} - (\dot{m}u + \dot{m}_f u_f)|_x \quad (5.6)$$

The integral of F_{wall} represents the losses from wall skin friction whereas the integral of F_{mix} are the losses from fuel-air mixing.

Dividing by $\Delta x \rightarrow 0$ is obtained

$$-\frac{dp}{dx}A - F_{wall} - F_{mix} = \frac{d}{dx}(\dot{m}u + \dot{m}_f u_f) \quad (5.7)$$

Considering

$$\left| \dot{m}_f \frac{du_f}{dx} \right| \ll \left| \dot{m} \frac{du}{dx} \right| \quad (5.8)^1$$

$$u_f = u\varepsilon \quad (5.9)^2$$

Taking into account Eq. (5.5) and the definitions of F_{wall} and F_{mix}

$$F_{wall} = \frac{1}{2}\rho u^2 c_f P_w \quad (5.10)^3$$

$$F_{mix} = \frac{1}{2}\rho u^2 c_{fj} P_{fj} \quad (5.11)^4$$

Momentum equation can be expressed as

$$\frac{dp}{dx} = -\left(\frac{1}{2}\rho u^2 c_f \frac{P_w}{A} + \frac{1}{2}\rho u^2 c_{fj} \frac{P_{fj}}{A} + \rho u \frac{du}{dx} + \frac{1}{A} \frac{d\dot{m}}{dx} u(1 - \varepsilon) \right) \quad (5.12)$$

¹ This assumption is valid because the fuel mass flow rate which is not mixed is much smaller than the mass flow rate of the gases through the whole length of combustor.

² This equation accounts for angled fuel injection ($\varepsilon = 0$ for normal fuel injection and $\varepsilon = 1$ for parallel fuel injection) and the velocity of the fuel fraction not mixed can be associated to the velocity of fuel injection in the x direction.

³ The wall skin friction force is function of the dynamic pressure, the perimeter of the duct and the friction coefficient, which might be defined from experimental results [24].

⁴ Analogously to the wall skin friction, the fuel-air mixing friction force can be written in function of the dynamic pressure, and a kind of perimeter and friction coefficient of the wetted area between fuel and air. See Section 5.6 for more details.

5.1.3. Energy conservation

Neglecting the dissipative, transport phenomena of viscosity, axial mass diffusion and axial thermal conductivity, the conservation of energy states that the work done by pressure forces acting on the control volume plus the heat transferred into the control volume is equal to the net amount of energy flow within the control volume

$$\begin{aligned} (puA + p_f u_f A_f)|_x - (puA + p_f u_f A_f)|_{x+\Delta x} + \int_x^{x+\Delta x} \dot{q} P_w dx \\ = (\dot{m} e_t + \dot{m}_f e_{tf})|_{x+\Delta x} - (\dot{m} e_t + \dot{m}_f e_{tf})|_x \end{aligned} \quad (5.13)$$

Dividing by $\Delta x \rightarrow 0$ is obtained

$$-\frac{d(puA)}{dx} + \dot{q} P_w = \frac{d}{dx} (\dot{m} e_t + \dot{m}_f e_{tf}) \quad (5.14)$$

Remembering the definitions of the total energy and the total enthalpy

$$e_t = h_t - \frac{p}{\rho} \quad (5.15)$$

$$h_t = h + \frac{1}{2} u^2 \quad (5.16)$$

Using Eq. (5.5) and considering

$$p_f = p \quad (5.17)^5$$

$$\left| \frac{1}{2} \dot{m}_f u_f^2 \right| \ll \left| \frac{1}{2} \dot{m} u^2 \right| \quad (5.18)^6$$

$$\left| \dot{m}_f \frac{dh_f}{dx} \right| \ll \left| \dot{m} \frac{dh}{dx} \right| \quad (5.19)^7$$

Energy equation is

$$\frac{dh}{dx} = -\frac{1}{\dot{m}} \frac{d\dot{m}}{dx} \left(h + \frac{1}{2} u^2 \right) + \frac{1}{\dot{m}} \frac{d\dot{m}}{dx} h_f - u \frac{du}{dx} + \frac{\dot{q} P_w}{\dot{m}} \quad (5.20)$$

And in terms of temperature

⁵ The fuel injection pressure is supposed to be equal to the gas pressure within the combustor.

⁶ The kinetic energy of the fuel is negligible in front of the kinetic energy of the mixture.

⁷ This assumption is valid because the fuel mass flow rate which is not mixed is much smaller than the mass flow rate of the gases through the whole length of combustor.

$$\frac{dT}{dx} = \frac{1}{c_p} \left[- \sum_i \left(h_i \frac{dY_i}{dx} \right) - \frac{1}{\dot{m}} \frac{d\dot{m}}{dx} \left(h + \frac{1}{2} u^2 \right) + \frac{1}{\dot{m}} \frac{d\dot{m}}{dx} h_f - u \frac{du}{dx} + \frac{\dot{q} P_w}{\dot{m}} \right] \quad (5.21)$$

Where specific heat capacity and specific static enthalpy are obtained weighting the values of each species from mass fractions

$$c_p = \sum_{i=1}^{N_i} c_{p_i} Y_i \quad (5.22)$$

$$h = \sum_{i=1}^{N_i} h_i Y_i \quad (5.23)$$

The heat release due to combustion will be dissipated through chamber walls. The heat-transfer term, which accounts for this phenomenon, is calculated from the definition of the Stanton number

$$C_H = \frac{\dot{q}}{\rho u (h_{aw} - h_w)} \quad (5.24)$$

The Stanton number can be related to the friction coefficient by Reynolds analogy

$$C_H = \frac{c_f R_f}{2} \quad (5.25)$$

Then, the heat-transfer term can be written as

$$\frac{\dot{q} P_w}{\dot{m}} = \frac{c_f R_f (h_{aw} - h_w) P_w}{2A} \quad (5.26)$$

Where R_f is the Reynolds analogy factor, h_{aw} and h_w are the adiabatic wall enthalpy and the wall enthalpy respectively, and P_w and A are the perimeter and the area of the section. The adiabatic wall enthalpy may be expressed in terms of a recovery factor r as

$$h_{aw} = h + r \frac{u^2}{2} \quad (5.27)$$

The recovery factor is typically written in terms of the Prandtl number as

$$r = Pr^{1/2} \quad \text{for laminar flow} \quad (5.28)$$

$$r = Pr^{1/3} \quad \text{for turbulent flow} \quad (5.29)$$

For laminar flow, the Reynolds analogy factor is typically assumed to be $R_f = Pr^{-2/3}$. And for turbulent flow, a value of $R_f = 1.1$ is often used.

The laminar Prandtl number ($Pr \approx 0.71$ for air) has been observed that is a good approximation for a widely range of Mach numbers.

5.2. Equation of state

As it is seen in the previous section, three equations have been developed, whereas there are four unknown variables (velocity, density, pressure and temperature). Therefore, to close the problem it is necessary to add an extra equation. It comes from the ideal gas law

$$p = \frac{\rho RT}{\overline{MW}} \quad (5.30)$$

Or in a differential form

$$\frac{1}{p} \frac{dp}{dx} = \frac{1}{\rho} \frac{d\rho}{dx} + \frac{1}{T} \frac{dT}{dx} - \frac{1}{\overline{MW}} \frac{d\overline{MW}}{dx} \quad (5.31)$$

Where the mixture molecular weight and its derivative are defined as

$$\overline{MW} = \frac{1}{\sum_i \frac{Y_i}{MW_i}} \quad (5.32)$$

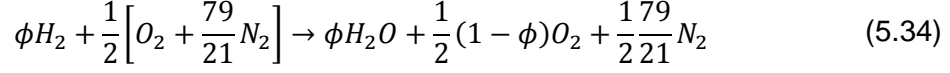
$$\frac{d\overline{MW}}{dx} = -\overline{MW}^2 \left(\sum_i \frac{1}{MW_i} \frac{dY_i}{dx} \right) \quad (5.33)$$

5.3. Combustion

In fact, the problem is not closed at all because the mass fractions of each species are not known a priori when chemical reactions occur. So, it is essential to include N_i equations for the N_i species present in the mass flow. Next, three types of combustion will be considered.

5.3.1. Combustion without dissociation

Considering the general case of off-stoichiometric reactions, the equilibrium air-hydrogen reaction is



Where ϕ is the equivalence ratio defined as the ratio of the actual fuel-air ratio to the stoichiometric fuel-air ratio

$$\phi = \frac{f}{f_{st}} \quad (5.35)$$

Notice that when $\phi = 1$ it is obtained the stoichiometric reaction, whereas if $\phi > 1$ the reaction is fuel-rich and if $\phi < 1$ it is fuel-lean. However, the aviation propulsion usually deals with fuel-lean mixtures. Thus, in the current model the equivalence ratio will be equal or inferior to the unity. Notice also that nitrogen (N_2) acts merely as an inert diluent, absorbing some of the sensible thermal energy released by combustion by virtue of its specific heat capacity.

Finally, comment that off-stoichiometric fuel-air ratios, as characterized by the equivalence ratio $\phi \neq 1$, affect the type and distribution of combustion products, as well as the temperature.

For definition, the mass fraction of species i is

$$Y_i = \frac{m_i}{m} = \frac{m_i}{\sum_i m_i} \quad (5.36)$$

And the rate of change of each species mass fraction is determined by the rate of change of local equivalence ratio that, in turn, is set by the fuel injection rate along the duct. The changes in local equivalence ratio and species mass fraction are controlled by

$$\frac{d\phi}{dx} = \frac{d\dot{m}_{fm}}{dx} \frac{1}{\dot{m}_a f_{st}} \quad (5.37)$$

$$\frac{dY_i}{dx} = \frac{dY_i}{d\phi} \frac{d\phi}{dx} \quad (5.38)$$

Then, mass fractions of reaction products and its differential form are

$$Y_{N_2} = \frac{\frac{1}{2} \frac{79}{21} MW_{N_2}}{m} \quad (5.39)$$

$$Y_{O_2} = \frac{\frac{1}{2}(1 - \phi)MW_{O_2}}{m} \quad (5.40)$$

$$Y_{H_2O} = \frac{\phi MW_{H_2O}}{m} \quad (5.41)$$

$$\frac{dY_{N_2}}{dx} = \frac{-\frac{1}{2}\frac{79}{21}MW_{N_2}\left(MW_{H_2O} - \frac{1}{2}MW_{O_2}\right)}{m^2} \frac{d\phi}{dx} \quad (5.42)$$

$$\frac{dY_{O_2}}{dx} = \frac{-\frac{1}{2}MW_{O_2}\left(m + (1 - \phi)\left(MW_{H_2O} - \frac{1}{2}MW_{O_2}\right)\right)}{m^2} \frac{d\phi}{dx} \quad (5.43)$$

$$\frac{dY_{H_2O}}{dx} = \frac{MW_{H_2O}\left(m - \phi\left(MW_{H_2O} - \frac{1}{2}MW_{O_2}\right)\right)}{m^2} \frac{d\phi}{dx} \quad (5.44)$$

Where the total mass of product gases and the equivalence ratio are respectively

$$m = \phi MW_{H_2O} + \frac{1}{2}\frac{79}{21}MW_{N_2} + \frac{1}{2}(1 - \phi)MW_{O_2} \quad (5.45)$$

$$\phi = \frac{\dot{m}_f m}{\dot{m}_a f_{st}} \quad (5.46)$$

5.3.2. Combustion with equilibrium dissociation

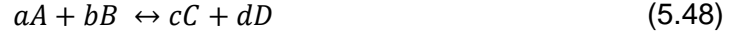
In reality the reaction products of Eq. (5.34) will dissociate into other molecular fragments at elevated temperature. Oxygen and hydrogen start to dissociate about 2500K and nitrogen at 4000K approximately. Therefore, the atom balance equation for the air-hydrogen reaction can be generalized as

$$\begin{aligned} \phi H_2 + \frac{1}{2}\left[O_2 + \frac{79}{21}N_2\right] \\ \rightarrow n_{H_2O}H_2O + n_{N_2}N_2 + n_{O_2}O_2 + n_{H_2}H_2 + n_H H + n_O O \\ + n_{OH}OH + n_{HO_2}HO_2 + n_{H_2O_2}H_2O_2 + n_{NO_2}NO_2 + etc. \end{aligned} \quad (5.47)$$

Where etc. indicates that the list of possible product gases may be as many combinations of H , O and N atoms as exist in nature.

If reaction rates are large relative to the rate of the phenomenon that is changing the thermodynamic state of the gas it is said that chemical reactions

proceed to a condition of chemical equilibrium⁸. In this situation there is a function K_p of T alone. Considering for example the generic stoichiometric reaction

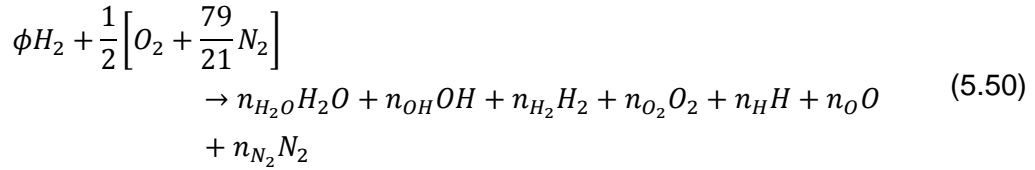


The equilibrium constant based on pressures K_p is

$$K_p(T) = \frac{p_C^c p_D^d}{p_A^a p_B^b} \quad (5.49)$$

The set of Eqs. (5.49) plus the statement that elements are conserved in chemical reactions serve to relate the pressure of any chemical species to those of the elements of which it is composed, as functions of temperature and gas pressure. Therefore, setting the temperature and gas pressure permits to find the composition of each species within a reaction.

For example, suppose that air and hydrogen react to form H_2O , OH , H_2 , O_2 , H , O and N_2 according to



Where ϕ is prescribed and it is wanted to find n_i . Consider the following equilibrium equations

$$H_2 + \frac{1}{2} O_2 \leftrightarrow H_2O, \quad K_{p,f}(H_2O) = \frac{p_{H_2O}}{(p_{H_2})(p_{O_2})^{1/2}} \quad (5.51)$$

$$\frac{1}{2} H_2 \leftrightarrow H, \quad K_{p,f}(H) = \frac{p_H}{(p_{H_2})^{1/2}} \quad (5.52)$$

$$\frac{1}{2} O_2 \leftrightarrow O, \quad K_{p,f}(O) = \frac{p_O}{(p_{O_2})^{1/2}} \quad (5.53)$$

$$\frac{1}{2} H_2 + \frac{1}{2} O_2 \leftrightarrow OH, \quad K_{p,f}(OH) = \frac{p_{OH}}{(p_{H_2})^{1/2} (p_{O_2})^{1/2}} \quad (5.54)$$

For each equilibrium equation, it is

⁸ Equilibrium at combustion chamber does not imply that in the subsequent nozzle expansion the chemical equilibrium will be granted.

$$\sum_{i=1}^{N_{i,r}} \ln p_i^{v_{i,r}} = - \sum_{i=1}^{N_{i,r}} v_{i,r} \frac{G_i^{p_{ref}=1}}{RT} \quad (5.55)$$

Where $N_{i,r}$ is the total number of species within each equation, v_i stands for the numerical coefficients (defined negative for those on the left side and positive for the ones on the right side of each partial equilibrium reaction), and $G_i^{p_{ref}=1}$ stands for the Gibbs function of each specie at a pressure of 1 atm

$$G_i^{p_{ref}=1} = h_i - T \left[\int_{T_{ref}}^T c_{pi} \frac{dT}{T} + R \ln p_{ref} + s_{i,ref} \right] \quad (5.56)$$

Then, one gets four equations relating partial pressures and temperatures. And at the same time the partial pressures are related with mole fractions

$$p_{H_2O} = \frac{n_{H_2O}}{n_{H_2O} + n_{OH} + n_{H_2} + n_{O_2} + n_H + n_O + n_{N_2}} p \quad (5.57)$$

$$p_{OH} = \frac{n_{OH}}{n_{H_2O} + n_{OH} + n_{H_2} + n_{O_2} + n_H + n_O + n_{N_2}} p \quad (5.58)$$

$$p_{H_2} = \frac{n_{H_2}}{n_{H_2O} + n_{OH} + n_{H_2} + n_{O_2} + n_H + n_O + n_{N_2}} p \quad (5.59)$$

$$p_{O_2} = \frac{n_{O_2}}{n_{H_2O} + n_{OH} + n_{H_2} + n_{O_2} + n_H + n_O + n_{N_2}} p \quad (5.60)$$

$$p_H = \frac{n_H}{n_{H_2O} + n_{OH} + n_{H_2} + n_{O_2} + n_H + n_O + n_{N_2}} p \quad (5.61)$$

$$p_O = \frac{n_O}{n_{H_2O} + n_{OH} + n_{H_2} + n_{O_2} + n_H + n_O + n_{N_2}} p \quad (5.62)$$

$$p_{N_2} = \frac{n_{N_2}}{n_{H_2O} + n_{OH} + n_{H_2} + n_{O_2} + n_H + n_O + n_{N_2}} p \quad (5.63)$$

If all pressures are expressed in atmosphere, then, since $p_{ref} = 1 \text{ atm}$, the logarithm in Eq. (5.56) will be zero.

Notice that nitrogen (N_2) is not dissociated and it acts as an inert gas, so its composition within the products is kept constant ($n_{N_2} = \frac{1}{2} \frac{79}{21}$). However, conservation of elements is required for H and O

$$2\phi = 2n_{H_2O} + n_{OH} + 2n_{H_2} + n_H \quad (5.64)$$

$$1 = n_{H_2O} + n_{OH} + 2n_{O_2} + n_O \quad (5.65)$$

Two methods of resolution are exposed subsequently:

- 1) Substituting Eqs. (5.57) to (5.62) in Eqs. (5.51) to (5.54), and using Eqs. (5.64) and (5.65), it is obtained a non linear system of six equations and six unknowns (n_{H_2O} , n_{OH} , n_{H_2} , n_{O_2} , n_H and n_O) for given values of ϕ , T and p . This system can be solved using the Newton – Raphson method.
- 2) The other alternative is solved by iteration:
 - a) Assume guess values for n_{H_2O} , n_{OH} , n_{H_2} , n_{O_2} , n_H and n_O .
 - b) Compute partial pressures p_{H_2O} , p_{OH} , p_{H_2} , p_{O_2} , p_H and p_O that result from Eqs. (5.57) to (5.62).
 - c) Compute new values of p_{H_2} , p_H , p_O and p_{OH} with Eqs. (5.51) to (5.54).
 - d) Set a linear system with Eqs. (5.58), (5.59), (5.61), (5.62), (5.64) and (5.65), and obtain new values of n_{H_2O} , n_{OH} , n_{H_2} , n_{O_2} , n_H and n_O . Go again to step a.

Once the moles of each species are determined, mass fractions can be obtained by using Eq. (5.36). It is important to note that mass fractions are function of ϕ , T and p . Therefore, from chain rule, the derivatives are

$$\frac{dY_i}{dx} = \frac{\partial Y_i}{\partial \phi} \frac{d\phi}{dx} + \frac{\partial Y_i}{\partial T} \frac{dT}{dx} + \frac{\partial Y_i}{\partial p} \frac{dp}{dx} \quad (5.66)$$

Where the partial derivatives can be calculated numerically

$$\frac{\partial Y_i}{\partial \phi} = \frac{Y_i(\phi + \Delta\phi, T, p) - Y_i(\phi - \Delta\phi, T, p)}{2\Delta\phi} \quad (5.67)$$

$$\frac{\partial Y_i}{\partial T} = \frac{Y_i(\phi, T + \Delta T, p) - Y_i(\phi, T - \Delta T, p)}{2\Delta T} \quad (5.68)$$

$$\frac{\partial Y_i}{\partial p} = \frac{Y_i(\phi, T, p + \Delta p) - Y_i(\phi, T, p - \Delta p)}{2\Delta p} \quad (5.69)$$

A second order approximation is enough since the variation for all three variables is very soft (see Section 7.4). The increases $\Delta\phi$, ΔT and Δp must be small enough so that changes in the values of derivatives were not appreciable.

5.3.3. Combustion with non-equilibrium dissociation

Here it is introduced the finite rate chemistry to model high-speed engine flowfields. In supersonic combustors, usually chemical equilibrium is not reached due to the high velocity of the flow; thus a better approximation of the combustion phenomenon is to include reaction rates.

Species conservation within the control volume yields

$$(\dot{m}_i)_{x+\Delta x} - (\dot{m}_i)_x = (\dot{m}_i)_{addition} + \dot{\omega}_i MW_i A \Delta x \quad (5.70)$$

The left-hand side of Eq. (5.70) is the net mass flow of species i leaving the control volume. The first term on the right-hand side is a source term that takes into account mass injection. The second term on the right-hand side is a source or sink term caused by chemical reactions within the control volume.

Dividing by $\Delta x \rightarrow 0$ is found

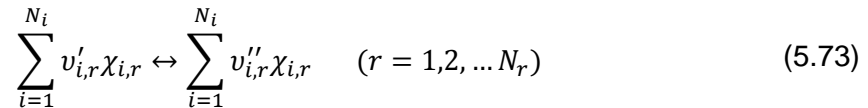
$$\frac{d(\dot{m}_i)}{dx} = \frac{d(\dot{m}_i)_{addition}}{dx} + \dot{\omega}_i MW_i A \quad (5.71)$$

Making use of Eq. (5.36), the differential form of mass fraction is

$$\frac{dY_i}{dx} = \frac{1}{\dot{m}} \frac{d(\dot{m}_i)_{addition}}{dx} + \frac{\dot{\omega}_i MW_i}{\rho u} - \frac{Y_i}{\dot{m}} \frac{d\dot{m}}{dx} \quad (5.72)$$

Notice that, in the current model, the only species added to the control volume is hydrogen (H_2). Computing the molar production (or destruction) rate of each species $\dot{\omega}_i$ requires the assumption of a chemical reaction mechanism. In chemistry, a reaction mechanism is the step by step sequence of elementary reactions by which overall chemical change occurs. As introducing a very detailed chemical reaction mechanism could bring a lot of complexity and be computationally time consuming, the model developed in this study will deal only with reduced reaction mechanisms.

Consider N_r elementary reversible (or irreversible) reactions involving N_i chemical species that can be represented in the general form



The stoichiometric coefficients $v_{i,r}$ (both forward ' and backward '') are integer numbers and χ_i is the chemical symbol for the i th species.

The production rate $\dot{\omega}_i$ of the i th species can be written as a summation of the rate-of-progress variables for all reactions involving the i th species

$$\dot{\omega}_i = \sum_{r=1}^{N_r} (v''_{i,r} - v'_{i,r}) \dot{q}_r \quad (i = 1, 2, \dots, N_i) \quad (5.74)$$

The rate-of-progress variable \dot{q}_r for the r th reaction is given by the difference of the forward and backward rates

$$\dot{q}_r = k_{f,r} \prod_{i=1}^{N_i} [\chi_{i,r}]^{v'_{i,r}} - k_{b,r} \prod_{i=1}^{N_i} [\chi_{i,r}]^{v''_{i,r}} \quad (5.75)$$

Where $[\chi_{i,r}]$ is the molar concentration of the i th species in r th reaction, and $k_{f,r}$ and $k_{b,r}$ are the forward and backward rate constants of the r th reaction.

The forward rate constants are generally assumed to have the following Arrhenius temperature dependence

$$k_{f,r} = A_r T^{\beta_r} \exp\left(\frac{-E_r}{RT}\right) \quad (5.76)$$

Where the pre-exponential factor A_r , the temperature exponent β_r , and the activation energy E_r are tabulated in the literature for a specified chemical reaction mechanism.

The backward rate constants are related to the forward ones through the equilibrium constants based on concentrations by

$$k_{b,r} = \frac{k_{f,r}}{K_{c,r}} \quad (5.77)$$

$$K_{c,r} = K_{p,r} \left(\frac{p_{atm}}{RT}\right)^{\sum_i (v''_{i,r} - v'_{i,r})} \quad (5.78)$$

$$K_{p,r} = \exp\left(\frac{-\Delta G}{RT}\right) = \exp\left(\frac{\Delta s_i^0}{R} - \frac{\Delta h_i^0}{RT}\right) \quad (5.79)$$

The Δ refers to the change that occurs in passing completely from reactants to products in the r th reaction. To write Eq. (5.79) pressures must be expressed in atmosphere.

In some reactions a “third body” M is required for the reaction to proceed; this is often the case in dissociation or recombination reactions. A general case could be two species A and B reacting to yield one single product species AB .

Nevertheless, this reaction requires an intermediate reaction with a third body M which stabilize the excited product AB^* by collision. The third body M is an inert molecule that can remove the excess energy from AB^* and eventually dissipate it as heat.



To emphasize the need for a third body, common practice is to write the overall reaction as



When a third body is needed, the concentration of the effective third body must appear in the expression for the rate-of-progress variable. Accordingly, the rate-of-progress variable is different from Eq. (5.75) by the first factor in the following equation which is called net effect of third bodies

$$\dot{q}_r = \left(\sum_{i=1}^{N_i} \gamma_{i,r} [\chi_{i,r}] \right) \left(k_{f,r} \prod_{i=1}^{N_i} [\chi_{i,r}]^{v'_{i,r}} - k_{b,r} \prod_{i=1}^{N_i} [\chi_{i,r}]^{v''_{i,r}} \right) \tag{5.82}$$

If all species in the mixture contribute equally as third bodies, then $\gamma_{i,r} = 1$ for all i , and the first factor is the total concentration of the mixture

$$[M] = \sum_{i=1}^{N_i} [\chi_{i,r}] \tag{5.83}$$

However, it is often the case that some species act more efficiently as third bodies than do others, and $\gamma_{i,r}$ differs from 1 for that ones.

5.4. Complete equation set

Combining Eqs. (5.2), (5.12), (5.21) and (5.31) gives the differential equation for velocity in the duct

$$\begin{aligned} \frac{du}{dx} = \frac{1}{\alpha} \left(\frac{1}{\dot{m}} \frac{d\dot{m}}{dx} - \frac{1}{A} \frac{dA}{dx} - \frac{1}{\overline{MW}} \frac{d\overline{MW}}{dx} \right. \\ \left. + \frac{1}{c_p T} \left[- \sum_i \left(h_i \frac{dY_i}{dx} \right) - \frac{1}{\dot{m}} \frac{d\dot{m}}{dx} \left(h + \frac{1}{2} u^2 \right) + \frac{1}{\dot{m}} \frac{d\dot{m}}{dx} h_f + \frac{\dot{q} P_w}{\dot{m}} \right] \right. \\ \left. + \frac{1}{p} \left[\frac{1}{2} \rho u^2 c_f \frac{P_w}{A} + \frac{1}{2} \rho u^2 c_{fj} \frac{P_{fj}}{A} + \frac{1}{A} \frac{d\dot{m}}{dx} u (1 - \varepsilon) \right] \right) \end{aligned} \quad (5.84)$$

Where

$$\alpha = -\frac{\rho u}{p} + \frac{1}{u} + \frac{u}{c_p T} \quad (5.85)$$

Next, there is a reminder of the differential equations for density, pressure and temperature

$$\frac{d\rho}{dx} = \rho \left(\frac{1}{\dot{m}} \frac{d\dot{m}}{dx} - \frac{1}{u} \frac{du}{dx} - \frac{1}{A} \frac{dA}{dx} \right) \quad (5.86)$$

$$\frac{dp}{dx} = - \left(\frac{1}{2} \rho u^2 c_f \frac{P_w}{A} + \frac{1}{2} \rho u^2 c_{fj} \frac{P_{fj}}{A} + \rho u \frac{du}{dx} + \frac{1}{A} \frac{d\dot{m}}{dx} u (1 - \varepsilon) \right) \quad (5.87)$$

$$\frac{dT}{dx} = \frac{1}{c_p} \left[- \sum_i \left(h_i \frac{dY_i}{dx} \right) - \frac{1}{\dot{m}} \frac{d\dot{m}}{dx} \left(h + \frac{1}{2} u^2 \right) + \frac{1}{\dot{m}} \frac{d\dot{m}}{dx} h_f - u \frac{du}{dx} + \frac{\dot{q} P_w}{\dot{m}} \right] \quad (5.88)$$

All of these equations plus the differential mass fractions dY_i/dx derived in Section 5.3 represent a set of Ordinary Differential Equations that can be solved using an ODE solver. This solver can be an implicit scheme or a Runge-Kutta method for example.

5.5. Semi-perfect gas flow properties

The flow properties for species i , as well as the mean values of the gaseous mixture, will be computed assuming a semi-perfect gas, or what is the same a thermally perfect gas. This means that heat capacity, and static enthalpy and entropy are only functions of temperature. NASA polynomials will be used

$$\frac{c_p}{R} = a_1 + a_2 T + a_3 T^2 + a_4 T^3 + a_5 T^4 \quad (5.89)$$

$$\frac{h}{RT} = a_1 + a_2 \frac{T}{2} + a_3 \frac{T^2}{3} + a_4 \frac{T^3}{4} + a_5 \frac{T^4}{5} + \frac{a_6}{T} \quad (5.90)$$

$$\frac{s}{R} = a_1 \ln T + a_2 T + a_3 \frac{T^2}{2} + a_4 \frac{T^3}{3} + a_5 \frac{T^4}{4} + a_7 \quad (5.91)$$

Where a_1 , a_2 , a_3 , a_4 , a_5 , a_6 and a_7 are the curvefit constants supplied by NASA thermodynamical coefficients. Remember the definitions of enthalpy and entropy

$$h = \Delta h_f^0 + \int_{T_{ref}}^T c_p dT \quad (5.92)$$

$$s = \int_{T_{ref}}^T \frac{c_p}{T} dT - R_g \ln \left(\frac{p}{p_{ref}} \right) \quad (5.93)$$

Where R_g is the gas constant, and the reference values are 298.15 K and 1 atm.

5.6. Supersonic mixing model

The key to accurate combustor performance simulation is determining the correct release of energy along the duct. In the current model, this is performed by deriving a supersonic mixing model.

Typically, mixing of fuel and air is calculated by solving the Navier-Stokes equations in conjunction with a turbulence model. To keep the computational overheads low, the problem is simplified using the concept of mixing efficiency, which is defined as the ratio of fuel that is available for combustion to the amount that was injected. A relation specifically for mixing efficiency in scramjet combustors is derived using results from literature.

It is assumed that the fuel available for reaction can be determined using a mixing efficiency

$$\dot{m}_{fm} = \eta_m \dot{m}_{0f} \quad (5.94)$$

Where \dot{m}_{fm} is the fuel mass flow rate available for reaction, η_m is the mixing efficiency, and \dot{m}_{0f} is the fuel mass flow rate that passes through the

injectors. The mixing efficiency changes in value from zero at the injector exit until it reaches unity at a defined mixing length L_{mix} , where all the injected fuel is mixed with air and is ready for combustion.

On the one hand, the mixing efficiency can be calculated using

$$\eta_m = a \left(1 - e^{-(k\bar{x})^d} \right) \quad (5.95)$$

With constants derived from numerical and experimental results

$$\begin{aligned} a &= 1.06492 \\ k &= 3.69639 \\ d &= 0.80586 \end{aligned}$$

The normalised distance along the combustor is defined as

$$\bar{x} = \frac{x}{L_{mix}} \quad (5.96)$$

The mixing length can be calculated using

$$\frac{L_{mix}}{d_f} = \frac{K^*}{f(M_c)} \left(\frac{\rho_f u_f}{\rho_a u_a} \right)^{1/2} \quad (5.97)$$

$$f(M_c) = 0.25 + 0.75e^{-3M_c^2} \quad M_c = \frac{u_f - u_a}{a_f + a_a} \quad (5.98)$$

Where d_f is the injector hydraulic diameter, and K^* is a constant that depends on the type of injection system and a variety of other injector-flowfield interaction parameters. For strut-injection configurations $K^* = 390$.

Since the expression of Eq. (5.95) is derived from empirical results, two modifications must be done:

- 1) This formula has a singularity at $x = 0$, so a parabola function is used to adjust the mixing efficiency at values close to $x = 0$. To define this parabola, three conditions are imposed: at $x = 0$ worth 0, and when it joints with the function of Eq. (5.95) the value and the derivative is equal to the value and the derivative of the function of Eq. (5.95).
- 2) At $x = L_{mix}$ the mixing efficiency must be worth 1 by definition; however, this is not fulfilled. Then, this formulation has to be delimited for a maximum value: 1 (assuming that all the fuel injected will be available for reaction at L_{mix}) or less (if it is wanted a fuel remaining never mixed).

On the other hand, the fuel-air mixing friction might be related with this aforementioned formulation. The jet friction coefficient c_{fj} and the hydraulic perimeter of the fuel jet P_{fj} can be computed by

$$c_{fj} = \frac{2}{\rho u \pi d_f} \frac{d\dot{m}_{fm}}{dx} \quad (5.99)$$

$$P_{fj} = \pi d_f \quad (5.100)$$

Then, the fuel jet friction force of Eq. (5.11) is converted to

$$F_{mix} = \frac{u}{A} \frac{d\dot{m}_{fm}}{dx} \quad (5.101)$$

Where $\frac{d\dot{m}_{fm}}{dx}$ is the ratio of fuel mixed or, what is the same, the ratio of fuel available for reaction. So, it can be derived from Eqs. (5.94) and (5.95)

$$\frac{d\dot{m}_{fm}}{dx} = \frac{d\eta_m}{dx} \dot{m}_{0f} \quad (5.102)$$

5.7. Reaction mechanism

In the current study a very simple mechanism has been used. It is called Abridged Jachimowski and it consists of seven species and seven reactions. The species are N_2 , H_2O , OH , H_2 , O_2 , H and O , and the reactions are listed in Table 2. Notice that the first two reactions are third body reactions, where M represents the third body. Thus, each equation requires a third body efficiency for each species. The species H_2 has $\gamma = 2.5$ for both reactions and H_2O has $\gamma = 16.0$ for both reactions. All other species have a third body efficiency of 1.0 for both reactions. The mechanism parameters are listed in Table 3.

R_1	$H + OH + M \leftrightarrow H_2O + M$
R_2	$H + H + M \leftrightarrow H_2 + M$
R_3	$H_2 + O_2 \leftrightarrow OH + OH$
R_4	$H + O_2 \leftrightarrow OH + O$
R_5	$OH + H_2 \leftrightarrow H_2O + H$
R_6	$O + H_2 \leftrightarrow OH + H$
R_7	$OH + OH \leftrightarrow H_2O + O$

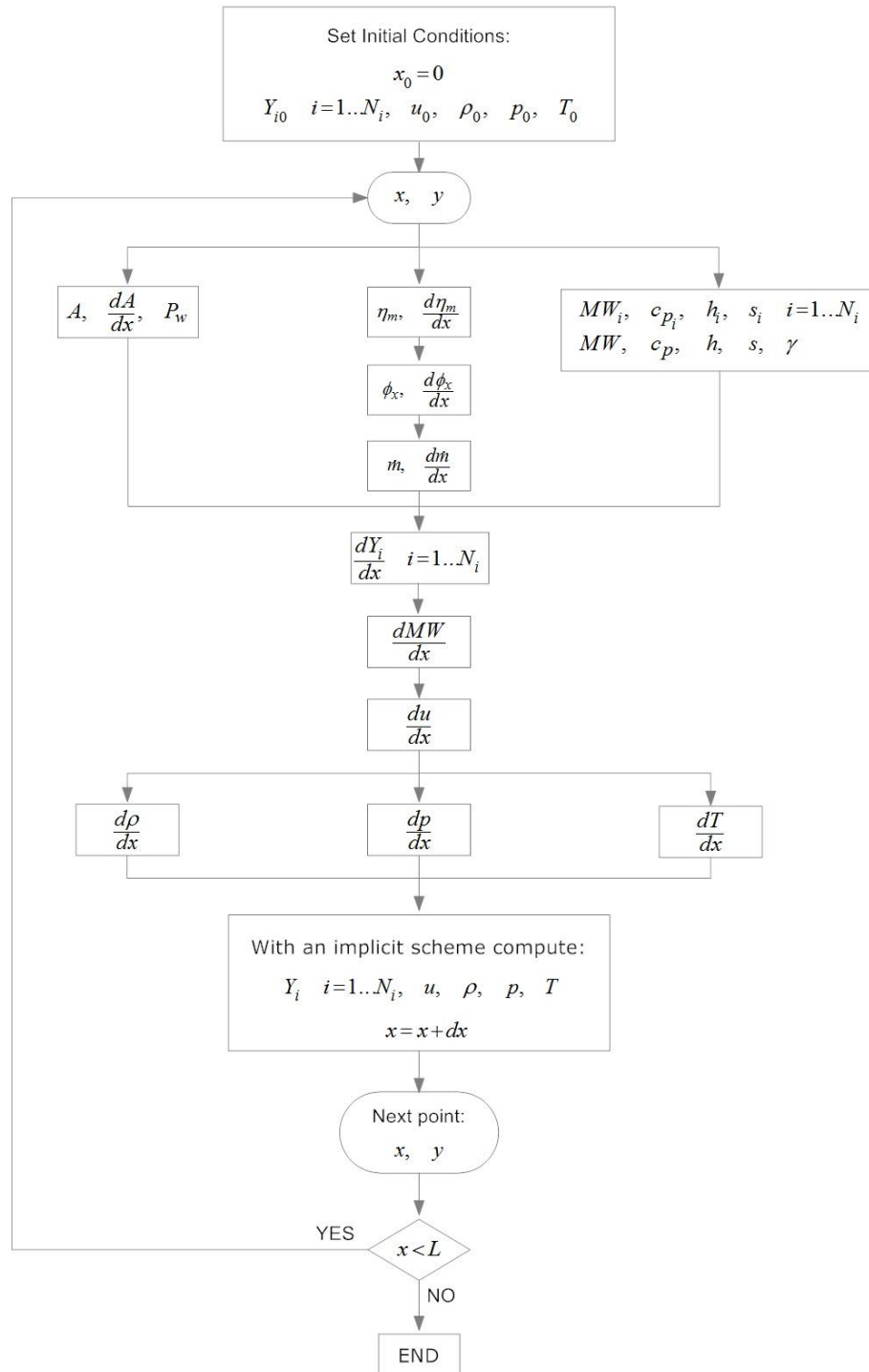
Table 2. Abridged Jachimowski mechanism reactions

	A_r	β_r	E_r
R_1	$2.21 \cdot 10^{22}$	-2.0	0.0
R_2	$7.30 \cdot 10^{17}$	-1.0	0.0
R_3	$1.70 \cdot 10^{13}$	0.0	48000.0
R_4	$1.20 \cdot 10^{17}$	-0.9	16800.0
R_5	$2.20 \cdot 10^{13}$	0.0	5150.0
R_6	$5.06 \cdot 10^{04}$	2.7	6268.0
R_7	$6.30 \cdot 10^{12}$	0.0	1090.0

Table 3. Abridged Jachimowski mechanism parameters. Units are *cal*, *mol*, *cm*³, *s*, *K*.

6. Combustion code

The formulation derived previously, in Chapter 5, has been implemented with MATLAB R2007a, which is a high-level language and interactive environment for numerical computation, visualization, and programming. Next, the algorithm of the code is exposed.



Two different implicit schemes are used for solving the Ordinary Differential Equations. In case of considering combustion without dissociation or with equilibrium dissociation, it is used a sixth-order Gear implicit FDE (Finite Difference Equation); while if the combustion is dealt with finite rate chemistry (non-equilibrium conditions), it is used an implicit trapezoid FDE.

The set of Ordinary Differential Equations form an initial - value ODE system that has the form

$$\begin{aligned}\frac{dy_1}{dx} &= f_1(x, y_1, y_2, \dots, y_m) & y_1(x_0) &= y_1|_0 \\ \frac{dy_2}{dx} &= f_2(x, y_1, y_2, \dots, y_m) & y_2(x_0) &= y_2|_0 \\ &\vdots & &\vdots \\ \frac{dy_m}{dx} &= f_m(x, y_1, y_2, \dots, y_m) & y_m(x_0) &= y_m|_0\end{aligned}\quad (6.1)$$

Where each derivative function f_m is a nonlinear function of the different y 's. Next, the two numerical methods applied to solve this nonlinear first-order ODE system are exposed.

The implicit trapezoid FDE is

$$y_{n+1} = y_n + \frac{\Delta x}{2} (f_n(x_n, y_n) + f_{n+1}(x_{n+1}, y_{n+1})) \quad (6.2)$$

This equation must be solved iteratively for y_{n+1} . It is of third-order locally and second-order globally, and it is unconditionally stable. This is the reason for employing this scheme for combustion with non-equilibrium dissociation, because in this case the final ODE system is stiff and could be difficult or computationally expensive to obtain an accurate stable solution with other methods.

When combustion is dealt with chemical equilibrium throughout the duct, stiffness is not present in the ODE system, so a higher-order scheme is used in order to have more accuracy on the numerical solution. The problem is that then the method is conditionally stable. Gear has devised a series of implicit FDEs that have much larger stability limits than other schemes (such as Adams-Moulton FDEs). The Gear formula of global sixth-order is presented below

$$y_{n+1} = \frac{1}{147} [60 \cdot \Delta x \cdot f_{n+1}(x_{n+1}, y_{n+1}) + (360y_n - 450y_{n-1} + 400y_{n-2} - 225y_{n-3} + 72y_{n-4} - 10y_{n-5})] \quad (6.3)$$

As before, this equation must be solved iteratively for y_{n+1} .

7. Code verification

This chapter presents some checks in order to verify the code of the combustion model presented in Chapter 5. This process is essential in any situation, where a tool has been developed to analyse some phenomenon, to assure that results obtained are correct. There are a lot of verifications that can be done for validating the tool developed; however, here are presented the most relevant ones.

7.1. Isentropic evolution

First of all, it is important to verify that the model describes exactly the isentropic evolution of a flow when the following conditions are imposed:

- Perfect gas
- No mass addition and consequently no mixing friction
- No wall skin friction
- Adiabatic walls

Air is the only gas considered and it has to compress if it is subsonic or expand in case to be supersonic, but keeping constant the total pressure, temperature and enthalpy, while it flows through the combustion chamber, obviously assuming that it is divergent. If the combustor had constant area, the different variables (such as velocity, pressure or temperature) would not suffer any change along the combustor length.

According to the definition of the mass flow rate

$$\dot{m} = \bar{m}(M, \gamma) \frac{p_t A}{\sqrt{R_g T_t}} \quad (7.1)$$

As air is assumed perfect gas, the total pressure and temperature are constants, as well as the mass flow rate, the following expression has to be fulfilled

$$\bar{m}(M_x) A_x = \bar{m}(M_0) A_0 \quad (7.2)$$

Where 0 represents the combustor inlet and x any position along the chamber.

A slightly variation of this check is changing the gas type. If air is assumed a semi-perfect gas, its compression or expansion has to be very similar as the previous one but without keeping constant the total temperature.

7.2. Heat addition

Next consider the effects of heat addition on the air flow in the combustor. For the sake of simplicity, it is assumed a perfect gas and constant flow area. Mass injection, and mixing and wall skin friction are not being considered yet.

The heat added into the combustor through its walls represents the heat released by combustion, and will be treated as Eq. (5.26)⁹ or imposing the heat of combustion for hydrogen (121 MJ/kg). Under the conditions aforementioned the following expressions must be fulfilled

$$\frac{u_x}{u_0} = \frac{1 + \gamma M_0^2}{1 + \gamma M_x^2} \left(\frac{M_x}{M_0} \right)^2 \quad (7.3)$$

$$\frac{\rho_x}{\rho_0} = \frac{1 + \gamma M_x^2}{1 + \gamma M_0^2} \left(\frac{M_0}{M_x} \right)^2 \quad (7.4)$$

$$\frac{p_x}{p_0} = \frac{1 + \gamma M_0^2}{1 + \gamma M_x^2} \quad (7.5)$$

$$\frac{T_x}{T_0} = \left(\frac{1 + \gamma M_0^2}{1 + \gamma M_x^2} \right)^2 \left(\frac{M_x}{M_0} \right)^2 \quad (7.6)$$

$$\frac{p_{tx}}{p_{t0}} = \frac{1 + \gamma M_0^2}{1 + \gamma M_x^2} \left(\frac{1 + \frac{1}{2}(\gamma - 1)M_x^2}{1 + \frac{1}{2}(\gamma - 1)M_0^2} \right)^{\frac{\gamma}{\gamma - 1}} \quad (7.7)$$

$$\frac{T_{tx}}{T_{t0}} = \left(\frac{1 + \gamma M_0^2}{1 + \gamma M_x^2} \right)^2 \frac{1 + \frac{1}{2}(\gamma - 1)M_x^2}{1 + \frac{1}{2}(\gamma - 1)M_0^2} \left(\frac{M_x}{M_0} \right)^2 \quad (7.8)$$

Where 0 represents the combustor inlet and x any position along the chamber.

Furthermore, it is interesting to take notice of flow evolution when heat is added. Adding heat always increases the static and total temperature, and lowers

⁹ Notice that the friction coefficient only appears in this expression to model heat transfer; however, in all other equations must be null.

the total pressure. In terms of static pressure and velocity, the evolution depends on the flow regime. If $M < 1$ the pressure decreases and velocity increases, and if $M > 1$ the pressure raises and velocity decreases. The behaviour of Mach number is the same as the linear velocity, adding heat always drives M toward 1.

7.3. Combustion without dissociation

Next step is to introduce combustion. Firstly, it will be assumed combustion without dissociation. From now on air is considered a semi-perfect gas. For simplicity it is assumed constant flow area, no friction losses and no heat transfer. Under these conditions, the flow properties performance must be that explained in Section 7.2.

This case is quite simple, the only change with respect to the previous case analysed is the mass addition, which is the fuel that will react with air. The fuel is injected at $x = 0$, but as it takes a specific time to mix with the freestream air and consequently to be available for reaction, in practice, it represents that is injected along x a fuel fraction available for reaction.

Therefore, some verifications concerning mass addition can be done. On one hand, the mass flow rate calculated from mass addition must be equal to the mass flow rate calculated from continuity equation; that is

$$\dot{m}_a + \dot{m}_{fm} = \rho u A \quad (7.9)$$

On the other hand, the first principle of thermodynamics has to be fulfilled. Assuming adiabatic walls and no work done to the control volume, as well as considering the hypothesis made during the development of equations of Section 5.1, the subsequent expression has to be meet

$$\dot{m} h_t + \dot{m}_f h_f = c t \quad (7.10)$$

Finally, mass fractions of species products (H_2O , O_2 and N_2) will change according to fuel injected. However, the sum of these mass fractions must always be equal to 1

$$\sum_{i=1}^{N_i} Y_i = 1 \quad (7.11)$$

All three equations are valid at each axial coordinate x of the combustor.

7.4. Combustion with equilibrium dissociation

In order to validate the equilibrium dissociation, it is necessary to validate first the part of the code responsible to calculate the chemical equilibrium. The species considered in the chemical equilibrium for air – hydrogen combustion are H_2O , OH , H_2 , O_2 , H and O (N_2 is also present but it is not dissociated). Figures below illustrate this validation.

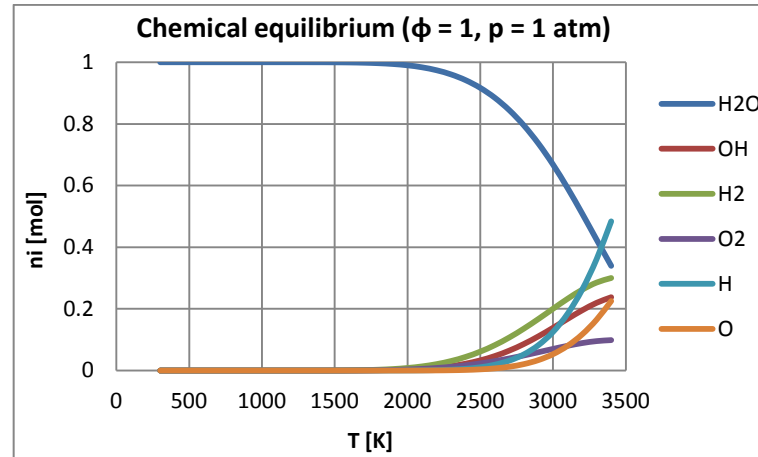


Figure 17. Chemical equilibrium in function of T , for $\phi = 1$ and $p = 1$ atm

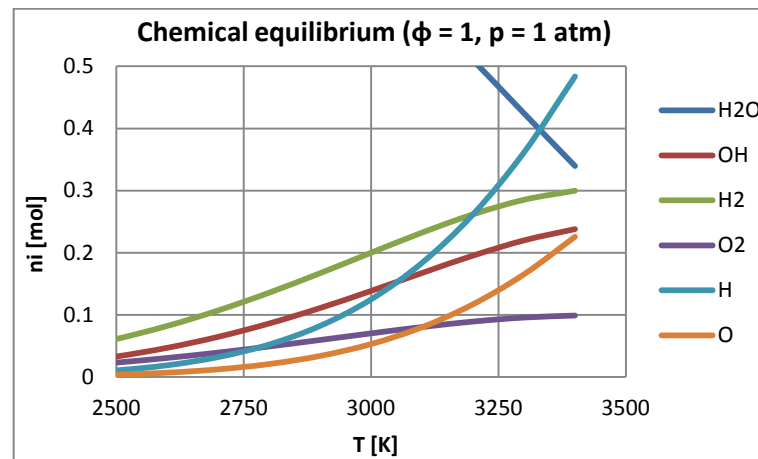


Figure 18. Zoom in of Figure 17

Notice that above 2500K dissociation starts to be present. As temperature rises, the moles of H_2O decrease and increase in the other species due to dissociation.

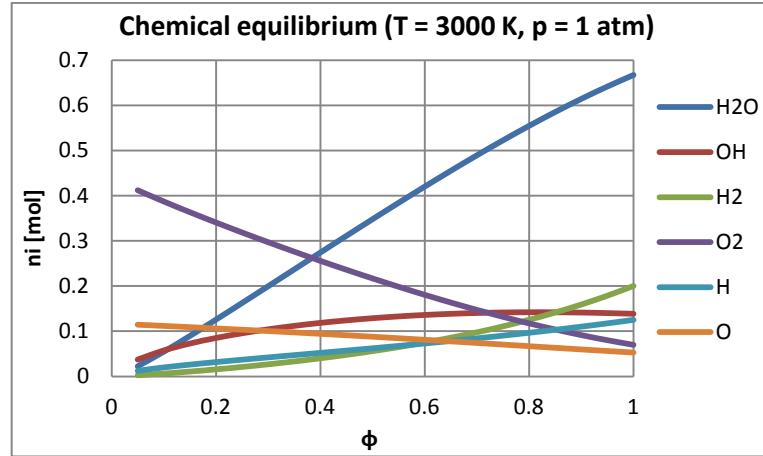


Figure 19. Chemical equilibrium in function of ϕ , for $T = 3000\text{ K}$ and $p = 1\text{ atm}$

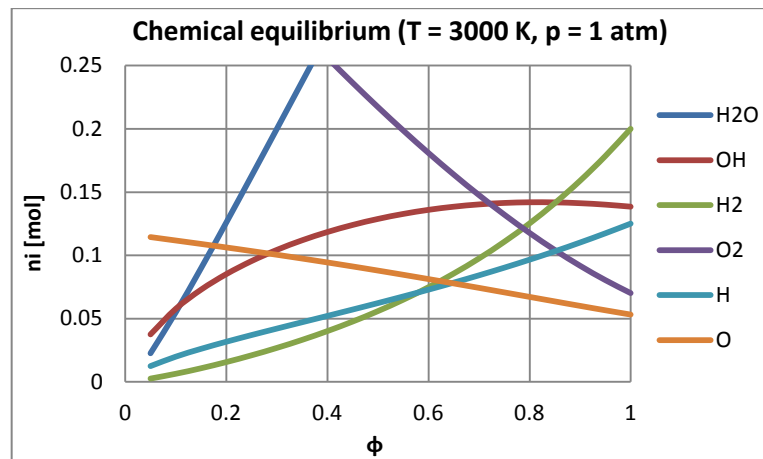


Figure 20. Zoom in of Figure 19

For $\phi = 0$ there is not fuel (H_2), so there is not combustion. As ϕ increases, there are more moles of H_2 that react with O_2 and, consequently, the moles of H_2O , H_2 and H increase while the moles of O_2 and O decrease.

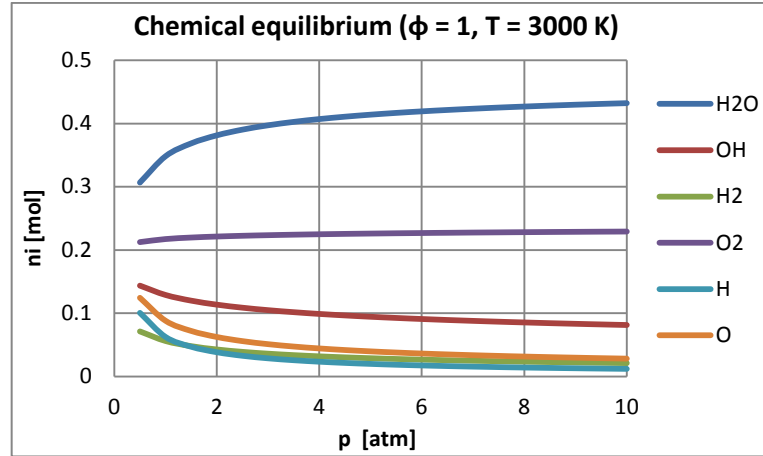


Figure 21. Chemical equilibrium in function of p , for $\phi = 1$ and $T = 3000\text{ K}$

Unlike the dependence of ϕ and T on the chemical equilibrium, the dependence of p is negligible, as it was expected.

Eventually, after observing that results presented above are coherent, the temperature rise in combustion of hydrogen with air is well compared with the predicted in [13].

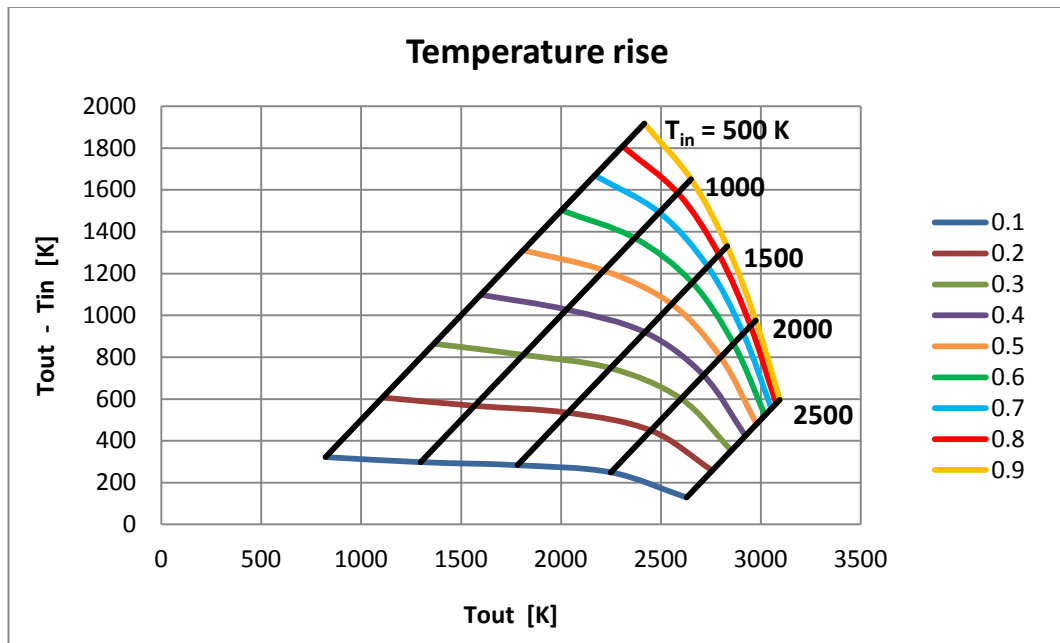


Figure 22. Temperature rise in combustion of H_2 with air, as a function of equivalence ratio, and initial and final temperature, for pressure of 1 atm and no flow

Now, the entire code with equilibrium dissociation can be verified. Assuming the same conditions and characteristics of the case analysed in Section 7.3, here the temperature and the pressure reached at the final combustor length must be lower since dissociation absorbs heat.

Furthermore, Eqs. (7.9), (7.10) and (7.11) should be fulfilled. The last check is through the specific impulse

$$I_{sp} = \frac{F_{net}}{\dot{m}_{of}g} = \frac{\dot{m}_{out}u_{out} - \dot{m}_{in}u_{in} + A_{out}(p_{out} - p_{in})}{\dot{m}_{of}g} \quad (7.12)$$

The value obtained with dissociation must be lower than the value without dissociation. The reason is that the chemical energy of hydrogen – oxygen mixture is not all converted to thermal energy due to heat absorbed by dissociation, and consequently, to kinetic energy.

7.5. Combustion with non-equilibrium dissociation

The last step is to introduce the combustion with non-equilibrium dissociation. Apart from checking Eqs. (7.9), (7.10) and (7.11), the specific impulse of Eq. (7.12) has to be lower than the obtained with the equilibrium solution, then

$$I_{sp}|_{no\ diss.} < I_{sp}|_{eq.\ diss.} < I_{sp}|_{non-eq.\ diss.} \quad (7.13)$$

The specific impulse obtained with non-equilibrium dissociation combustion could be very small or even negative due to the high influence the ignition delay time prediction has on the flowfield performance. In order to avoid this, the gross thrust instead of the net thrust can be compared. Gross thrust should be higher for the equilibrium case and maximum for the solution without dissociation.

The gross thrust is obtained from the complete expression for thrust but removing the term of flight speed

$$F_{gross} = \dot{m}_{out}u_{out} + A(p_{out} - p_{in}) \quad (7.14)$$

8. Results

This chapter analyses the results obtained with the quasi-one-dimensional combustion model developed in the current study. In some cases experimental data is used for comparison. The influence of some critical parameters, such as dissociation, fuel mixing, and combustor chamber design or entrance properties, on the combustor performance are analysed as well. The results presented below accounts for chemical equilibrium and non-equilibrium.

8.1. Chemical equilibrium without dissociation

First of all, the results obtained from the quasi-one-dimensional model assuming chemical equilibrium are compared to experimental data. Two different experiments are used. Then, the influence of the mixing model on the flow performance is studied. For the sake of simplicity, the composition of the flowfield is set to be the major species (H_2O , O_2 and N_2) of reaction products.

8.1.1. HyShot II Flight Tests

Flight tests of HyShot II program [22] are used for validation of the model developed. The HyShot II combustor is a 300-mm-long, 9.8 x 75 mm duct followed by a 147-mm-long, 12° divergence of the duct ceiling (Figure 23). Fuel injection is achieved via circular injection ports in the floor of the combustor (normal injection), 58 mm from the entrance. Two flight conditions are simulated; both are at an altitude of 33 km and at a Mach number of approximately 7.7.

The first flight-test experiment is obtained with no fuel injection and the second one with fuel injection with an overall equivalence ratio of 0.3. For the first experiment the hypersonic inlet supply the combustor with supersonic air at a Mach number of 2, a temperature of 1571 K, and a pressure of 65.90 kPa. In the second experiment the combustor inlet is supplied with supersonic air at a Mach number of 2, a temperature of 1528 K, and a pressure of 73.76 kPa. To achieve the following results, a mixing length of $L_{mix} = 0.9\text{ m}$ is required.

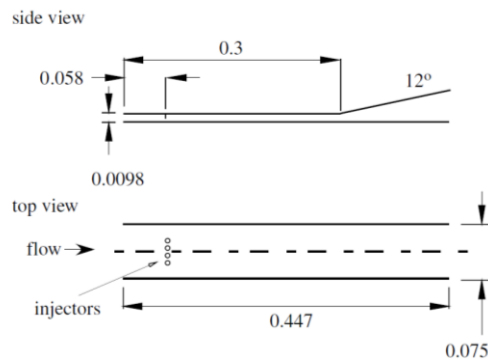


Figure 23. Schematic diagram of the experimental HyShot II combustion duct [22]. Units are in meters.

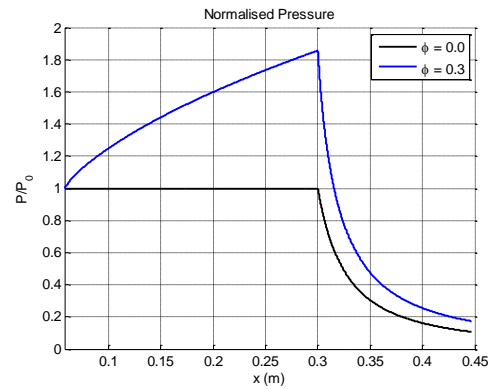


Figure 24. Pressure distribution in the HyShot II combustor (P_0 is the pressure at combustor entrance).

The fuel-off experimental results indicate that the model is correctly modelling gas dynamics. The fuel-on experimental results show how the model adequately resolves the mean pressure rise due to combustion (see Figure 6 of reference [15]). The quasi-one-dimensional model does not capture two phenomena. On the one hand, the pressure fluctuations along the duct due to weak shocks generated by fuel injector, and on the other one, the large pressure rise at the downstream end due to an exhaust shock that compresses the flow to atmospheric conditions. However, in both cases fuel-off and fuel-on, the model does reproduce the mean pressure distribution.

Notice that the hypothesis of chemical equilibrium is valid; the model matches well with experimental data. The pressure and temperature at the combustor entrance are great enough to induce rapidly self-ignition of the hydrogen, and moreover the Mach number is relatively low.

8.1.2. Reflected shock tunnel experiment

Another example to evaluate the accuracy of the current quasi-one-dimensional model is the experiment of the University of Queensland, the T4 reflected shock tunnel [23]. The scramjet test simulated here uses a diverging duct with a rectangular cross section in which both the top and bottom plates are set to 1.72° (Figure 25). Hydrogen fuel is injected at sonic conditions using a central strut (parallel injection) to achieve an overall equivalence ratio of 0.38. Supersonic air at Mach 2.47, a static temperature of 1025 K, and a static pressure of 59 kPa are the flow conditions at the entrance of the combustion chamber. The model will reproduce the flowfield from the exit of the strut injector to the exhaust nozzle combustor.

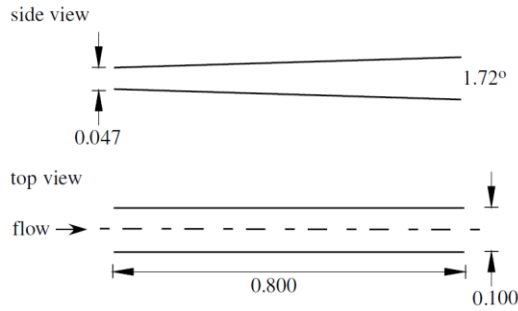


Figure 25. Schematic diagram of the experimental T4 reflected shock tunnel [23]. Units are in meters.

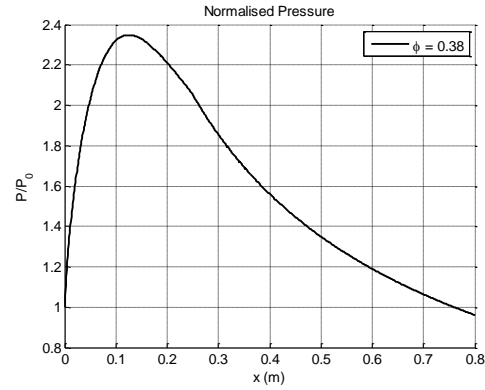


Figure 26. Pressure distribution for T4 experiment (P_0 is the pressure at combustor entrance).

Figure 26 shows the pressure distribution along the duct. If the numerical solution is compared with experimental data (see Figure 2 of reference [15]), it can be seen how the model does not resolve the pressure fluctuations and does not accurately predict the peak pressure. However, it does successfully reproduce the mean pressure rise along the duct. By simulating the mean pressure distribution along the combustor correctly, the quasi-one-dimensional model is capable of calculating the thrust and the specific impulse of a scramjet combustor. As the model is also computationally efficient, it can be directly incorporated into design optimization, performance, and trajectory simulations.

Finally, notice that no mention about the mixing length has been done. That is why the injector used has a strut configuration and it can be calculated and it is not necessary to be estimated. According to the formulation derived in Section 5.6 $L_{mix} = 0.2559 \text{ m}$.

8.1.3. Influence of mixing model

The mixing model is what models the heat release by combustion. Assuming chemical equilibrium through all the duct, each fuel fraction injected and mixed with the freestream air has associated a direct release of heat since it is supposed to react immediately and converted into products. Therefore, it is very important for the quasi-one-dimensional model to have a real modelling of the fuel-air mixing.

In order to analyse the influence of the mixing model on the flowfield performance, the experimental arrangement of Section 8.1.2 is used. Results are illustrated in Figure 27. The black line corresponds to the original mixing model

(see Section 8.1.2), which has been proved to simulate the real heat release by combustion. The coloured blue line is obtained with an invented lineal¹⁰ mixing model. From the big differences between the two cases, it is derived the importance of predicting well the mixing between fuel and air, because this is directly related with heat release, which determines the performance of a combustor.

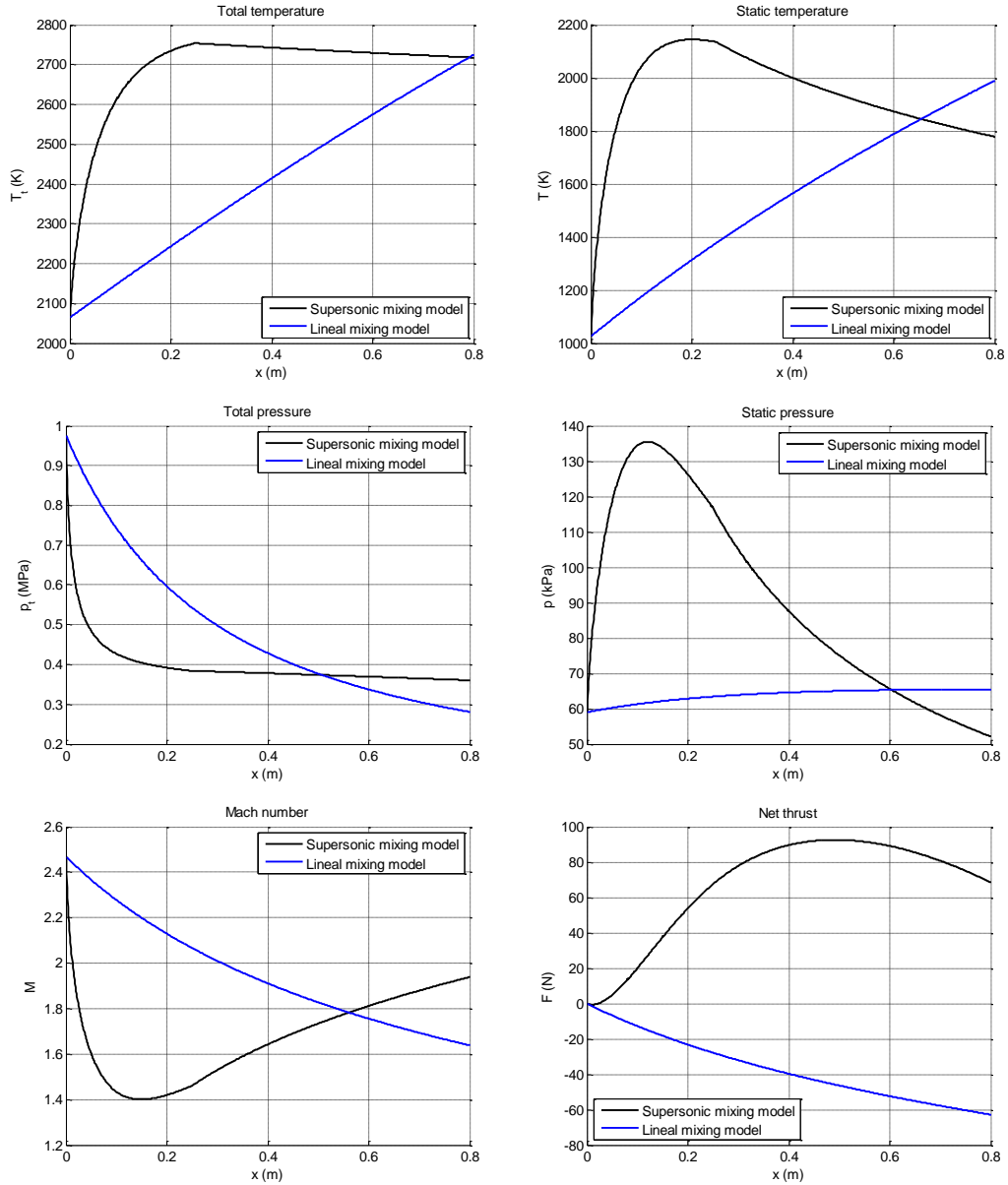


Figure 27. Influence of mixing model on flowfield performance (the experiment of Section 8.1.2 is used, $c_f = 0.002$, $T_w = 500K$)

¹⁰ The mixing efficiency function is a line: $\eta_m = \frac{1}{L}x$, where L is the duct length (in this case 0.8 m) and x the axial position of the duct.

The supersonic mixing model used in the current study is obtained from the literature, and in Sections 8.1.1 and 8.1.2 it has been proved its validity. However, the research done until nowadays on this phenomena is still limited and there is a lack of information or knowledge. For example, for injector configurations different from the strut one, the mixing length has to be estimated. So, what would happen if this estimation is not correct? Next, the influence of the mixing length¹¹ is analysed.

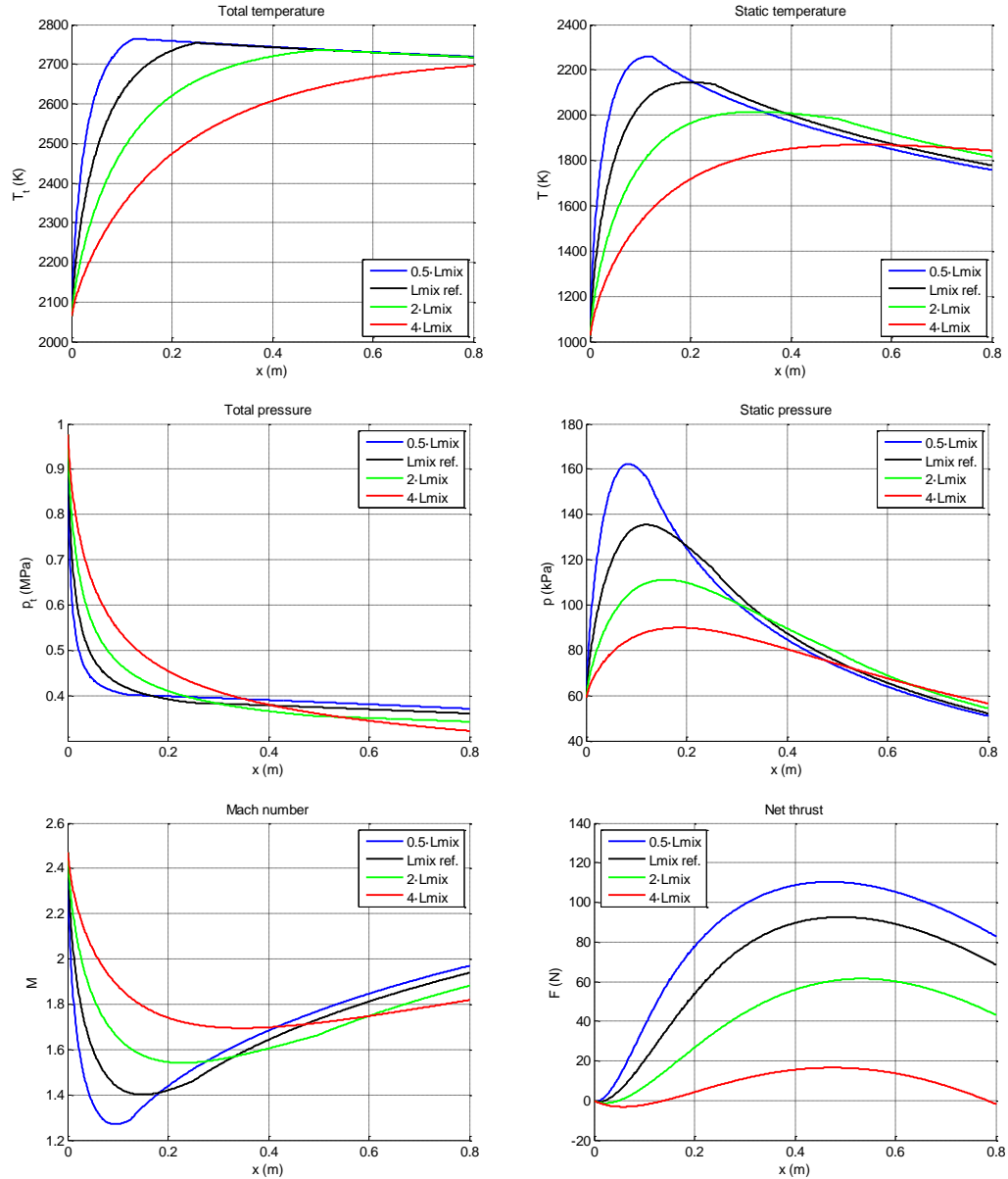


Figure 28. Influence of mixing length on flowfield performance (the experiment of Section 8.1.2 is used, $c_f = 0.002$, $T_w = 500K$).

¹¹ The supersonic mixing model is not changed, the mixing efficiency follows the formulation derived in Section 5.6, what only changes is the mixing length L_{mix} used in this formulation.

The black line corresponds to the reference mixing length (20.5% of the total duct length) that has been proved in Section 8.1.2 to give a good prediction of the combustor performance. Considerable total pressure is destroyed in the mixing region, after that it continues to decrease slightly due to friction losses. The total temperature increases in this region as a result of combustion, and its following small drop is due to the heat transferred to the walls. Close to the entrance, injection and mixing are predominant, so the effects of heat release by combustion prevail in front of expansion effects, and then the Mach number drops significantly while the static pressure and temperature rise. On the other hand, approaching the mixing length the effects of heat release are less severe and the expansion starts to be observed.

The blue line represents a very rapid mixing (L_{mix} is at approximately 10% of the total duct length), so very close to the injection all the fuel is available for reaction. This rapid mixing (and consequently releasing of heat) implies that increases or drops of total and static properties are more accentuated. Nevertheless, the expansion of the flow is very similar to previous case (reference L_{mix}) but it gives a thrust increase of 21%.

The green line corresponds to a L_{mix} of about 64% of the total longitude; this entails that fuel injected spends more time to mix with the freestream air with the consequence that heat release is smoother, and also the variations of flow properties. The thrust loss with respect to the reference case ($L_{mix} = 0.2559 m$) is of 38%.

Eventually, the red line corresponds to a L_{mix} higher than the duct length; this represents a case of an incomplete combustion with the consequence of a lower temperature reached. The peak pressure is also very low compared to other cases and the exit Mach number somewhat lower too. All of this justifies the great thrust loss, 107% with respect to the reference case meaning that the combustion chamber does not generate net thrust.

8.2. Effects of dissociation

After analysing the flow properties without dissociation, it is interesting to observe which would be the performance of the flowfield along the combustor assuming dissociation. Both equilibrium and non-equilibrium conditions will be considered.

8.2.1. Anderson & Gooderum experiment

Here it is used the experiment of Anderson and Gooderum [17] shown in Figure 29 to compare the results between the three types of combustion exposed in Section 5.3. The apparatus consists of a constant-area rectangular duct of height 3.81 cm and width 17 cm followed by a diverging region. Hydrogen is injected normally to the flowfield at 24 cm from the expansion section of the combustor, which has a total length of 71.9 cm and an exit height of 7.62 cm. The global equivalence ratio is 0.619. For the mixing model L_{mix} of 0.6 m is assumed. The incoming flowfield has a Mach number of 3.2, a temperature of 1031 K, and a pressure of 75777 Pa.

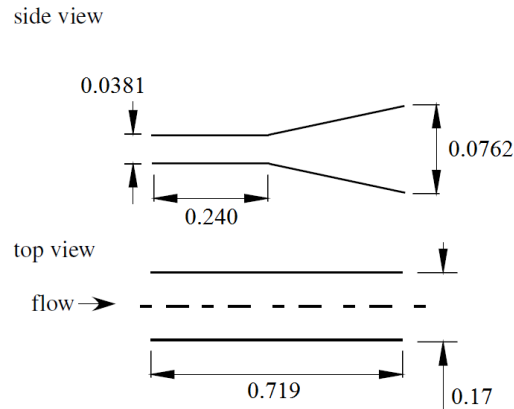


Figure 29. Schematic diagram of Anderson & Gooderum's experimental combustor [17].
Units are in meters.

The combustor performance for the three types of combustion (no dissociation, equilibrium dissociation and non-equilibrium dissociation) is compared in Figure 30 and Figure 31.

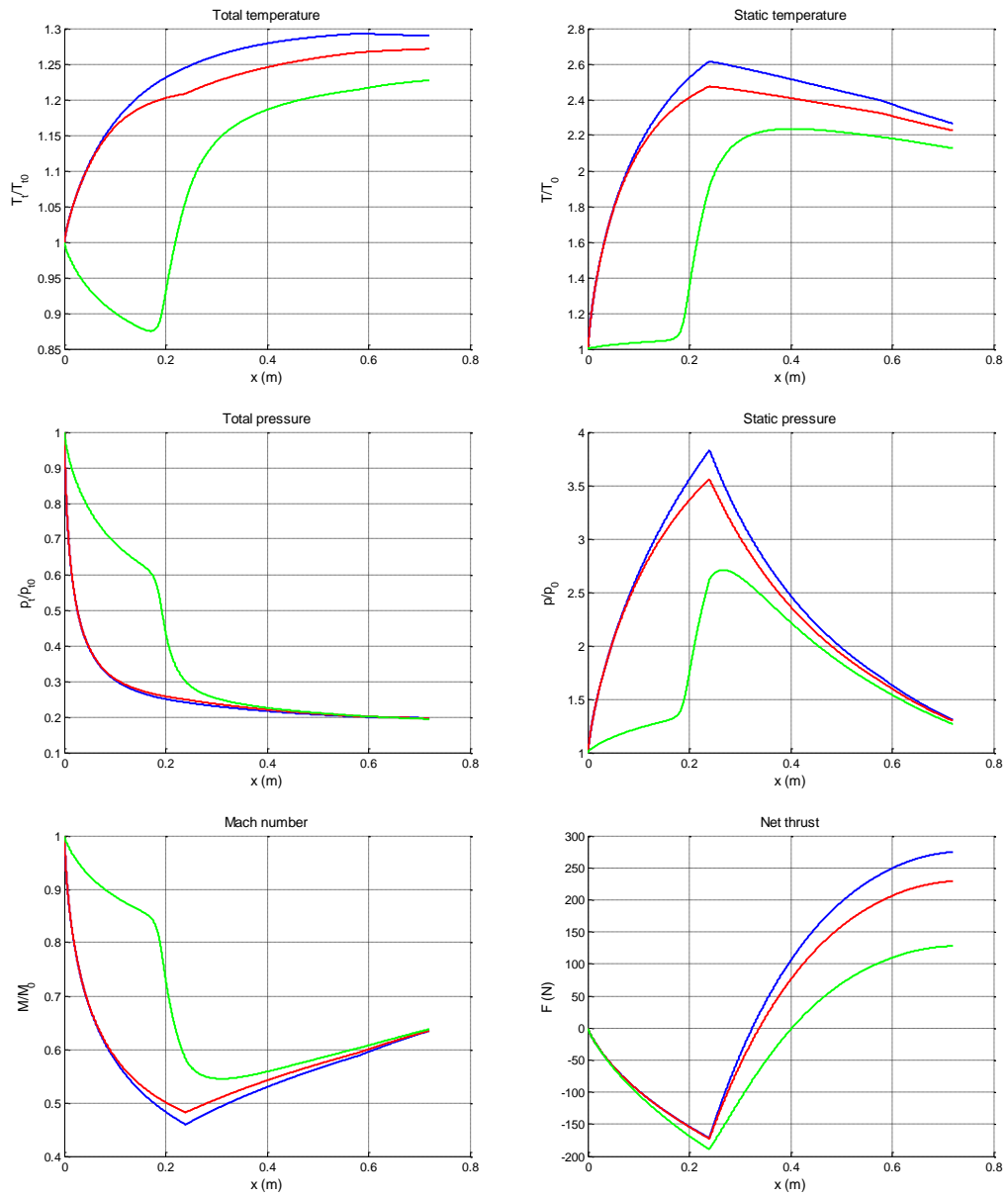


Figure 30. Flowfield performance for Anderson & Gooderum's experiment ($c_f = 0.002$, $T_w = 500K$). All variables except thrust are dimensionalised by its initial values. Legend: blue = no dissociation, red = equilibrium dissociation, green = non-equilibrium dissociation.

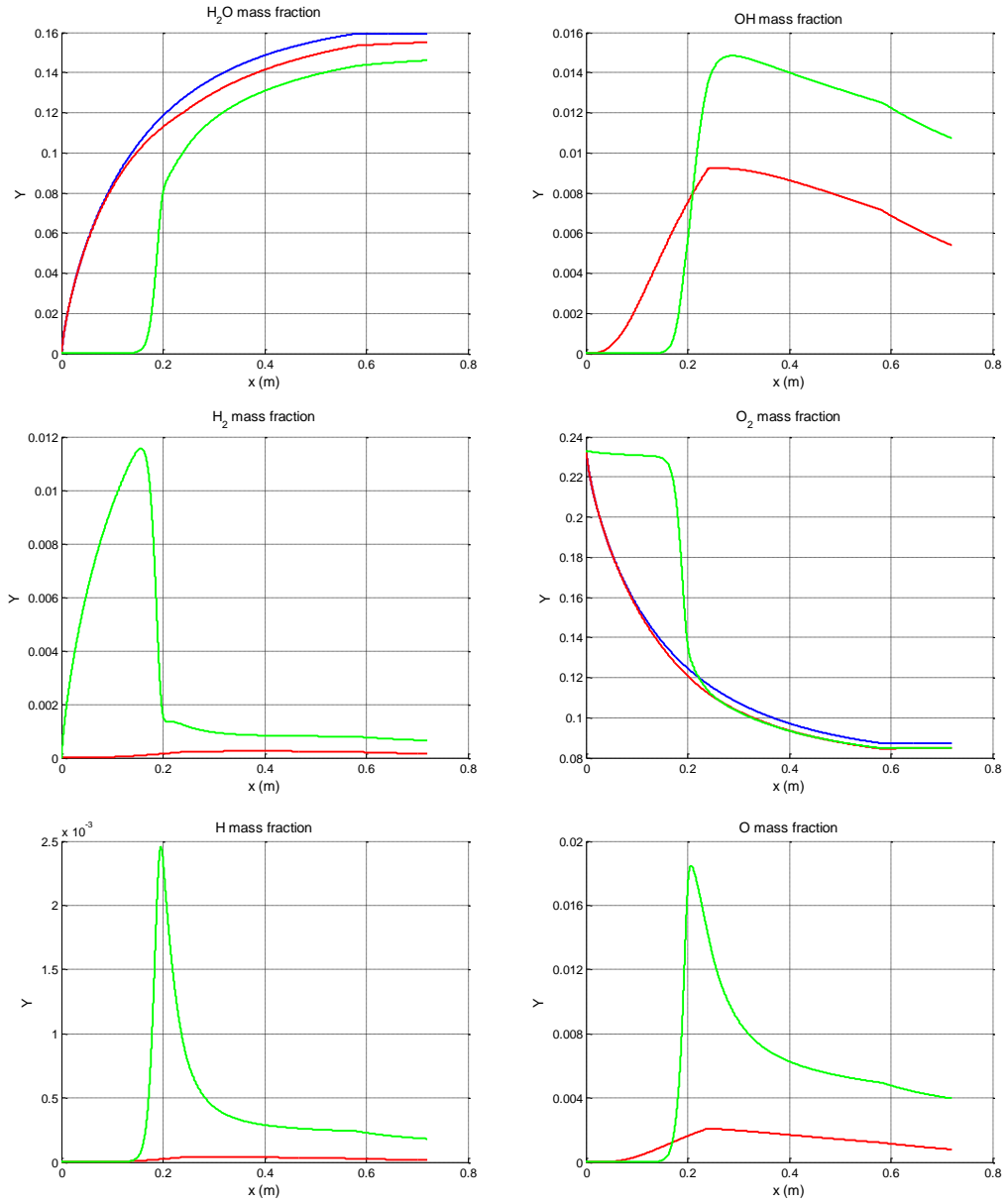


Figure 31. Species mass fractions for Anderson & Gooderum's experiment ($c_f = 0.002$, $T_w = 500K$). N_2 is not shown since it is not dissociated and it acts as an inert gas. Legend: blue = no dissociation, red = equilibrium dissociation, green = non-equilibrium dissociation.

First of all, observe how the temperature reached by the equilibrium dissociation solution (red line) is inferior with respect to the case without dissociation (blue line). The reason is the dissociation of the water to other species such as hydroxyl. Moreover, the pressure reached is also slightly lower, and the Mach number decreases a little less. The relevant consequence of dissociation is a thrust loss. The net thrust generated by this combustor assuming chemical equilibrium is 16.5% lower than the no dissociation case.

After that, pay attention to the non-equilibrium dissociation solution (green line). What is most interesting to highlight is that finite rate chemistry allows for an accurate prediction of fuel ignition. The peak temperature and pressure are even more inferior; with the consequence of a thrust loss of about 44% with respect to the equilibrium dissociation value. The peak pressure predicted is at $x = 0.27 \text{ m}$ location (3 cm past the beginning of the expansion region). Compared to an equilibrium solution, where the peak pressure would be just prior to the expansion region, in the finite rate solution detonation occurs in the expansion zone due this ignition delay; so expansion effects counteract heat release effects and consequently the maximum temperature and pressure achieved will be inferior. Now, observe species mass fractions. Until the ignition does not occur, oxygen is kept constant, hydrogen rises as fuel is being injected and mixed with the freestream air, and water and the rest of species mass fractions are zero. At the ignition moment O_2 and H_2 decline drastically to form basically H_2O and in much lesser extent OH , O and H .

From this example it is derived the importance of predicting well fuel ignition since affects considerably the combustor performance. Moreover, for these combustor inlet conditions, equilibrium hypothesis is not valid. Computing the characteristic times in a certain position of the duct demonstrates this.

The fluid dynamic time can be calculate as

$$\Delta t_d = \frac{\Delta L}{u} = \frac{x(a_3) - x(a_1)}{u(a_2)} \quad (8.1)$$

Where $a_1 < a_2 < a_3$ and $\Delta L \rightarrow 0$.

The chemical reaction time can be expressed as

$$\Delta t_r = \frac{\Delta C_{H_2O}}{\dot{\omega}_{H_2O}} = \frac{C_{H_2O}(a_3) - C_{H_2O}(a_1)}{\dot{\omega}_{H_2O}(a_2)} \quad (8.2)$$

Where C_{H_2O} is the molar concentration and $\dot{\omega}_{H_2O}$ the molar production rate.

Computing the ratio of both characteristic times it is possible to know the validity of assuming equilibrium

$$x = 0.25 \text{ m} \rightarrow \frac{\Delta t_r}{\Delta t_d} = 1.5 \quad (8.3)$$

As it was expected, in this example, the chemical reaction time is higher than the fluid dynamic time. This value justifies the ignition delay. In order to assume equilibrium this ratio should be $\frac{\Delta t_r}{\Delta t_d} \ll 1$.

Finally, another way to quantify the effects of dissociation is through a combustion efficiency, which can be calculated by means of water production

$$\eta_c = \frac{Y_{H_2O}}{(Y_{H_2O})_{no \text{ diss.}}} \quad (8.4)$$

$(Y_{H_2O})_{no \text{ diss.}}$ corresponds to the value obtained if all of the hydrogen injected had been converted to water. For the equilibrium case the value is 0.973 and it proves the efficiency losses that cause dissociation. For the non-equilibrium case the combustion efficiency is 0.917 and apart from dissociation losses it also includes the losses of ignition delay.

8.2.2. Influence of combustor inlet conditions

Now, a simple duct without area changes is used for analysing the influence of combustor inlet conditions. It will be seen that the flow properties at the entrance of the chamber affect considerably the performance of the flowfield assuming non-equilibrium combustion.

Figure 32 illustrates some properties for different initial conditions detailed in Table 4. The area of the duct is of 1 m^2 and fuel is injected at sonic conditions by means of a strut to get an overall equivalence ratio of 0.6. Notice that in case 1 the solution of non-equilibrium dissociation matches with the solution of equilibrium dissociation very close to the entrance. So, the ignition delay could be negligible and equilibrium hypothesis could be valid. The reason is the low Mach number and the high values of pressure and temperature. The other cases are obtained increasing Mach and decreasing pressure and temperature. Therefore, it is observed that the ignition delay rises and the equilibrium state for the finite rate chemistry is achieved further (except for case 4 in which combustion will never be produced, because there is a minimum pressure below which ignition does not occur).

	Case 1	Case 2	Case 3	Case 4
M	2.75	4	4.5	5.5
p [Pa]	299160	43482	22678	7588
T [K]	1878	1105	894	600

Table 4. Flow properties at combustor entrance to get graphs of Figure 32

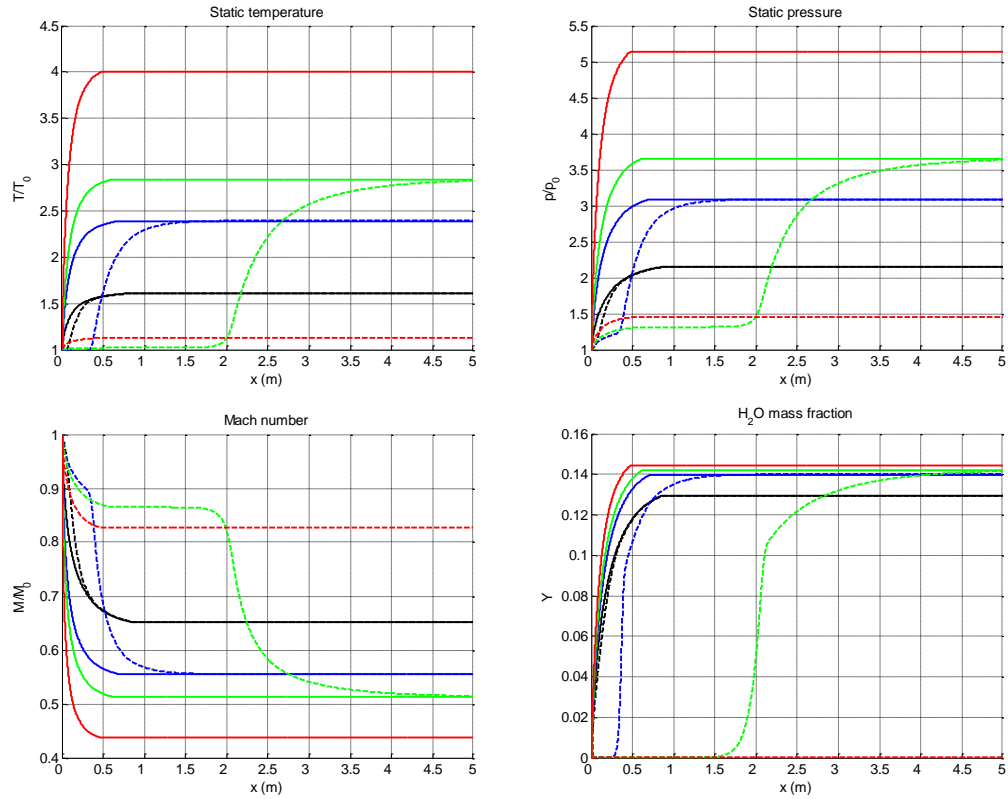


Figure 32. Flowfield performance in an area constant duct for different initial conditions ($c_f = 0$, adiabatic walls). Legend: black = case 1, blue = case 2, green = case 3, red = case 4; continuous line = equilibrium & dashed line = non-equilibrium.

Notice also that a higher combustor inlet temperature entails a lower temperature increase as can be observed in Figure 22. This fact has consequences on the water mass fraction created and other flow properties.

These results show the importance of combustor inlet conditions. A minimum combustor inlet pressure is required to achieve complete combustion within a given length. Alternatively, the combustor length required increases exponentially with the combustor inlet Mach number for fixed total conditions (observe Figure 33). These results also indicate the importance of accounting for continued combustion in nozzles.

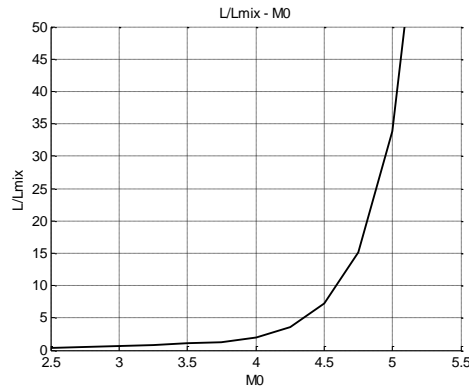


Figure 33. Necessary length to achieve equilibrium in function of combustor inlet Mach

8.2.3. Influence of combustor chamber design

In the previous section the influence of conditions at the combustor entrance has been analysed in a constant area duct. However, the combustor geometry is also determining on the flowfield performance. Next, a diverging duct will be used to analyse the influence of chamber design. For that purpose the length of the duct (2 m), the mixing length (0.8 m), and the initial properties ($u_0 = 2705 \text{ m/s}$, $p_0 = 101325 \text{ Pa}$, $T_0 = 1200 \text{ K}$) are fixed, while the combustor exit area is set to different values (see Table 5). The initial area is of 1 m^2 and the overall equivalence ratio 0.6.

	Case 1	Case 2	Case 3	Case 4	Case 5	Case 6
$\frac{A_f}{A_i}$	1	1.5	2	4	6	2 (isentropic evolution without combustion, $\phi = 0$)

Table 5. Area ratios of the combustor to get graphs of Figure 34

Figure 34 shows some results in function of the ratio A_f/A_i of the combustor duct. As it has been aforementioned, the resulting evolution of the properties is the combination of two phenomena (heat addition by combustion and expansion by divergence) which have contrary effects. These two effects are represented respectively by the black continuous line (no expansion) and the black dashed line (no combustion). The solution without area changes gives the maximum temperature and pressure with respect to the other cases, as it would be expected. As the expansion angle increases the peak temperature and pressure is lower and even if it can disappear for very high expansion angles. The consequence of this is a relevant change on thrust. As high is the

temperature and pressure achieved, higher is the final thrust. In other words, if the expansion is quite accentuated the heat release does not have an appreciable effect, and consequently the combustor thrust will be very low or even if negative.

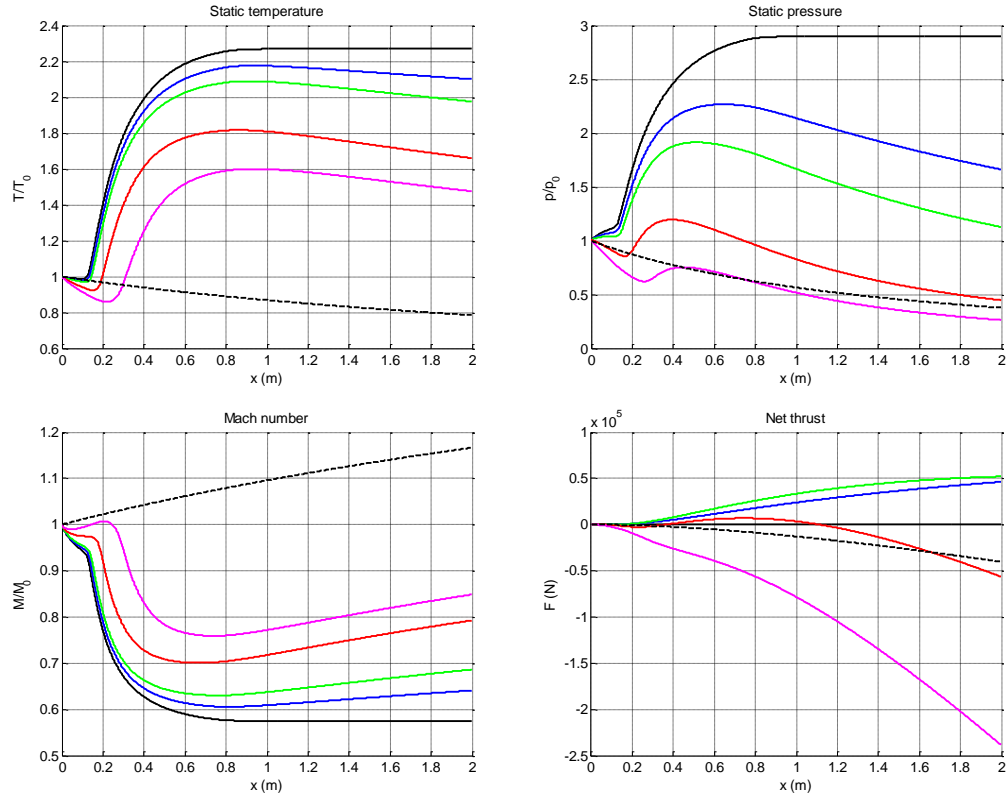


Figure 34. Flowfield performance in a diverging duct for different area ratios ($c_f = 0$, adiabatic walls). Legend: black = Case 1, blue = Case 2, green = Case 3, red = Case 4, pink = Case 5; dashed = Case 6.

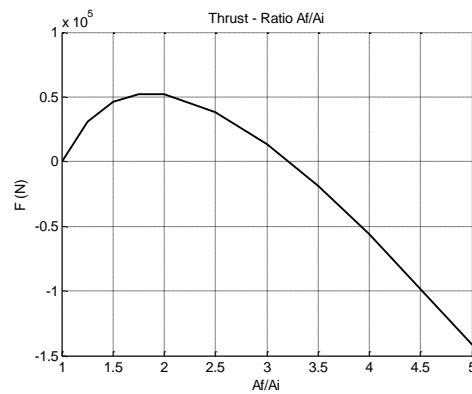


Figure 35. Net thrust generated by the combustion chamber in function of the area ratio

Eventually, comment that the effect of the mixing model or meaning the mixing length is analogous to the effect of the chamber design or the expansion degree. As larger is the mixing length, for fixed initial conditions, higher is the ignition delay time and then, for a fixed combustor length, less longitude for thrust purposes. So the behaviour of the flowfield in function of L_{mix} is similar to that in Figure 34 and Figure 35.

8.3. Effects of friction

The analysis of friction effects is developed with cold flow (no combustion) in order to have a better quantification. Remember that the contribution to friction comes from viscosity and mixing. Furthermore, the friction caused by the viscous boundary-layer and the friction caused by fuel-air mixing are the same order of magnitude.

The cold flow is simulated in a constant area duct (1 m^2). The duct entrance flow conditions are: $u_0 = 1000 \text{ m/s}$, $p_0 = 50 \text{ kPa}$, $T_0 = 288 \text{ K}$. Three different cases are represented in graphs of Figure 36. A first case with no fuel injection or skin friction losses termed “no losses”. A second case with no fuel injection but skin friction losses called “skin friction losses only”. The friction coefficient is set to 0.003. And the third case called “all losses” includes a strut injector, so both skin and mixing friction are present. The hydrogen fuel is injected parallel to the freestream air at the entrance of the duct and the equivalence ratio is 0.6.

Figure 36 shows how total pressure is destroyed by various mechanisms. The skin friction losses are linear along the duct while the mixing losses are (naturally) concentrated towards the injector where the mixing is most intense and are significantly higher. The remaining results in Figure 36 illustrate that static pressure rises while Mach number falls as losses and mass are progressively added to the combustor flow. Thrust is seen to be a little higher with mass injection, but if more fuel was injected, major would be the fuel-air friction and therefore the thrust loss. The friction between fuel and air induces a thrust loss; however, mass addition means more moment and more thrust. Thus, the final result is obtained balancing the two contrary effects. These results are contrasted with those presented in [18].

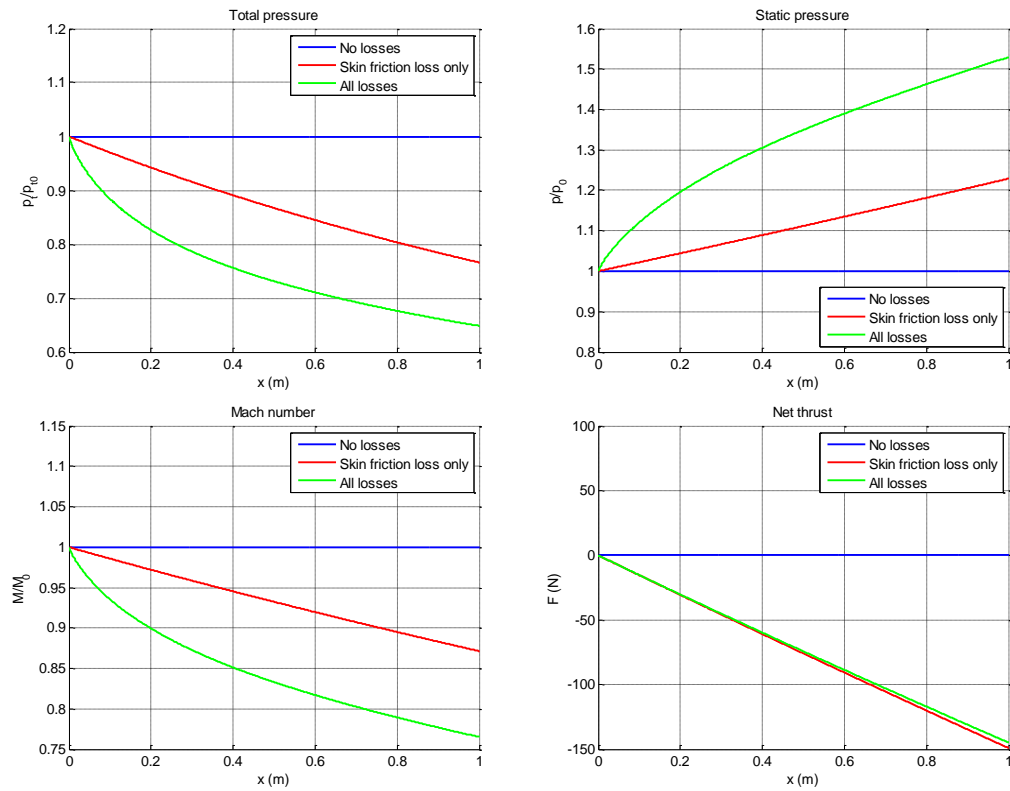


Figure 36. Performance of cold flow along a constant area duct

8.4. Application

Finally, an application example is presented in order to have an overall vision of the scramjet. Figure 37 shows the complete propulsion system, which begins with a series of wedge compression ramps. The flow is turned back to parallel by the front of the engine cowl, with the cowl shock cancelling at the top of the combustor entrance. The area-averaged results from the compression region are then placed into the quasi-one-dimensional combustor model just presented to calculate the combustor flowfield. Gaseous hydrogen is injected normally at the combustor entrance, and it is assumed to be fully mixed by the end of the constant area region. Then, the flow experiences a constant angle expansion for thrusting purposes followed by an internal and external nozzle.

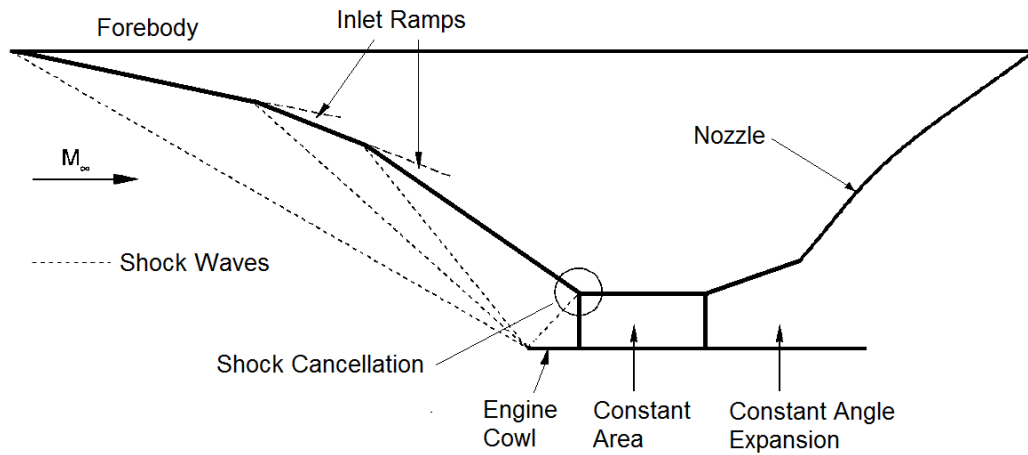


Figure 37. Schematic illustration of a scramjet engine

Assuming freestream Mach number of 12 at an altitude of 36 km, the area-averaged incoming properties into the combustor are a Mach of 4.36, a temperature of 1490K, and a pressure of 57247Pa. In order to achieve these conditions an inlet with four shock waves and a recovery factor of 0.98¹² are assumed. The deflection angles encountered are $\delta_1 = 3.5^\circ$, $\delta_2 = 5.8^\circ$, and $\delta_3 = 17.1^\circ$, being $\delta_4 = -(\delta_1 + \delta_2 + \delta_3)$ fixed in order to turn back the flow parallel to the engine cowl.

The combustor consists of a constant area region of 1 m height and 2 m width followed by a 14° diverging duct of 2.2 m length. The total length of the combustor is 5.8 m. Hydrogen fuel is injected normally at a temperature of 450K and with an overall equivalence ratio of 0.8. It is assumed that at the exit of the constant area region all of the fuel injected is mixed with the freestream air, except a remaining corresponding to a maximum mixing efficiency of 0.99¹³. Finally, a wall skin friction coefficient of 0.003 and a wall temperature of 500K are imposed.

The resulting distributions in flow properties are shown in Figure 38. The temperature slightly increases as a result of mass injection at the beginning of the combustor. At a distance of 0.1 m, fuel ignition is detected with a sharp increase in the temperature and a slope change (although it is difficult to appreciate in this picture). The ignition delay is nearly negligible. The reason is the high inlet temperature. This result is very advantageous from a design and performance viewpoint since it allows a shorter combustion chamber and a higher specific

¹² This value is quite optimistic; a more realistic value could be 0.97. Nevertheless, this difference of 0.01 is an arbitrary margin to account viscosity effects, whose treatment is out of this study. Thus, it is possible to show which should be the geometry of the inlet.

¹³ This maximum mixing efficiency represents inefficiencies and losses as a result of fuel injection. Despite reaching the mixing length a small fraction of fuel injected will never be available for reaction.

impulse. After the ignition, the temperature continues rising as a result of combustion until the end of the constant area region. After that it is observed a slightly decrease due to the expansion effects. Pressure behaves similarly to temperature, being the peak pressure just before the expansion region too. Nevertheless, the distribution of the Mach number is contrary to temperature or pressure. A decrease in Mach number is observed for both mass injection and fuel ignition. A further decrease beyond fuel ignition is observed as a result of combustion and friction effects. From the end of the constant area region the Mach number rises as a result of the expansion.

It is interesting to pay attention on water mass fraction, which obviously increases as a result of combustion but what is not so trivial is that it continues rising along the expansion region. Because of the high combustion temperatures in the constant area region dissociation of water is occurring (see OH mass fraction). As the flow continues in the diverging duct, the temperature begins to fall as a result of the expansion, and then water can begin to form, while OH and other dissociated species decrease again. The heat release from water formation in the diverging section is still enough to heat the flow, so the expansion effects in temperature are not as significative as in pressure.

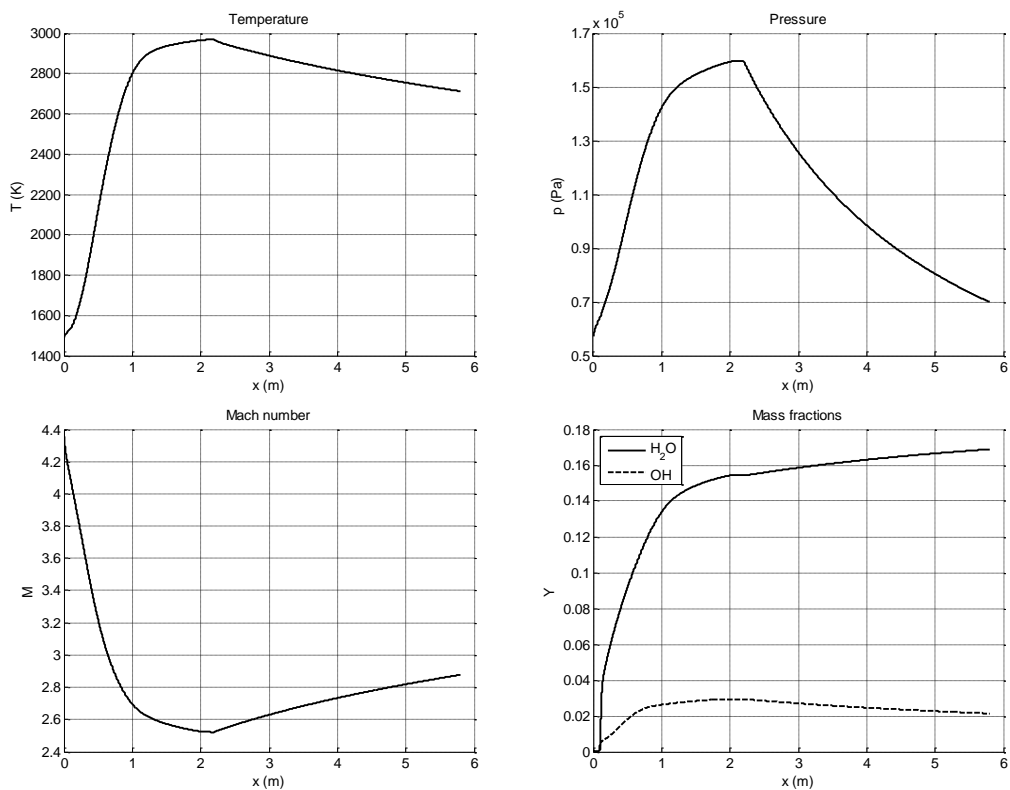


Figure 38. Properties distribution in the combustor of Figure 37

The combustion efficiency defined as the ratio of water mass fraction at the exit of the combustor to the stoichiometric mass fraction value if all the hydrogen had been converted into water is found to be 0.832%. This low value is partially caused by the high combustion temperatures ($\sim 3000\text{K}$) keeping some of the water dissociated. Though the ignition delay is almost negligible, it also has influence on this low value of combustion efficiency.

Eventually, the flow is expanded in a nozzle to generate thrust. Taking advantage of the quasi-one-dimensional combustion model, the flowfield along the nozzle is simulated. But considering the model limitations, this expansion must be performed with an internal nozzle (see Annex D for more details), which is not real. Nevertheless, this analysis will give an estimation of the overall specific impulse, as well as the flow properties at the exit of the scramjet. Thus, the flow is expanded isentropically (adiabatically and without friction effects) until the exit pressure matches the ambient pressure. Three types of flow have been simulated:

- 1) Equilibrium flow throughout the nozzle
- 2) Flow with finite-rate chemistry
- 3) Frozen flow from the combustor exit

The flow enters the nozzle in a highly reactive state, so chemical reactions will occur during its expansion. The first and third cases are two limiting cases. If the expansion is slow enough, chemical equilibrium might be approached. This is an ideal case that gives the maximum specific impulse. The opposite case would be fixing the composition of the flow at the exit of the combustor chamber because the velocity is too high that it could be realistic. However, since the model developed includes finite-rate chemistry, the better (and also realistic) modelling for the nozzle performance is using this finite-rate chemistry. Table 6 summarizes the results obtained at the nozzle exit for the three types of flow aforementioned.

When the ideal nozzle exit velocity has been computed, viscous effects can be accounted for by the use of a kinetic energy efficiency (see Annex D). The actual values that appear in Table 6 have been computed taking $C_v = 0.98^{14}$. Notice the high influence of viscous effects (due to the elevated exhaust velocities), having the actual specific impulse a difference of about 350s with respect to the ideal computed value by the current model. Both thrust and specific impulse are of the overall scramjet.

¹⁴ Realistic value for a well-designed nozzle at high Reynolds number.

	Equilibrium flow	Finite-rate chemistry	Frozen flow
Y_{H_2O}	0.200	0.186	0.169
M	5.74	5.93	6.12
u [m/s]	3990	3936	3904
T [K]	1129	996	900
F_{ideal} [kN]	301.7	253.8	225.2
F_{actual} [kN]	230.6	183.6	155.6
$I_{sp_{ideal}}$ [s]	1519	1278	1134
$I_{sp_{actual}}$ [s]	1161	924	783

Table 6. Exit nozzle flow properties for equilibrium flow, finite-rate chemistry and frozen flow

Charts below illustrate some properties distribution along the combustor and the nozzle.

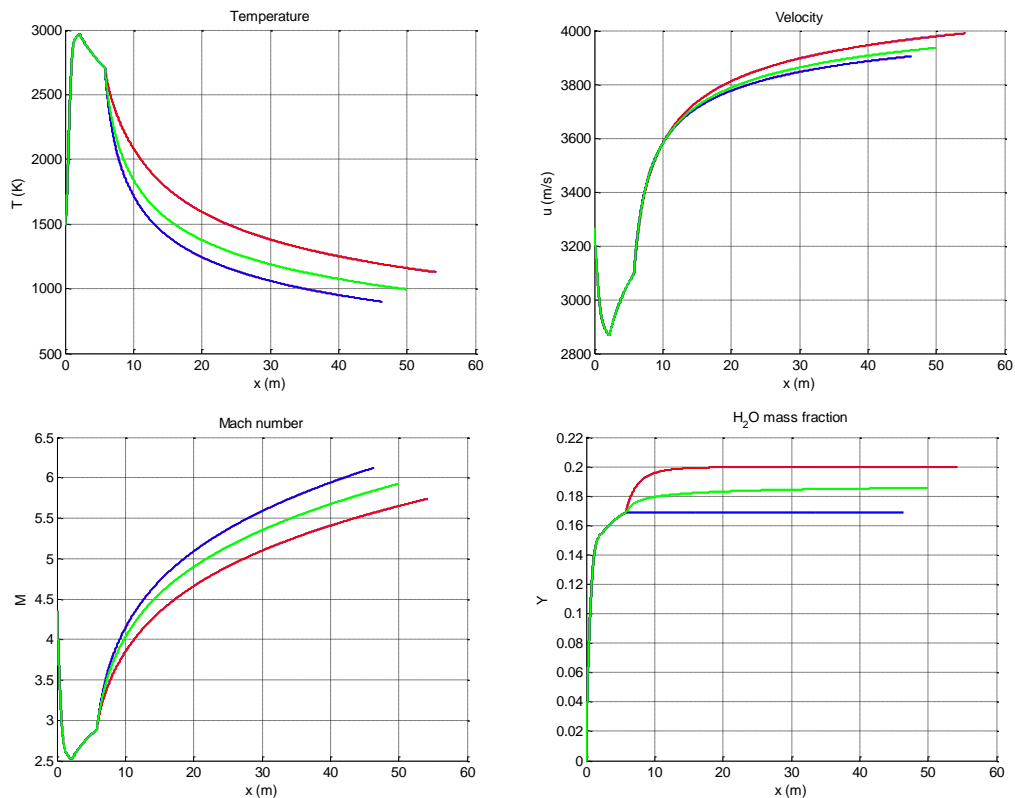


Figure 39. Combustor & nozzle properties distribution. The combustor ends at $x = 5.8$ m and is performed with finite-rate chemistry. The nozzle has been simulated with three types of flow. Legend: blue = frozen flow, green = finite-rate chemistry, red = equilibrium flow.

The flowfield through the combustion chamber is simulated considering the chemical reaction rates (non-equilibrium combustion), while its passage through the nozzle is simulated with three different conditions (equilibrium, finite-rate chemistry and frozen conditions) in order to analyse the final performance of the scramjet. The specific impulse is the primary indicator of engine performance. The lowest value is obtained for the frozen flow solution because its composition is fixed throughout the nozzle (see H_2O mass fraction of Figure 39). On the other hand, the highest value corresponds to the equilibrium case, since the chemical energy invested in dissociation is recovered as thermal energy and then into kinetic energy as recombination occurs in the nozzle. This phenomenon can be observed through the flow properties evolution represented in Figure 39. During the nozzle expansion the temperature decreases with the consequently formation of water (recombination of species). Water formation releases heat at the same time; that is why the temperature does not decrease such as in the frozen flow solution. If the nozzle expansion is performed taking into account the chemical reaction rates, the recombination of species during the expansion is also produced but the formation of water is not as elevated as in the equilibrium case. This case is situated between the other two cases in terms of specific impulse.

The specific impulse computed by the quasi-one-dimensional model with finite-rate chemistry and taking into account all losses and scramjet components efficiencies is of 924s. This value might seem quite low, but it should be noticed that the preceding conditions and geometry are provided as an example and do not imply any optimality. Even so, comparing this value to the well-known results for rocket engines (between 200 and 500 s) it can be derived the feasibility of a scramjet engine for a hypersonic flight, obviously without considering other limitations as those explained in Chapter 3.

Eventually, look at the high nozzle length. Despite this expansion has been performed in an internal nozzle, the weight of a fully-expanded nozzle is prohibitive for the most hypersonic flights. Usually, the nozzles are under-expanded but this implies a loss of specific impulse. Therefore, an agreement has to be reached between the under-expansion losses and the nozzle weight that also acts negatively on the scramjet performance.

9. Conclusions and recommendations

The main work carried out in this study has been the development of a quasi-one-dimensional high-speed engine model in order to simulate the combustion process of a scramjet engine. The scramjet combustion is usually simulated by solving Navier-Stokes equations in conjunction with a turbulent model; however, this is quite computationally expensive. On the contrary, the current developed model is time saving, basically because of its one-dimensional nature. This advantage in conjunction with the accuracy of the results makes this model ideal for design and optimization studies.

As it has already mentioned, the combustion analysis was the main purpose of this project due to its high repercussion on the overall scramjet efficiency, a proved fact in this study. The reason is the dissociation of combustion products. Scramjets are conceived to operate at hypersonic flight Mach numbers, so even though the air inlet does not decelerate the freestream until subsonic regimes, the combustor inlet temperature plus its rise due to combustion leads to so high temperatures within the combustion chamber that the main products are dissociated. This phenomenon absorbs energy and consequently the temperature rise is not as high as it could be without dissociation. This affects the flowfield performance so that the thrust or the specific impulse is lower.

The code has the capacity of simulating the flowfield properties with equilibrium or with finite-rate chemistry. Results show that the inclusion of chemical reaction rates allows for fuel ignition prediction, a determining phenomenon on the combustor performance for the most scramjet operational conditions, where equilibrium hypothesis are not valid. Not only incorporating the timescales for ignition allows for a good prediction of properties distribution, also considering the fuel-air mixing time is crucial to foretell correctly the heat release by combustion. Moreover, keep in mind that this process is one of the limitations of a scramjet and it must be correctly modelled. In this study, a supersonic mixing model derived from the literature has been employed and proved its validity.

Furthermore, the influences of some critical parameters are presented. Apart from quantifying the effects of using one supersonic mixing model or another one, as well as different mixing lengths; the combustion chamber design and its entrance conditions are analysed as well. It could be concluded that as higher are the inlet temperature and pressure and lower the Mach number, inferior will be the ignition delay allowing shorter combustors for a fixed level of water production, but on the other hand a very high inlet temperature (which is

the consequence of a very low Mach number for a fixed flight velocity) implies more dissociation being counterproductive for the efficiency and thrust. Therefore, the two effects must be balanced in order to optimize the performance. These results also indicate the importance of considering reactions in the subsequent nozzle expansion. A rapid mixing (short mixing length) also implies inferior ignition times affecting positively the overall performance. A diverging combustor is designed for thrust purposes; however, accentuated expansion angles are counterproductive since the maximum pressure achieved is lesser. It should be noted that all these parameters are very interrelated, so the combustor performance depends on a combination of geometry, inlet conditions, and fuel mixing, making the scramjet combustion a so complex phenomenon, obviously without talking about its physical complexity and limitations.

Eventually, the air inlet and the nozzle are briefly analysed in order to have an overall vision of the scramjet engine. For the air inlet, it is assumed a kinetic energy efficiency and then the properties at the combustor entrance are computed. The nozzle expansion has been simulated with equilibrium flow, frozen flow, and with finite-rate chemistry, thus the final specific impulse can be compared. The results show the feasibility of the scramjet engine rather than a rocket engine for hypersonic flight.

To conclude, some future work is proposed. It should be interesting to compare the results of finite-rate chemistry (non-equilibrium conditions) with experimental data, and do it with different supersonic mixing profiles and chemical reaction mechanisms. The problem is that there is not much free available information on the literature. Another task might be to make a two-dimensional treatment with CFD of the combustion; nevertheless, this corresponds to another project. Keeping this line, a two-dimensional more accurate and detailed modelling could be done for the air inlet and the nozzle.

10. Bibliography

- [1] Fry, Ronald. S. A century of ramjet propulsion technology evolution. Johns Hopkins University, Maryland. *Journal of propulsion and power*, 2004, Vol. 20, No.1.
- [2] Curran, Edward. T. Scramjet engines: the first forty years. U.S. Air Force Research Laboratory, Ohio. *Journal of propulsion and power*, 2001, Vol. 17, No. 6.
- [3] Smart, M. Scramjets. *Advances on propulsion technology for high-speed aircraft*, 2008. Educational Notes RTO-EN-AVT-150, Paper 9.
- [4] McClinton, C. R. High speed/hypersonic aircraft propulsion technology development. *Advances on propulsion technology for high-speed aircraft*, 2008. Educational Notes RTO-EN-AVT-150, Paper 1.
- [5] Falempin, F. Propulsion systems for hypersonic flight. *Lecture Series on "Critical technologies for hypersonic vehicle development"*, 2004. Educational Notes RTO-EN-AVT-116.
- [6] Segal, C. Propulsion systems for hypersonic flight. *Lecture Series on "Critical technologies for hypersonic vehicle development"*, 2004. Educational Notes RTO-EN-AVT-116.
- [7] Nicole Roberts, K. *Analysis and design of a hypersonic scramjet engine with a starting Mach number of 4.00*. Master of Science in Aerospace Engineering, University of Texas at Arlington, Department of Aerospace Engineering, 2008.
- [8] Engman, E. *Numerical simulation of scramjet combustion*. Master of Science in Engineering Physics, Lulea University of Technology, Department of Applied Physics and Mechanical Engineering, 2008.
- [9] National Aeronautics and Space Administration (2009). *Inlet performance*. Retrieved December 14, 2012, from <http://www.grc.nasa.gov/WWW/k-12/airplane/inleth.html>
- [10] Smart, M. Scramjet Inlets. *Advances on propulsion technology for high-speed aircraft*, 2008. Educational Notes RTO-EN-AVT-185, Paper 9.

- [11] Smart, M. Scramjet Isolators. *Advances on propulsion technology for high-speed aircraft*, 2008. Educational Notes RTO-EN-AVT-185, Paper 10.
- [12] Aerospaceweb (2000). *Hydrogen and the scramjet*. Retrieved December 14, 2012, from <http://www.aerospaceweb.org/question/propulsion/q0170.shtml>
- [13] Kerrebrock, J. L. *Aircraft engines and gas turbines*. Second edition. United States of America: MIT Press, 1992. ISBN 0-262-11162-4.
- [14] Hill, P. G.; Peterson, C. R. *Mechanics and thermodynamics of propulsion*. Second edition. United States of America: Addison Wesley Longman, 1992. ISBN 0-201-14659-2.
- [15] Birzer, C.; Doolan, C. J. Quasi-one-dimensional model of hydrogen-fueled scramjet combustors. University of Adelaide, Australia. *Journal of propulsion and power*, 2009, Vol. 25, No. 6.
- [16] Shapiro, A. H. *The dynamics and thermodynamics of compressible fluid flow: Volume I*. First edition. United States of America: John Wiley & Sons, 1953. ISBN 0-471-06691-5.
- [17] O' Brien, T. F.; Starkey, R. P.; Lewis, M. J. Quasi-one-dimensional high-speed engine model with finite-rate chemistry. University of Maryland, Maryland. *Journal of propulsion and power*, 2001, Vol. 17, No. 6.
- [18] Doolan, C. J.; Boyce, R. A quasi-one-dimensional mixing and combustion code for trajectory optimization and design studies. University of Adelaide and University of Queensland, Australia. *15th AIAA International Space Planes and Hypersonic Systems and Technologies Conference*, 2008.
- [19] Anderson, J. D. *Hypersonic and high-temperature gas dynamics*. Second edition. United States of America: AIAA Education Series, 2006. ISBN 1-56347-780-7.
- [20] Glassman, I. Yetter, R. A.; *Combustion*. Fourth edition. United States of America: Elsevier, 2008. ISBN 978-0-12-088-573-2.
- [21] GRI-Mech. (n.d.). *Thermodynamic Data*. Retrieved July 18, 2013, from http://www.me.berkeley.edu/gri_mech/index.html.

- [22] Hass, N. E.; Smart, M, K. Flight data analysis of HyShot 2. NASA Langley Research Center, Virginia; and University of Queensland, Australia. *13th AIAA International Space Planes and Hypersonic Systems and Technologies Conference*, 2005.
- [23] Boyce, R. R.; Paull, A.; Stalker, R. J; Wendt, M.; Chinzei, N.; Miyajima, H. Comparison of supersonic combustion between impulse and vitiation-heated facilities. Imperial College of Science, Technology, and Medicine, United Kingdom; University of Queensland, Australia; and National Aerospace Laboratory, Japan. *Journal of propulsion and power*, 2000, Vol. 16, No. 4.
- [24] Kirchhartz, R, M.; Mee, D. J; Stalker, R. J. Supersonic skin-friction drag with tangential wall slot fuel injection and combustion. University of Queensland, Australia. *AIAA Journal*, 2012, Vol. 50, No. 2.

Annexes

- A. Scramjet evolution
- B. Governing equations detailed development
- C. Air inlet performance
- D. Nozzle performance

A. Scramjet evolution

Era	Country/service	Engine/vehicle	Engine type	Dates, year	Cruise Mach no.	Cruise altitude, ft	Powered range, n mile	Launcher	Total length, in.	Diameter, in.	Total weight, lbm	State of development
1955–1975	U.S. Navy	External burn ^b	ERJ	1957–1962	5–7	—	—	—	—	—	—	Combustion tests
	Russia	Chetinkov research	ERJ	1957–1960	5–7	—	—	—	—	—	—	Component tests
	U.S. Air Force	Marquardt SJ	DMSJ	1960–1970	3–5	—	—	—	88	10 × 15	—	Cooled engine tests
	U.S. Air Force	GASL SJ ^a	SJ	1961–1968	3–12	—	—	—	40	31 in ²	—	Cooled engine tests
	U.S. Navy	SCRAM ^b	LFSJ	1962–1977	7.5	100,000	350	Rail	288	26.2	5,470	Free-jet test
	U.S. Air Force	IFTV ^c	H ₂ /SJ	1965–1967	5–6	56,000	—	—	—	—	—	Component tests
	U.S. Air Force–NASA	HRE ^a	H ₂ /SJ	1966–1974	4–7	—	—	—	87	18	—	Flowpath tests
	NASA	AIM ^b	H ₂ /SJ	1970–1984	4–7	—	—	—	87	18	—	Cooled engine tests
	France	ESOP ^b	DMSJ	1973–1974	5–7	—	—	—	87	18	—	Component tests
	U.S. Navy	WADM/HyWADM ^b	DCR	1977–1986	4–6	80,000–100,000	500–900	VLS	256	21	3,750	Component tests
1975–1990	Russia	Various research	SJ/DCR	1980–1991	5–7	80,000–100,000	—	—	—	—	—	Combustion tests
	NASA	NASP ^b	MCSJ	1986–1994	0–26	0–orbit	Orbital	Runway	—	—	500,000	Free-jet test (M7)
	Germany	Sänger II ^b	ATRJ	1988–1994	4	0–orbit	Orbital	Runway	3976	550	800,000	Concept vehicle

^aSystem discussed and shown. ^bSystem discussed. ^cIFTV incremental flight test vehicle.

Table 7. Worldwide scramjet evolution 1955–1990

Era	Country/service	Engine/vehicle	Engine type	Dates, year	Cruise Mach no.	Cruise altitude, ft	Powered range, n mile	Launcher	Total length, in.	Diameter, in.	Total weight, lbm	State of development
1990–2003	United Kingdom	HOTOL ^c	SJ	1990–1994	2–8	—	—	—	—	—	—	Combustion tests
	Japan	PATRES/ATREX ^b	TRBCC	1990–	0–12	100,000	—	—	87	30	—	Component tests
	Japan	NAL-KPL research ^b	SJ	1991–	4–12	50,000–100,000	—	—	83	8 × 10	—	Component tests
	Russia	Kholod ^a	DCR	1991–1998	3.5–5.4	50,000–115,000	—	SA-5	36	24	—	Flight tests
	Russia/France	Kholod ^a	DCR	1991–1995	3.5–5.4	50,000–115,000	—	SA-5	36	24	—	Flight tests
	Russia/United States	Kholod ^a	DCR	1994–1998	3.5–7	50,000–115,000	—	SA-5	36	24	—	Flight tests
	France	CHAMIOS ^b	SJ	1992–2000	6.5	—	—	—	—	8 × 10	—	Component tests
	France	Monomat	DMSJ	1992–2000	4–7.5	—	—	—	—	4 × 4	—	Component tests
	France	PREPA ^a	DMSJ	1992–1999	2–12	0–130,000	Orbital	Ground	2560	Waverider	1 × 10 ⁶	Component tests
	Russia	ORYOL/MIKAKS	SJ	1993–	0–12	0–130,000	Orbital	Ground	—	—	—	Component tests
	France/Russia	WRR ^b	DMSJ	1993–	3–12	0–130,000	—	Ground	—	Waverider	60,000	Component tests
	Russia	GELA Phase II ^a	RJ/SJ	1995–	3–5+	295,000	—	Tu-22M	—	—	—	Flight tests
	Russia	AJAX ^b	SJ	1995–	0–12	0–130,000	—	—	—	—	—	Concept
	U.S. Air Force	HyTech ^a	SJ	1995–	7–10	50,000–130,000	—	—	87	9 × 12	—	Component tests
	United States	GTX ^d	RBCC ^e	1995–	0–14	50,000–130,000	—	—	—	—	—	Component tests
	U.S. Navy	Counterforce	DCR	1995–	4–8	80,000–100,000	—	Air/VLS	256	21	3,750	Component tests
	NASA	X-43A/Hyper-X ^a	H2/SJ	1995–	7–10	100,000	200	Pegasus	148	60(span)	3,000	Flight tests
	France/Germany	JAPHAR ^a	DMSJ	1997–2002	5–7.6	80,000	—	—	90	4 × 4	—	Component tests
	United States	ARRMD ^b	DCR	1997–2001	3–8	80,000	450–800	Rail/Air	168–256	21	2,200–3,770	Component tests
	Russia	IGLA ^a	SJ	1999–	5–14	82,000–164,000	—	SS-25	197	—	—	Flight tests
	NASA	X-43C ^b	DMSJ	1999–	5–7	100,000	—	Pegasus	—	10.5 wide	—	Component tests
	United States	IHPTET ^b	ATR	1999–	0–5	0–90,000	—	—	—	15–40	—	Component tests
	United States	RTA ^b	TBCC	1999–	0–5	0–90,000	—	—	—	15–40	—	Component tests
	France	Promethee ^b	DMSJ	1999–2002	2–8	0–130,000	—	—	238	—	3,400	Component tests
	India	AVATAR-M ^b	SJ	1999–	0–14	0–orbit	Orbital	Ground	—	—	18–25 ton	Combustion tests
	United Kingdom	HOTOL Phase II	SJ	2000–	2–8	—	—	—	—	—	—	Component tests
	France	PIAF ^b	DMSJ	2000–	2–8	0–110,000	—	—	53	8 × 2	—	Component tests
	United States	MARIAH	MHD/SJ	2001–	15	—	—	—	—	—	—	Combustion tests
	Australia	HyShot ^b	SJ	2001–2002	7.6	75,000–120,000	200	Terror Orion	55	14	—	Flight tests
	United States	Gun launch technology	SJ	2001–	—	—	—	Ground	—	—	—	Flight tests
	United States	ISTAR ^b	RBCC ^e	2002–2003	2.4–7	0–orbit	Orbital	Ground	400	Waverider	20,000	Component tests
	United States	X-43B ^b	RB/TBCC	2002–2003	0–10	100,000	200	Air	500	Waverider	24,000	Component tests
	Russia	Mig-31 HFL ^b	SJ/DCR	2002–	2–10	50,000–130,000	—	Mig-31	—	—	—	Planned flight tests
	United States	HyFly ^a	DCR	2002–	3–6.5	85,000–95,000	600	F-4	225	19	2,360	Flight tests planned
	United States	SED ^a	SJ	2003–	4.5–7	80,000	—	—	—	9 wide	—	Planned flight tests
	France	LEA ^a	SJ/DCR	2003–2012	4–8	80,000	—	Air	—	—	—	Flight tests planned
	United States	RCCFD ^b	TBCC	2003–	0.7–7	0–orbit	Orbital	Ground	400	Waverider	20,000	Flight tests planned

^aSystem discussed and shown. ^bSystem discussed. ^cHorizontal takoff and landing (HOTOL). ^dNASA Glenn Rc hydrogen fueled/cooled (GTX). ^eReference vehicle designation (RBCC).

Table 8. Worldwide scramjet evolution 1990–today

B. Governing equations detailed development

Mass conservation

$$\dot{m} = \rho u A$$

$$\ln(\dot{m}) = \ln(\rho u A)$$

$$\ln \dot{m} = \ln \rho + \ln u + \ln A$$

$$(\ln \dot{m})' = (\ln \rho + \ln u + \ln A)'$$

$$\frac{1}{\dot{m}} \frac{d\dot{m}}{dx} = \frac{1}{\rho} \frac{d\rho}{dx} + \frac{1}{u} \frac{du}{dx} + \frac{1}{A} \frac{dA}{dx}$$

$$\frac{d\rho}{dx} = \rho \left(\frac{1}{\dot{m}} \frac{d\dot{m}}{dx} - \frac{1}{u} \frac{du}{dx} - \frac{1}{A} \frac{dA}{dx} \right)$$

Momentum conservation

$$\begin{aligned} (pA)|_x - (pA)|_{x+\Delta x} + \int_x^{x+\Delta x} p dA - \int_x^{x+\Delta x} F_{wall} dx - \int_x^{x+\Delta x} F_{mix} dx \\ = (\dot{m}u + \dot{m}_f u_f)|_{x+\Delta x} - (\dot{m}u + \dot{m}_f u_f)|_x \end{aligned}$$

$$-\frac{d(pA)}{dx} + p \frac{dA}{dx} - F_{wall} - F_{mix} = \frac{d}{dx} (\dot{m}u + \dot{m}_f u_f)$$

$$-\frac{dp}{dx} A - p \frac{dA}{dx} + p \frac{dA}{dx} - F_{wall} - F_{mix} = \frac{d\dot{m}}{dx} u + \dot{m} \frac{du}{dx} + \frac{d\dot{m}_f}{dx} u_f + \dot{m}_f \frac{du_f}{dx}$$

$$\left| \dot{m}_f \frac{du_f}{dx} \right| \ll \left| \dot{m} \frac{du}{dx} \right|$$

$$u_f = u\varepsilon$$

$$-\frac{dp}{dx} A - F_{wall} - F_{mix} = \frac{d\dot{m}}{dx} u + \dot{m} \frac{du}{dx} + \frac{d\dot{m}_f}{dx} u\varepsilon$$

$$\frac{dp}{dx} + \frac{1}{A} F_{wall} + \frac{1}{A} F_{mix} + \frac{1}{A} \frac{d\dot{m}}{dx} u + \frac{1}{A} \dot{m} \frac{du}{dx} + \frac{1}{A} \frac{d\dot{m}_f}{dx} u\varepsilon = 0$$

$$\frac{dp}{dx} + \frac{1}{A} F_{wall} + \frac{1}{A} F_{mix} + \frac{1}{A} \frac{d\dot{m}}{dx} u + \rho u \frac{du}{dx} + \frac{1}{A} \frac{d\dot{m}_f}{dx} u\varepsilon = 0$$

$$\frac{d\dot{m}_f}{dx} = -\frac{d\dot{m}}{dx}$$

$$\frac{dp}{dx} + \frac{1}{A}F_{wall} + \frac{1}{A}F_{mix} + \rho u \frac{du}{dx} + \frac{1}{A} \frac{d\dot{m}}{dx} u(1 - \varepsilon) = 0$$

$$F_{wall} = \frac{1}{2} \rho u^2 c_f P_w$$

$$F_{mix} = \frac{1}{2} \rho u^2 c_{fj} P_{fj}$$

$$\frac{dp}{dx} + \frac{1}{2} \rho u^2 c_f \frac{P_w}{A} + \frac{1}{2} \rho u^2 c_{fj} \frac{P_{fj}}{A} + \rho u \frac{du}{dx} + \frac{1}{A} \frac{d\dot{m}}{dx} u(1 - \varepsilon) = 0$$

$$\frac{dp}{dx} = - \left(\frac{1}{2} \rho u^2 c_f \frac{P_w}{A} + \frac{1}{2} \rho u^2 c_{fj} \frac{P_{fj}}{A} + \rho u \frac{du}{dx} + \frac{1}{A} \frac{d\dot{m}}{dx} u(1 - \varepsilon) \right)$$

Energy conservation

$$\begin{aligned} (puA + u_f A_f p) \Big|_x - (puA + u_f A_f p) \Big|_{x+\Delta x} + \int_x^{x+\Delta x} \dot{q} P_w dx \\ = (\dot{m} e_t + \dot{m}_f e_{tf}) \Big|_{x+\Delta x} - (\dot{m} e_t + \dot{m}_f e_{tf}) \Big|_x \end{aligned}$$

$$-\frac{d(puA)}{dx} + \dot{q} P_w = \frac{d}{dx} (\dot{m} e_t + \dot{m}_f e_{tf})$$

$$e_t = h_t - \frac{p}{\rho}$$

$$-\frac{d(puA)}{dx} + \dot{q} P_w = \frac{d}{dx} \left(\dot{m} h_t - \dot{m} \frac{p}{\rho} \right) + \frac{d}{dx} \left(\dot{m}_f h_{tf} - \dot{m}_f \frac{p_f}{\rho_f} \right)$$

$$p_f = p$$

$$h_t = h + \frac{1}{2} u^2$$

$$-\frac{d(puA)}{dx} + \dot{q} P_w = \frac{d}{dx} \left(\dot{m} h + \dot{m} \frac{1}{2} u^2 \right) + \frac{d}{dx} \left(\dot{m}_f h_f + \dot{m}_f \frac{1}{2} u_f^2 \right) - \frac{d}{dx} \left(\dot{m} \frac{p}{\rho} + \dot{m}_f \frac{p}{\rho_f} \right)$$

$$-\frac{d(puA)}{dx} + \dot{q} P_w = \frac{d}{dx} (\dot{m} h + \dot{m}_f h_f) + \frac{d}{dx} \left(\frac{1}{2} \dot{m} u^2 + \frac{1}{2} \dot{m}_f u_f^2 \right) - \frac{d}{dx} (uAp + u_f A_f p)$$

$$\left| \frac{1}{2} \dot{m}_f u_f^2 \right| \ll \left| \frac{1}{2} \dot{m} u^2 \right|$$

$$-\frac{d(puA)}{dx} + \dot{q} P_w = \frac{d}{dx} (\dot{m} h + \dot{m}_f h_f) + \frac{d}{dx} \left(\frac{1}{2} \dot{m} u^2 \right) - \frac{d(uAp)}{dx}$$

$$\frac{d}{dx}(\dot{m}h + \dot{m}_f h_f) + \frac{d}{dx}\left(\frac{1}{2}\dot{m}u^2\right) - \dot{q}P_w = 0$$

$$\frac{d\dot{m}}{dx}h + \dot{m}\frac{dh}{dx} + \frac{d\dot{m}_f}{dx}h_f + \dot{m}_f\frac{dh_f}{dx} + \frac{1}{2}\left(\frac{d\dot{m}}{dx}u^2 + \dot{m}\frac{du^2}{dx}\right) - \dot{q}P_w = 0$$

$$\left|\dot{m}_f\frac{dh_f}{dx}\right| \ll \left|\dot{m}\frac{dh}{dx}\right|$$

$$\frac{d\dot{m}}{dx}h + \dot{m}\frac{dh}{dx} + \frac{d\dot{m}_f}{dx}h_f + \frac{1}{2}\frac{d\dot{m}}{dx}u^2 + \dot{m}u\frac{du}{dx} - \dot{q}P_w = 0$$

$$\frac{dh}{dx} = -\frac{1}{\dot{m}}\frac{d\dot{m}}{dx}\left(h + \frac{1}{2}u^2\right) - \frac{1}{\dot{m}}\frac{d\dot{m}_f}{dx}h_f - u\frac{du}{dx} + \frac{\dot{q}P_w}{\dot{m}}$$

$$\frac{d\dot{m}_f}{dx} = -\frac{d\dot{m}}{dx}$$

$$\frac{dh}{dx} = -\frac{1}{\dot{m}}\frac{d\dot{m}}{dx}\left(h + \frac{1}{2}u^2\right) + \frac{1}{\dot{m}}\frac{d\dot{m}}{dx}h_f - u\frac{du}{dx} + \frac{\dot{q}P_w}{\dot{m}}$$

$$h = \sum_i h_i Y_i$$

$$\frac{dh}{dx} = \sum_i \left(\frac{dh_i}{dx}Y_i + h_i\frac{dY_i}{dx}\right)$$

$$h_i = \Delta h_{f,i}^0 + \int_{T_0}^T c_{p_i} dT = \frac{R_u}{MW_i} \left(a_1 T + a_2 \frac{T^2}{2} + a_3 \frac{T^3}{3} + a_4 \frac{T^4}{4} + a_5 \frac{T^5}{5} + a_6 \right)$$

$$\frac{dh_i}{dx} = c_{p_i} \frac{dT}{dx}$$

$$c_{p_i} = \frac{R_u}{MW_i} (a_1 + a_2 T + a_3 T^2 + a_4 T^3 + a_5 T^4)$$

$$\sum_i \left(c_{p_i} \frac{dT}{dx} Y_i + h_i \frac{dY_i}{dx} \right) = -\frac{1}{\dot{m}}\frac{d\dot{m}}{dx}\left(h + \frac{1}{2}u^2\right) + \frac{1}{\dot{m}}\frac{d\dot{m}}{dx}h_f - u\frac{du}{dx} + \frac{\dot{q}P_w}{\dot{m}}$$

$$c_p \frac{dT}{dx} = -\sum_i \left(h_i \frac{dY_i}{dx} \right) - \frac{1}{\dot{m}}\frac{d\dot{m}}{dx}\left(h + \frac{1}{2}u^2\right) + \frac{1}{\dot{m}}\frac{d\dot{m}}{dx}h_f - u\frac{du}{dx} + \frac{\dot{q}P_w}{\dot{m}}$$

$$c_p = \sum_i c_{p_i} Y_i$$

$$\frac{dT}{dx} = \frac{1}{c_p} \left[-\sum_i \left(h_i \frac{dY_i}{dx} \right) - \frac{1}{\dot{m}}\frac{d\dot{m}}{dx}\left(h + \frac{1}{2}u^2\right) + \frac{1}{\dot{m}}\frac{d\dot{m}}{dx}h_f - u\frac{du}{dx} + \frac{\dot{q}P_w}{\dot{m}} \right]$$

Equation of state

$$p = \frac{\rho R_u T}{\overline{MW}}$$

$$\ln p = \ln \frac{\rho R_u T}{\overline{MW}}$$

$$\ln p = \ln \rho + \ln R_u + \ln T - \ln \overline{MW}$$

$$(\ln p)' = (\ln \rho + \ln R_u + \ln T - \ln \overline{MW})'$$

$$\frac{1}{p} \frac{dp}{dx} = \frac{1}{\rho} \frac{d\rho}{dx} + \frac{1}{T} \frac{dT}{dx} - \frac{1}{\overline{MW}} \frac{d\overline{MW}}{dx}$$

$$\overline{MW} = \frac{1}{\sum_i \frac{Y_i}{MW_i}}$$

$$\frac{d\overline{MW}}{dx} = -\overline{MW}^2 \left(\sum_i \frac{1}{MW_i} \frac{dY_i}{dx} \right)$$

Species conservation

$$(\dot{m}_i)_{x+\Delta x} - (\dot{m}_i)_x = (\dot{m}_i)_{addition} + \dot{\omega}_i MW_i A \Delta x$$

$$\frac{d(\dot{m}_i)}{dx} = \frac{d(\dot{m}_i)_{addition}}{dx} + \dot{\omega}_i MW_i A$$

$$\dot{m}_i = \dot{m} Y_i$$

$$\frac{d(\dot{m} Y_i)}{dx} = \frac{d(\dot{m}_i)_{addition}}{dx} + \dot{\omega}_i MW_i A$$

$$\frac{d\dot{m}}{dx} Y_i + \dot{m} \frac{dY_i}{dx} = \frac{d(\dot{m}_i)_{addition}}{dx} + \dot{\omega}_i MW_i A$$

$$\frac{dY_i}{dx} = \frac{1}{\dot{m}} \frac{d(\dot{m}_i)_{addition}}{dx} + \frac{\dot{\omega}_i MW_i A}{\rho u} - \frac{Y_i}{\dot{m}} \frac{d\dot{m}}{dx}$$

Equation for the velocity

$$\begin{aligned}
\frac{1}{p} \frac{dp}{dx} &= \frac{1}{\rho} \frac{d\rho}{dx} + \frac{1}{T} \frac{dT}{dx} - \frac{1}{\overline{MW}} \frac{d\overline{MW}}{dx} \\
-\frac{1}{p} \left(\frac{1}{2} \rho u^2 c_f \frac{P_w}{A} + \frac{1}{2} \rho u^2 c_{fj} \frac{P_{fj}}{A} + \rho u \frac{du}{dx} + \frac{1}{A} \frac{d\dot{m}}{dx} u (1 - \varepsilon) \right) \\
&= \frac{1}{\dot{m}} \frac{d\dot{m}}{dx} - \frac{1}{u} \frac{du}{dx} - \frac{1}{A} \frac{dA}{dx} \\
&\quad + \frac{1}{c_p T} \left[- \sum_i \left(h_i \frac{dY_i}{dx} \right) - \frac{1}{\dot{m}} \frac{d\dot{m}}{dx} \left(h + \frac{1}{2} u^2 \right) + \frac{1}{\dot{m}} \frac{d\dot{m}}{dx} h_f - u \frac{du}{dx} + \frac{\dot{q} P_w}{\dot{m}} \right] \\
&\quad - \frac{1}{\overline{MW}} \frac{d\overline{MW}}{dx} \\
-\frac{\rho u}{p} \frac{du}{dx} + \frac{1}{u} \frac{du}{dx} + \frac{u}{c_p T} \frac{du}{dx} \\
&= \frac{1}{\dot{m}} \frac{d\dot{m}}{dx} - \frac{1}{A} \frac{dA}{dx} - \frac{1}{\overline{MW}} \frac{d\overline{MW}}{dx} \\
&\quad + \frac{1}{c_p T} \left[- \sum_i \left(h_i \frac{dY_i}{dx} \right) - \frac{1}{\dot{m}} \frac{d\dot{m}}{dx} \left(h + \frac{1}{2} u^2 \right) + \frac{1}{\dot{m}} \frac{d\dot{m}}{dx} h_f + \frac{\dot{q} P_w}{\dot{m}} \right] \\
&\quad + \frac{1}{p} \left(\frac{1}{2} \rho u^2 c_f \frac{P_w}{A} + \frac{1}{2} \rho u^2 c_{fj} \frac{P_{fj}}{A} + \frac{1}{A} \frac{d\dot{m}}{dx} u (1 - \varepsilon) \right) \\
\frac{du}{dx} &= \frac{1}{\alpha} \left\{ \frac{1}{\dot{m}} \frac{d\dot{m}}{dx} - \frac{1}{A} \frac{dA}{dx} - \frac{1}{\overline{MW}} \frac{d\overline{MW}}{dx} \right. \\
&\quad + \frac{1}{c_p T} \left[- \sum_i \left(h_i \frac{dY_i}{dx} \right) - \frac{1}{\dot{m}} \frac{d\dot{m}}{dx} \left(h + \frac{1}{2} u^2 \right) + \frac{1}{\dot{m}} \frac{d\dot{m}}{dx} h_f + \frac{\dot{q} P_w}{\dot{m}} \right] \\
&\quad \left. + \frac{1}{p} \left(\frac{1}{2} \rho u^2 c_f \frac{P_w}{A} + \frac{1}{2} \rho u^2 c_{fj} \frac{P_{fj}}{A} + \frac{1}{A} \frac{d\dot{m}}{dx} u (1 - \varepsilon) \right) \right\} \\
\alpha &= -\frac{\rho u}{p} + \frac{1}{u} + \frac{u}{c_p T}
\end{aligned}$$

C. Air inlet performance

Through a scramjet inlet a set of shock waves occurs. In this section are detailed the governing equations of shock waves. An oblique shock wave can be schematized by

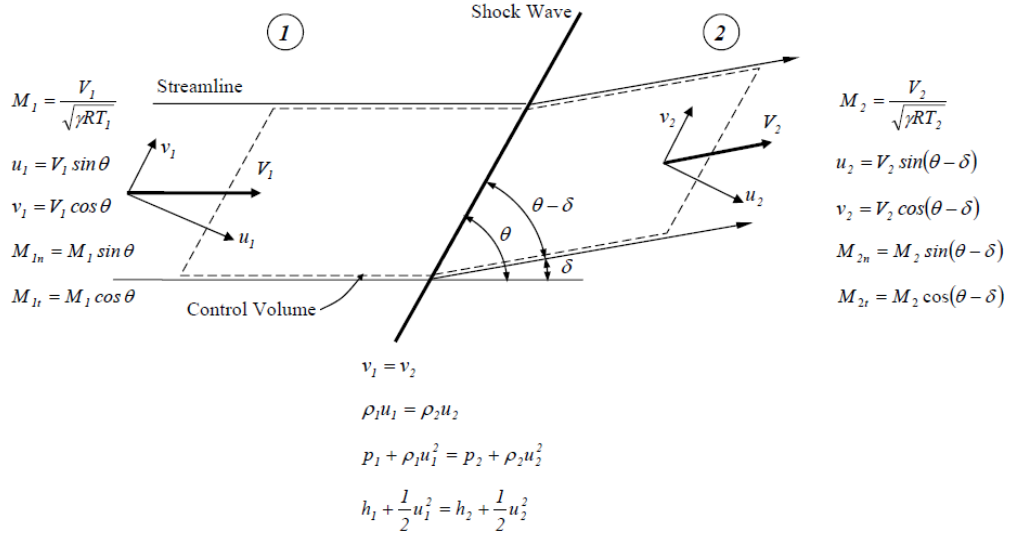


Figure 40. Oblique shock wave

The summary of equations for a thermally perfect gas is the following

$$\frac{p_2}{p_1} = \frac{\frac{\gamma+1}{\gamma-1} \frac{\rho_2}{\rho_1} - 1}{\frac{\gamma+1}{\gamma-1} - \frac{\rho_2}{\rho_1}} \quad \text{or} \quad \frac{\rho_2}{\rho_1} = \frac{\frac{\gamma+1}{\gamma-1} \frac{p_2}{p_1} - 1}{\frac{\gamma+1}{\gamma-1} - \frac{p_2}{p_1}} \quad (\text{Rankine - Hugoniot}) \quad (\text{C.1})$$

$$u_{1n} u_{2n} = (c^*)^2 \quad (\text{Prandtl}) \quad \text{with} \quad c^* = \sqrt{\gamma R_g T^*} = \sqrt{\frac{2\gamma R_g T_t}{\gamma+1}} \quad (\text{C.2})$$

$$T_{t2} = T_{t1} \quad (\text{C.3})$$

$$M_{1n} = M_1 \sin \theta \quad (\text{C.4})$$

$$M_{2n}^2 = \frac{2 + (\gamma - 1) M_{1n}^2}{-(\gamma - 1) + 2\gamma M_{1n}^2} \quad (\text{C.5})$$

$$\frac{T_2}{T_1} = \frac{2 + (\gamma - 1) M_{1n}^2}{2 + (\gamma - 1) M_{2n}^2} \quad (\text{C.6})$$

$$\frac{p_2}{p_1} = \frac{2\gamma}{\gamma+1} M_{1n}^2 - \frac{\gamma-1}{\gamma+1} \quad (C.7)$$

$$\frac{p_{t1}}{p_{t2}} = \left(\frac{2\gamma}{\gamma+1} M_{1n}^2 - \frac{\gamma-1}{\gamma+1} \right)^{\frac{1}{\gamma-1}} \left(\frac{2 + (\gamma-1)M_{1n}^2}{(\gamma+1)M_{1n}^2} \right)^{\frac{\gamma}{\gamma-1}} \quad (C.8)$$

The condition $v_1 = v_2$ gives

$$\frac{u}{\sin\theta} \cos\theta = \frac{u_2}{\sin(\theta-\delta)} \cos(\theta-\delta) \rightarrow \tan(\theta-\delta) = \tan\theta \frac{M_{2n}}{M_{1n}} \sqrt{\frac{T_2}{T_1}} \quad (C.9)$$

For an oblique shock wave, since $u_2 < u_1$ and $v_1 = v_2$, the flow is always deflected towards the shock wave. For a normal shock wave we have $\theta = \frac{\pi}{2}$, so $M_{1n} = M_1$ and $M_{2n} = M_2$.

Fixing the number of shock waves and its angles, the total pressure ratio π_d can be found. For example, suppose a three shock wave inlet (two oblique and a final normal shock) such as Figure 41. Notice that the overall inlet π_d is the product of the total pressure ratio at each shock wave

$$\pi_d = \frac{p_{t2}}{p_{t0}} = \frac{p_{t2}}{p_{t12}} \frac{p_{t12}}{p_{t01}} \frac{p_{t01}}{p_{t0}} \quad (C.10)$$

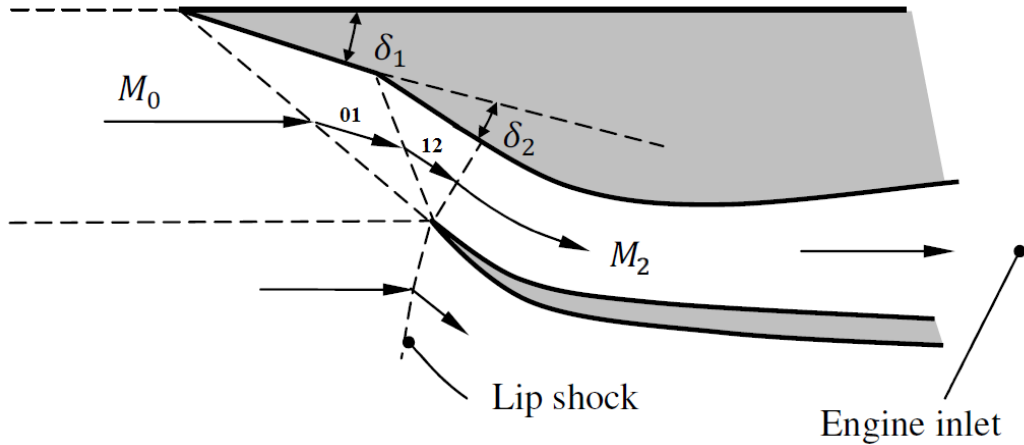


Figure 41. Scramjet inlet with three shock waves

Now, the inlet total pressure ratio is related with a kinetic energy efficiency.

The kinetic energy efficiency η_d is defined as the ratio of available kinetic energy at diffuser exit (reduced isentropically to ambient pressure) to available kinetic energy at freestream conditions

$$\eta_d = \frac{\frac{1}{2}u_2'^2}{\frac{1}{2}u_0^2} = \frac{u_2'^2}{u_0^2} \quad (\text{C.11})$$

It can be related to π_d taking into account the following expressions

$$\pi_d = \frac{p_{t2}}{p_{t0}} = \frac{p_{t2}'}{p_{t0}} = \frac{p_2'}{p_0} \left(\frac{1 + \frac{\gamma-1}{2} M_2'^2}{1 + \frac{\gamma-1}{2} M_0^2} \right)^{\frac{\gamma}{\gamma-1}} = \left(\frac{1 + \frac{\gamma-1}{2} M_2'^2}{1 + \frac{\gamma-1}{2} M_0^2} \right)^{\frac{\gamma}{\gamma-1}} \quad (\text{C.12})$$

$$M_2'^2 = \frac{u_2'^2}{\gamma R_g T_2'} = \frac{\eta_d u_0^2}{\gamma R_g T_2'} \quad (\text{C.13})$$

$$T_0 + \frac{u_0^2}{2c_p} = T_2' + \frac{u_2'^2}{2c_p} = T_2' + \frac{\eta_d u_0^2}{2c_p} \rightarrow T_2' = T_0 + (1 - \eta_d) \frac{u_0^2}{2c_p} \quad (\text{C.14})$$

Substituting Eqs. (C.13) and (C.14) to (C.12), it is get

$$\pi_d = \left[1 + (1 - \eta_d) \frac{\gamma-1}{2} M_0^2 \right]^{\frac{-\gamma}{\gamma-1}} \quad (\text{C.15})$$

The following picture relates the total pressure ratio in function of flight Mach number for various values of kinetic energy efficiency.

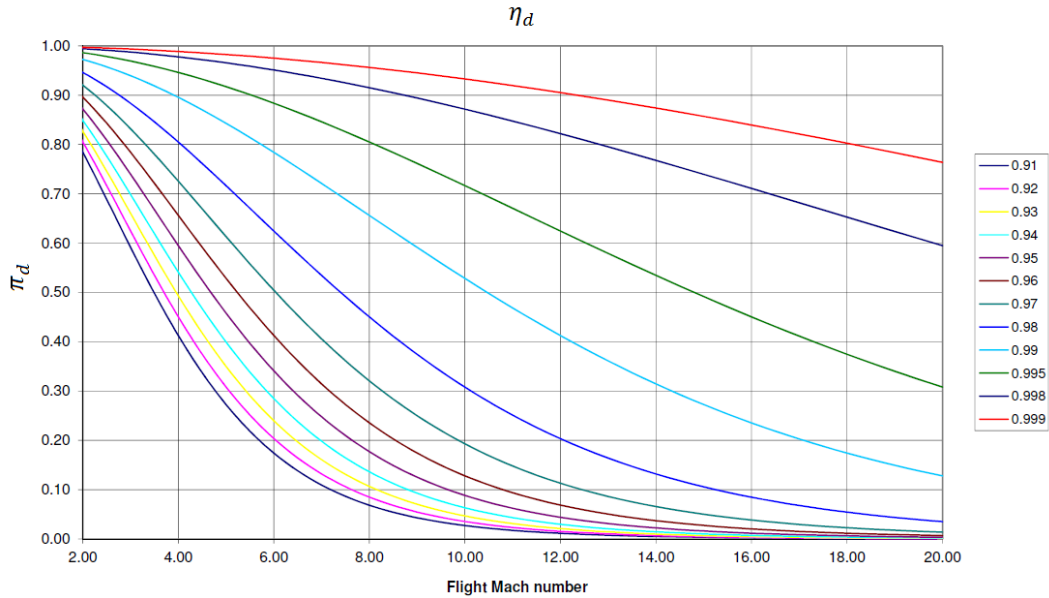


Figure 42. Total pressure ratio in function of flight Mach number and kinetic energy efficiency

D. Nozzle performance

This section analyses the performance of a nozzle in order to have an overall vision of a scramjet. A detailed and accurate development of a scramjet nozzle should be using a two-dimensional treatment but this is out of the current study. Therefore, for the sake of simplicity, an internal¹⁵ expansion is assumed. Furthermore, the treatment done here considers an ideal expansion, and then a correction is applied to represent the real performance.

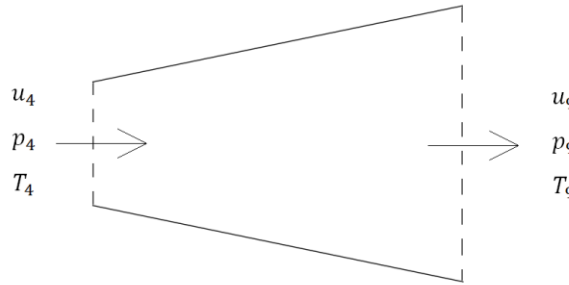


Figure 43. Internal nozzle

An ideal nozzle expands the flow isentropically until the exit pressure matches the atmospheric pressure ($p_9 = p_0$). Considering the flow as a semi-perfect gas, and knowing the nozzle inlet conditions, the exit flow properties can be determined following an iterative procedure:

- 1) Assume T_9 .
- 2) Compute the integral

$$I = \int_{T_9}^{T_{t4}} \frac{c_p(T)}{T} dT \quad (D.1)$$

- 3) Calculate p_9 from

$$\frac{p_{t4}}{p_9} = e^{\frac{I}{R_g}} \quad (D.2)$$

- 4) Iterate T_9 until the p_9 obtained at step 3 equals the atmospheric pressure p_0 .
- 5) Finally, knowing T_9 the static enthalpy can be determined, and u_9 is obtained from

$$h_{t4} = h_9 + \frac{1}{2} u_9^2 \quad (D.3)$$

¹⁵ Scramjet nozzles are completely external or both internal and external.

Notice that $T_{t9} = T_{t4}$, $p_{t9} = p_{t4}$, and $h_{t9} = h_{t4}$, since in an isentropic evolution the total variables are constant.

When the ideal nozzle exit velocity has been computed, viscous effects can be accounted for by the use of a nozzle velocity coefficient

$$C_v = \frac{\text{actual exhaust velocity}}{\text{ideal exhaust velocity}} \quad (\text{D.4})$$

And finally, the thrust and the specific impulse can be obtained.